Spring 5-16-2020

Soil Moisture Contributions to InSAR Phase and Decorrelation

Yusuf Eshqi Molan
Southern Methodist University, yeshqimolan@smu.edu

SOIL MOISTURE CONTRIBUTIONS TO INSAR PHASE AND DECORRELATION

Approved by:

_____
Prof. Zhong Lu
Professor of Geophysics

_____
Prof. Robert T. Gregory
Professor of Geochemistry

_____
Prof. Matthew Hornbach
Professor of Geophysics

_____
Dr. Jin-Woo Kim
SAR/InSAR Research Scientist

_____
Dr. Piyush S. Agram
Electrical Engineering

SOIL MOISTURE CONTRIBUTIONS TO INSAR PHASE AND DECORRELATION

A Dissertation Presented to the Graduate Faculty of

Dedman College

Southern Methodist University

in

Partial Fulfillment of the Requirements

for the degree of

Doctor of Philosophy

with a

Major in Geophysics

by

Yusuf Eshqi Molan

M.Sc., Mining Engineering – Mineral resources Exploration, Amirkabir University of Technology, Tehran, Iran

B.Sc., Mining Engineering. – Mineral resources Exploration, Sahand University of Technology, Tabriz, Iran

May 16, 2020

ACKNOWLEDGMENTS

I would like to thank my advisor Prof. Zhong Lu. He sets a very high standard of professionalism and compassion to follow. I benefited specifically from his subtle guidance of my learning and research. In addition, he is extremely kind, generous, and supportive and I am very grateful for him. I would like to thank Dr. Jin-Woo Kim for his very useful tutorials and scripts of InSAR processing. I also thank my other committee members, Dr. Robert Gregory, Dr. Matt Hornbach, and Dr. Piyush Agram for their help and constructive suggestions. I thank the faculty, staff, and students at the Department of Earth Sciences, specially, Stephanie Schwob, Maria Richards, and Dr. Gregory for creating friendly environment within the department. I am grateful to my colleagues and friends at SMU radar lab for being good friend and providing me with positive teaming environments. I thank my wife, Elham Kalantari. She has selflessly given me inspiration, unwavering state of love, and encouragement throughout. Without a doubt, I could not have completed this PhD without her dedication. Special thanks to my daughter, Elay, for her patience during this time. She showed understanding beyond her age. Finally, I thank my parents and parents-in-law for encouragement and support throughout my PhD.

Eshqi Molan, Yusuf

M.Sc., Amirkabir University of Technology
B.Sc., Sahand University of Technology

Soil Moisture Contributions to InSAR Phase and Decorrelation

Advisor: Professor Zhong Lu
Doctor of Philosophy conferred May 16, 2020
Dissertation completed April 21, 2020

Interferometric synthetic aperture radar (InSAR) provides capability to detect surface deformation. Between two SAR images, in addition to ground surface deformations, changes may happen in the surface parameters such as soil moisture, vegetation layer water content, and so on. Despite deformation, the other changes may not be of interest for a common InSAR analysis and an ordinary InSAR analysis rarely takes into account their influences on InSAR phase and coherence. The effect of the changes on InSAR phase and coherence can potentially impede accurate estimation of ground surface deformation but also can open new window into soil moisture retrieval and vegetation layer properties estimation.

So far, numerous InSAR processing methods such as persistent scatterers (PS), and short baseline subset (SBAS) approaches have been introduced. Regardless of the processing methodology, however, temporal decorrelation is a major obstacle for all InSAR applications especially over vegetated areas and dynamic environments. Temporal coherence is usually modeled as a univariate exponential function of temporal baseline. Here, I introduce a new temporal decorrelation model that considers changes in surface backscattering by utilizing the relative change in SAR intensity between two images as a proxy for the change in surface scattering parameters.

The phase of interferograms generated from single-looked pixels are rather noisy due to strong effects of decorrelations and noises. One way to deal with this problem is using multi-looked interferograms. Another approach is exploring methods such as SqueeSAR, and the component extraction and selection SAR (CAESAR), which have been developed to extend Persistent Scatterers Interferometry (PSI) analysis. Multi-looking, however, leads to non-zero phase triplet. I analyze the influence of the statistical properties of intensity and phase of single-looked pixels on the phase and coherence of multi-looked pixels.

Potentially, modeling soil moisture influence on InSAR phase measurements and SAR intensity changes provides a means to compensate soil moisture induced InSAR phase artifacts and also to retrieve surface soil moisture. I present a new approach and a comprehensive model to estimate soil moisture induced SAR intensity and InSAR phase changes. The model can not only provide improved estimation of soil moisture induced intensity and phase changes but also potentially be used to infer soil structure.

TABLE OF CONTENTS

LIST OF FIGURES

LIST OF TABLES

To Elham and Elay

CHAPTER 1

INTRODUCTION

1.1 SAR imaging

Synthetic Aperture Radar (SAR) is a signal processing method to create images of the Earth's surface using a radar instrument mounted on a space-borne or air-borne platform. As the satellite moves along its orbit at a height h with a velocity v, the radar instrument illuminates a swath on the ground by pointing a radar beam towards the Earth and perpendicular to the satellite motion. The scatterers in the illuminated swath phase encode and backscatter the transmitted radar echoes toward the receiver mounted on the satellite.

SAR data are in the format of complex numbers. This is to record the phase and amplitude information of backscattering signal. The phase, which is moduled by 2π, is proportional to the time delay between the transmitted beam and received signal. In other words, it represents the radar signal's round-trip traveling distance between the sensor and ground target, as well as the interaction of the radar signal with ground targets (Hanssen, 2001). Hence, to retrieve the continuous phase changes, a subsequent unwrapping procedure should be applied. The amplitude represents the intensity of the backscattered electromagnetic energy. The intensity of the received signal is a function of the imaging radar geometry such as incidence angle, *i.e.* the angle between the normal to the ground surface and the radar echo propagation direction, satellite height, etc (Hanssen, 2001). In addition, the radar reflectivity of scatterers on the

ground, *i.e.* surface dielectric constant, surface roughness, and surface slope, also determine the intensity of the received radar signal.

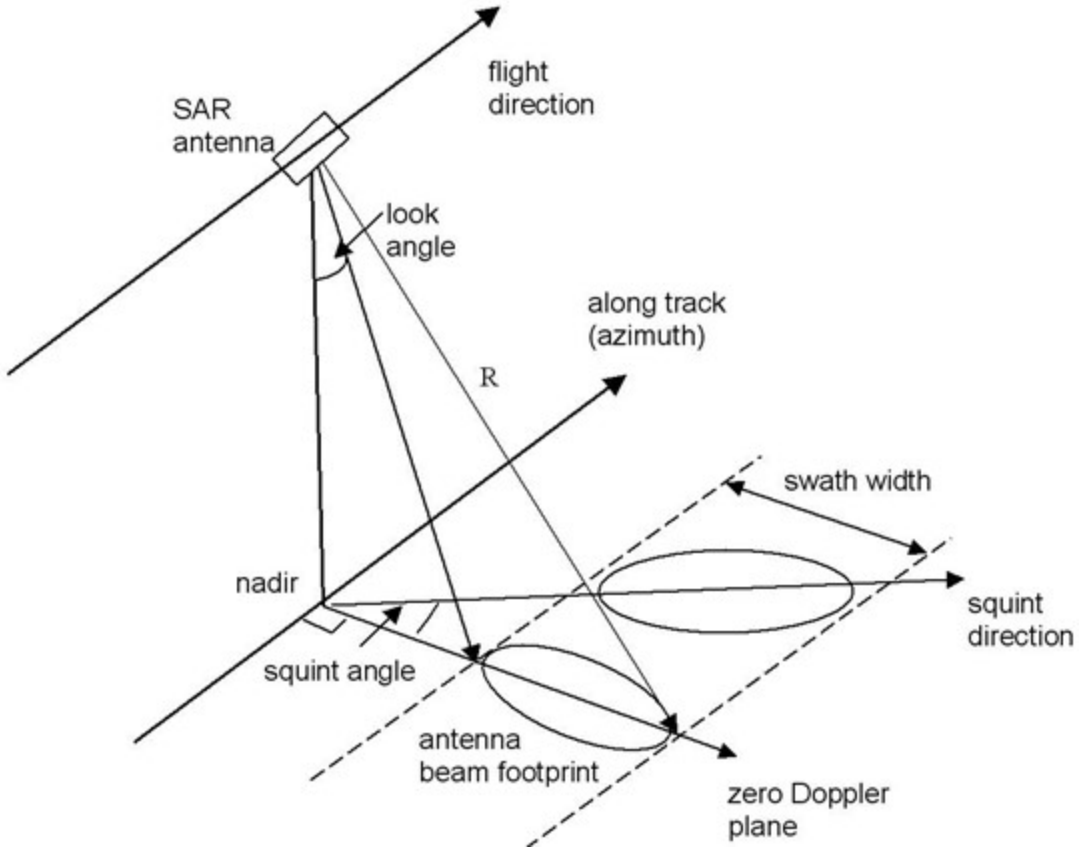

Figure 1.1. The imaging geometry of a space-borne SAR system (Image: European Space Agency (ESA))

1.2 Range and Azimuth Compression

SAR images have two dimensions. One dimension define as the range direction or the across-track direction, which is parallel to the radar beam. The other dimension is referred as the azimuth direction, or the along track direction, which is along the satellite motion direction.

Raw SAR data is a 2-D function of range and azimuth. Range compression is the first step in the digital SAR processor, and is done with fast Fourier transform (FFT) (Hanssen, 2001). In the range direction, the radar antenna often sends out a linear frequency-modulated (FM) plus, which is called chirp. This chirp propagates to the ground where it reflects from scatterers. Every point will return chirp echo. The received signal then will be correlated with the replica of transmitted chirp. The received radar data consists of the complex reflectivity of the surface convolved with the chirp. The objective of range processing is to recover the complex reflectivity by deconvolution of the chirp. Therefore, the impulse response in the time domain is approximately a sinc function

$$Sinc\left(\tau.B_p\right) = \frac{\sin(\pi\,\tau\,B_p)}{\pi\,\tau\,B_p} \tag{1.1}$$

where τ is time, and B_p is the chirp bandwidth. Then the range resolution is

$$\rho_R \cong \frac{c}{2\,B_p} \tag{1.2}$$

As the radar instrument moves along the azimuth, it transmits pulses at the pulse repetition frequency (PRF). Thus, each point in the swath will be illuminated by multiple pulses. The echoes from multiple illuminations creates the second chirp function in the azimuth direction. In other words, the received signals from a scatterer are shifted in frequency due to the

relative movement between the radar instrument and the scatterer. This effect is known as "Doppler effect". Therefore, the next step is to focus the data in azimuth direction. This is done by generating a frequency-modulated chirp. The velocity of the spacecraft, the pulse repetition frequency (PRF), and the absolute range define the chirp parameters. The chirp is FFT transformed into frequency space. Then it is multiplied by each column of range-migrated data. This generates an inverse Fourier transformed image.

The time that a scatterer is illuminated by multiple pulses can be approximated by

$$\tau_{az} = \frac{\mathrm{r}_0 \lambda}{v\, l} \tag{1.3}$$

where l is the length of the antenna, $\frac{\mathrm{r}_0 \lambda}{l}$ is the synthetic aperture length, and v is the speed of the satellite. Therefore, the azimuth bandwidth will be

$$BW_{az} = \frac{2v}{l} \tag{1.4}$$

And finally the azimuth resolution is

$$\delta_{az} = \frac{l}{2} \tag{1.5}$$

The final product is focused SAR image with the azimuth and ranges resolutions of few meters.

1.3 InSAR

The phase of a pixel on a SAR image, which is moduled by 2π, is linearly related to the slant range from the satellite to the ground target

$$\phi_1(i,j) = -\frac{4\pi}{\lambda} r_1(i,j) + \varepsilon_1(i,j) \quad (1.6)$$

where λ is the wavelength of the radar, ε_1 is the sum of phase shifts due to the interaction between the incident radar wave and the scatterers within the resolution cell. InSAR requires two SAR images taken from the identical vantage of repeating passes with different acquisition times, and different positions, *i.e.* temporal, and spatial baselines. The two images should be co-registered first. Image co-registration is the process of geometrically aligning two or more images. This means that same ground feature between images are aligned on the same spatial position. The initial interferometric phase ϕ_{init} between two equivalent pixels, *i.e.* s_1, and s_2, on two images is generated by the phase differential at each co-registered pixel

$$z_{1,2} = s_1 . s_2^* = a_1 a_2 e^{i(\phi_1 - \phi_2)} \quad (1.7)$$

where, a_i and ϕ_i are the amplitude and phase of the pixels, respectively. The initial phase represents the difference in the round-trip traveling distance along the line-of-sight (LOS) direction plus the phase change due to the change in the scattering property of the ground

$$\phi_{init} = \phi_1 - \phi_2 = -\frac{4\pi[r_1(i,j) - r_2(i,j)]}{\lambda} + [\varepsilon_1(i,j) - \varepsilon_2(i,j)] \quad (1.8)$$

By assuming that the scattering phases remain the same ($\varepsilon_1(i,j) = \varepsilon_2(i,j)$), the phase change of a pixel between two images will be

$$\phi_{\text{init}} = \phi_1 - \phi_2 = -\frac{4\pi[r_1(i,j) - r_2(i,j)]}{\lambda} \tag{1.9}$$

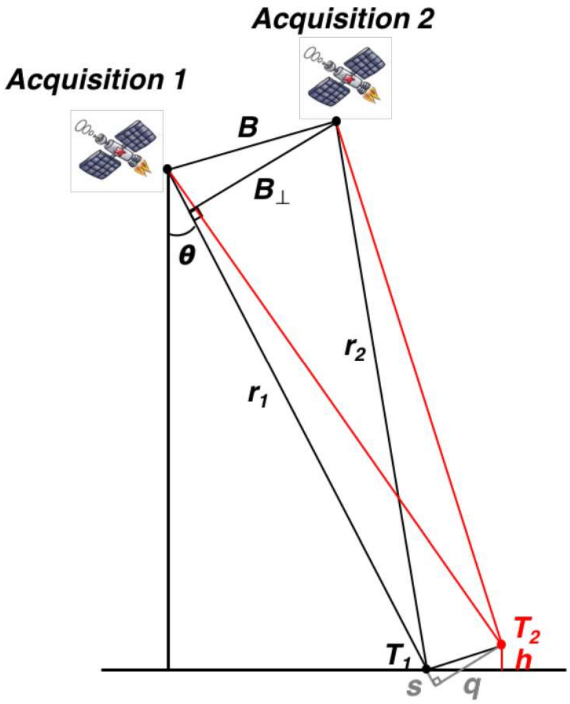

Figure 1.2. Sketch of InSAR geometry (modified from Lu and Dzurisin, 2014)

Due to the spatial baseline of the two acquisitions, there is a phase variation between two neighboring pixels, even over flat areas. The phase difference $\Delta\phi$ is a function of the slant range difference s and the height difference h

$$\Delta\phi = -\frac{4\pi}{\lambda}\frac{B_\perp s}{R\,tan(\theta)} - \frac{4\pi}{\lambda}\frac{B_\perp h}{R\,sin(\theta)} \tag{1.10}$$

where R is the range distance, θ is the look angle, and $B_\perp$ is the perpendicular (spatial) baseline between the two images. As mentioned previously, the first term of the equation (1.10) is due to the spatial separation of the two satellites and it should be reduced from the initial phase. The remaining part is called flatten interferometric phase

$$\Delta\phi_{flatten} = -\frac{4\pi}{\lambda}\frac{B_\perp h}{R\,sin(\theta)} \tag{1.11}$$

In the case where there is no deformation between the two images, the flatten phase can be used to extract topographic elevation model (DEM). On the other hand, if deformation happened between the two images, we have

$$\Delta\phi_{flatten} = -\frac{4\pi}{\lambda}\frac{B_\perp h}{R\,sin(\theta)} + \phi_{def} \tag{1.12}$$

Therefore, the flatten phase can be subtracted from the phase simulated from digital elevation model to obtain the deformation happen between the two images. Because the phase is wrapped modulo 2π, an unwrapping procedure has to be applied to retrieve the continuous phase changes.

1.3.1 Multi-looking and InSAR Coherence

The coherence of two complex SAR images u_1 and u_2, is defined as follows (Lu and Dzurisin, 2014; Lopes et al., 1992; Bamler and Just, 1993; Tough et al., 1993)

$$\gamma = \frac{E[u_1 u_2^*]}{\sqrt{E[|u_1|^2]E[|u_2|^2]}} = |\gamma| e^{i\varphi_0} \tag{1.13}$$

where φ_0 is the expected noise-free phase, u_2^* is the complex conjugate of the second image, and E[.] denotes the expectation value that in practice will be approximated with a sampled average (Lopes et al., 1992; Just and Bamler, 1994; Anxi et al., 2014). Hence, over statistically uniform areas, the sampled coherence can be computed as (Bamler and Just, 1993; Tough et al., 1993; Lee et al., 1994a; Lee et al., 1994b)

$$\hat{\gamma} = \frac{\sum_1^n u_1 u_2^*}{\sqrt{\sum_1^n |u_1|^2 \sum_1^n |u_2|^2}} = |\hat{\gamma}| e^{j(\varphi_0 + \varphi_n)} = |\hat{\gamma}| e^{i\varphi} \tag{1.14}$$

where $|\hat{\gamma}|$ and φ are the magnitude and phase of the multi-looked interferogram. The joint probability density function (PDF) of magnitude and phase of an interferogram depends on the number of looks and satisfies Wishart distribution. The marginal PDF of InSAR phase can be derived from the joint PDF (Just and Bamler, 1994; Lee et al., 1994a; Lee et al., 1994b; Davenport and Root, 1987; Bamler and Hartl, 1998; Tough et al., 1995) that is characterized

with a mean of φ_0 and a variance, which is a function of InSAR coherence value |γ | (Bamler and Hartl, 1998; Tough et al., 1995). Thus, we have

$$\varphi = \varphi_0 + \varphi_n \text{ with } E[\varphi] = \varphi_0 \tag{1.15}$$

where φ_n denotes a zero-mean additive noise, upon which its variance is independent of the magnitude φ (Bamler and Hartl, 1998). The expected value of interferometric phase is φ_0 regardless of the magnitude of changes, number of looks and the value of complex correlation coefficient (Lee et al., 1994a; Lee et al., 1994b; Davenport and Root, 1987; Bamler and Hartl, 1998).

1.4 InSAR time-series techniques

Conventional InSAR method can provide centimeter-level-precision deformation map. However, geometrical and temporal decorrelation, atmospheric artifacts, topographic errors, and unwrapping errors can limit its ability to accurately map the deformations. An interferometric phase has generally the following components

$$\Delta\phi_{ifg} = \Delta\phi_{def} + \Delta\phi'_{topo} + \Delta\phi_{atm} + \Delta\phi'_{orb} + \Delta\phi_{dc} + \Delta\phi_{noise} \tag{1.16}$$

where, $\Delta\phi_{def}$ is LOS deformation, $\Delta\phi'_{topo}$ is residual topographic phase (DEM error), which can be calculated by

$$\Delta\phi'_{topo} = -\frac{4\pi}{\lambda}\frac{B_{\perp}h'}{R\,sin(\theta)} \tag{1.17}$$

where h' is DEM error. $\Delta\phi_{atm}$ is atmospheric phase delay, $\Delta\phi'_{orb}$ is the residual orbit phase error induced by in-accurate orbit locations, $\Delta\phi_{dc}$ is the phase change due to the change in dielectric constant of the ground target, and $\Delta\phi_{noise}$ represents all other uncorrelated noise sources. The aim of time-series InSAR methods is to separate the interferometric phase components based on their characteristics in spatial and time domains. InSAR time-series techniques utilize a network of interferograms other than individual interferograms to estimate temporal evolution of surface deformation.

1.4.1 Small baseline SAR (SBAS)

The essential strategy taken in SBAS methods is to exploit small temporal and spatial baselines to minimize geometrical decorrelation and topographic error induced artifacts. This leads to more accurate deformation time-series. In addition, the SBAS methods often perform a spatial averaging to further decrease decorrelation. The solution of time-series phase values associated with the deformation for each selected coherent point is given by

$$\phi_N = (A^T\mathrm{A})^{-1}\,A^T\,\Delta\phi_M \tag{1.18}$$

where ϕ_N is the vector of the N unknown phase values associated with the cumulative deformation of N SAR images in time series, A is an M by N sparse matrix (Berardino et al., 2002), and $\Delta\phi_M$ is the vector of the M known phase values from M interferograms. Based on the prior knowledge of the deformation signal, phase inversion methods can be exploited. When the all the interferograms are connected and A is full rank, such as least-squares estimation (Schmidt and Bürgmann, 2003) can be used. Also, singular value decomposition (Berardino et al., 2002) can be used when interferograms are not connected and A is rank deficient (Berardino et al., 2002). The result is the temporal evolution of phase, *i.e.* deformation time-series.

1.4.2 Persistent Scattere Analysis

The persistent scatterer InSAR (PSI) technique (Ferrett et. al, 2000, 2001; Hooper et. al, 2004) identifies coherent radar signal (persistent scatterer, PS) in a stack of interferograms. This is done by discriminating coherent signal from incoherent contributions.

1.5 Soil moisture influence on InSAR phase, coherence, Closure phase

InSAR detects mm level deformation and provides valuable input to studies of earthquakes, volcanos, landslides, permafrost processes, and so on. Two SAR images taken at different times are combined to make an interferogram aiming to detect ground surface deformations as well as to generate DEMs. The surface characteristics between the two images, e.g. soil moisture and vegetation water content, are subject to changes. The temporal change in soil moisture as well as vegetation layer has been known to contribute to InSAR phase and decorrelation (*e.g.* Molan et al., 2020; Molan and Lu, 2020). The effect of the changes on InSAR phase and coherence can potentially impede accurate estimation of ground surface deformation.

Furthermore, in some cases such as landslides, permafrost and surface erosion, the processes and subsequent surface movements are closely related to the changes in soil moisture. For example, sudden landslides can happen right after heavy precipitation or rapid snow melt. Soil moisture is also in a close relationship with permafrost thawing and subsequent ground surface subsidence. Therefore, quantifying the influence of soil moisture on InSAR phase, and coherence is of great importance.

1.5.1 The effect of water content of surface medium on InSAR phase

The temporal change in soil moisture has been known to contribute to InSAR phase. The first reported signal of soil moisture on InSAR images has been reported in 1989 (Gabriel et al., 1989). One of the interferograms over agricultural field in California, generated using SEASAT data at the JET Propulsion Laboratory (JPL), featured phase changes corresponded to field boundaries. The observed phase was inferred to be related to soil moisture. Swelling characteristic of the soil convinced the authors to ascribe the phase change to surface movement (expansion), i.e. change in the travel path. Since then, soil moisture induced phase changes on interferograms from satellite SAR data (Nolan et al., 2003; Zhang et al., 2008; Barrett et al., 2012) and airborne and indoor experiments (Hajnsek and Prats, 2008; Nesti et al., 1995, 1998) have been reported.

New experimental studies, however, cast doubt on the expansion hypothesis. Rudant et al., 1996, in a laboratory experiment noted apparent subsidence over wetted soil and sprinkled planets. Hensley et al., 2011 and Morrison et al., 2011, also noticed that the phase change is larger than deformation and motion of the surface of the soil under study indicating that the observed phase cannot be caused by a realistic deformation.

One explanation for soil moisture induced phase changes is *penetration* hypothesis. Soil moisture content governs the depth at which electromagnetic wave attenuates, *i.e.* depth of penetration (Tsang et al., 2000). The depth of penetration is the depth at which the two-way propagation leads to reduction in power by a factor of 1/e. According to this hypothesis, penetration depth decreases by increasing soil moisture (Nolan, 2003). Note that the influence of soil moisture change on InSAR coherence is not clear in this hypothesis.

Recently, *Dielectric* hypothesis has been introduced to explain soil moisture induced phase changes. Based on this hypothesis, it is the dielectric characteristic of the medium (soil) that governs soil moisture induced phase change on interferograms. The change in the water content of vegetation layer on InSAR phase is also known to be similar to the effect of soil moisture changes on phase (Hensley et al., 2011) since the dielectric constant of both soil and vegetation layer depend on water content (Tsang et al., 2000). As water content of a medium (soil for example) between two images changes, the dielectric constant of the medium changes. The change in the dielectric constant results in a change in the wavenumber. The change in the real part of dielectric constant gives rise to the increase in wavenumber, i.e. shorter spacing of the wavefronts (Zwieback et al., 2015a). This in turn leads to phase increase as water content increases. The imaginary part of the dielectric constant governs the absorption of the electromagnetic wave by depth. The absorption increases by increasing water content. However, it is the real part of the dielectric constant that give rise to phase changes (De Zan et al., 2014).

A broad range of studies from controlled experiments to observational studies have been conducted to quantify the effect of soil moisture on InSAR phase and coherence (Zwieback et al., 2015b). A number of this studies provided mathematical models ranging from simple analytical expression (e.g. De Zan et al., 2014) to more complicated numerical solutions to Maxwell's

equations (e.g. Zwieback et al., 2015a). Recently, Zwieback et al., 2015a, empirically analyzed the applicability of the aforementioned hypotheses. Using the data of two L-band airborne campaigns, the authors revealed that soil moisture change induced phase was not consistent with the penetration depth, or soil swelling hypotheses but only with dielectric volume scattering mechanism.

1.5.2 The effect of the changes in water content of surface medium on InSAR coherence

InSAR has been successfully used to detect surface deformation due to various mechanisms, such as volcanism, subsidence, permafrost, and landslides (Ferrett et. al, 2001; Molan et al., 2018a; Rykhus and Lu, 2008; Liu et al, 2010). So far numerous methods and approaches have been developed to improve InSAR performance. However, temporal decorrelation, regardless of the processing methodology, is one of the major obstacles for all InSAR applications especially over vegetated areas. The main sources of the loss of coherence, i.e. decorrelation, are temporal decorrelation, spatial decorrelation, volume decorrelation, thermal decorrelation, and processing errors (e.g. Zebker and Villasenor, 1992; Just and Bamler, 1994). Generally, InSAR coherence decreases by increasing spatial and temporal baselines between two images.

InSAR coherence is sensitive to the changes in surface backscattering, which is dominated by surface dielectric constant and roughness on the scale of the radar wavelength (Simard et al., 2012; Rocca, 2007; Luo et al., 2001; Lu and Dzurisin, 2014). It has been documented that temporal coherence can be influenced by temporal variations of surface backscattering due to changes in soil moisture, snow depth, surface roughness, and vegetation biomass (Scott et al., 2017; Zhang et al., 2003, 2008; Borgeaud and Wegmueller, 1996; Morishita and Hanssen, 2015). Simard et al. (2012) found precipitation events to be the main cause of

temporal decorrelation using fully polarimetric airborne L-band acquisitions over forested landscapes with up to 9 days temporal baselines,. Also, they argued that correlation decreases by increasing canopy height regardless of forest type and polarization. Zwieback et al. (2015b) evaluated soil moisture effects on L-band InSAR and revealed that the phase difference between two SAR images increased with increasing soil moisture difference, whereas the coherence decreased at the same time. Zhang et al. (2008), in a case study using C-band ERS SAR data, assessed the relationship between InSAR coherence and soil moisture and inferred that the relation between the two may satisfy an exponential distribution.

1.6 Significance

InSAR detected displacement can be systematically biased by the changes in soil moisture. Ordinary InSAR analyses rarely take into account soil moisture influences on InSAR phase, intensity, and coherence. However, soil moisture-induced uncompensated biases in the spatial and temporal patterns of InSAR detected displacement can limit its applicability and impacts its reliability and robustness. The effort to quantify the influence of soil moisture of InSAR measurements, in addition to compensate the influence of soil moisture changes, can also open new window into soil moisture retrieval and soil structure properties estimation.

The quality, and quantity of the induced changes can be modeled or statistically assessed using adequate number of interferograms. Potentially, modeling soil moisture influence on InSAR phase and SAR intensity changes provides a means to compensate soil moisture phase artifacts and also to retrieve surface soil moisture. Also, modeling temporal decorrelations provides a means to understand and estimate a wide variety of surficial processes, such as vegetation growth, permafrost freezing and thawing, and soil moisture and vegetation layer induced effects (Simard et al., 2012).

1.7 Chapter summaries and contributions

Chapter 2, 3, 4, 5, and 6 are written for peer reviewed publication. Chapter 2, 3, 4, and 5 include my research published in two journals: *remote sensing* (Molan et al., 2018a, and Molan et al, 2018b) and *IEEE Transaction of Geosciences and Remote Sensing* (Molan and Lu, 2020a, and Molan et al., 2020). Chapter 6 is submitted to a peer-reviewed journal (*Remote Sensing*) (Molan and Lu, 2020b). Chapter 7 highlights the findings of this dissertation and discuss topics of future work.

Chapter 2: This chapter provides a case study where InSAR was used for ground surface deformation mapping over discontinuous permafrost in interior Alaskan Boreal Forest (Molan et al, 2018a). The discontinuous permafrost zone is one of the world's most sensitive areas to climate change. Alaskan boreal forest is underlain by discontinuous permafrost, and wildfires are one of the most influential agents negatively impacting the condition of permafrost in the arctic region. Using InSAR of Advanced Land Observation Satellite (ALOS) Phased Array type L-band Synthetic Aperture Radar (PALSAR) images, we mapped extensive permafrost degradation over interior Alaskan boreal forest in Yukon Flats, induced by the 2009 Big Creek wildfire. Our analyses showed that fire-induced permafrost degradation in the second post-fire thawing season contributed up to 20 cm of ground surface subsidence. We generated post-fire deformation time series and introduced a model that exploited the deformation time series to estimate fire-induced permafrost degradation and changes in active layer thickness. The model showed a wildfire-induced increase of up to 80 cm in active layer thickness in the second post-fire year due to pore-ice permafrost thawing. The model also showed up to 15 cm of permafrost degradation due to excess-ice thawing with little or no increase in active layer thickness. The uncertainties of the estimated change in active layer thickness and the thickness of thawed excess ice permafrost are

27.77 and 1.50 cm, respectively. Our results demonstrate that InSAR-derived deformation measurements along with physics models are capable of quantifying fire-induced permafrost degradation in Alaskan boreal forests underlain by discontinuous permafrost. Our results also have illustrated that fire-induced increase of active layer thickness and excess ice thawing contributed to ground surface subsidence.

Chapter 3: This chapter provides a model for L-band InSAR temporal coherence (Molan et al., 2018b). InSAR provides capability to detect surface deformation. Numerous processing approaches have been developed to improve InSAR results and overcome its limitations. Regardless of the processing methodology, however, temporal decorrelation is a major obstacle for all InSAR applications especially over vegetated areas and dynamic environments such as Interior Alaska. Temporal coherence is usually modeled as a univariate exponential function of temporal baseline. It has been, however, documented that temporal variations in surface backscattering due to the change in surface parameters, i.e. dielectric constant, roughness, and the geometry of scatterers, can result in gradual, seasonal, or sudden decorrelations and loss of InSAR coherence. The coherence models introduced so far have largely neglected the effect of the temporal change in backscattering on InSAR coherence. Here, we introduce a new temporal decorrelation model that considers changes in surface backscattering by utilizing the relative change in SAR intensity between two images as a proxy for the change in surface scattering parameters. The model also takes into account the decorrelation due to the change in snow depth between two images. Using ALOS-2 PALSAR-2 data, the model has been assessed over forested and shrub landscapes in Delta Junction, Interior Alaska. The model decreases the RMS error of temporal coherence estimation from 0.18 to 0.09 in average. The improvements made by the model has been statistically proved to be significant with 99% confidence level. Also, the model

shows that the coherence of forested area is more prone to changes in backscattering than shrub landscape. The model is based on L-band data and may not be expanded to C-band or X-band InSAR observations.

Chapter 4: An analytical model for soil moisture-induced SAR intensity and InSAR phase changes is provided in this chapter (Molan and Lu, 2020a). A broad range of studies have been conducted so far to quantify the effect of soil moisture on SAR intensity and InSAR phase. The introduced models are either intensity or interferometric models, and there is no single scattering model that can estimate both intensity and phase changes, indicating the subject is poorly understood. Here, we quantify the influence of soil moisture on InSAR phase and SAR intensity by employing a volume scattering model. We model soil as a collection of randomly distributed independent point scatterers embedded in a homogeneous background. Our volume scattering model successfully estimates SAR intensity and InSAR phase changes due to soil moisture changes. In addition to soil moisture changes, the model also takes into account the scatterers' size and their volumetric fraction. This may open new window in the studying of soil structure using SAR images and InSAR methods. Our results indicate that the structure of soil manipulates the way soil moisture alters the SAR intensity and InSAR phase. The model has been evaluated against field soil moisture measurements and shown to be successful in modeling InSAR phase and SAR intensity.

Chapter 5: This chapter provides the study dedicated to assess the influence of statistical properties of intensity and phase of pixels of multi-looked phase, coherence and closure phase (Molan et al., 2020). Non-zero closure phase exists in multi-looked pixels. We study the influence of statistical properties of intensity and phase changes of single-looked pixels on multi-looked phase and coherence. By quantifying the extent of their influences on phase triplet, we

show in this paper that the statistical properties of intensity of pixels within a multi-looking window can induce changes in interferometric phase and coherence and contribute to non-zero closure phase. We demonstrate that the intensityinduced changes increase by increasing the standard deviation of phase changes, dispersion index of intensity, and the correlation between intensity and phase changes. We have used ALOS PALSAR, ALOS-2 PALSAR-2, and Sentinel-1 images to generate real and semi-synthetic interferograms to assess our findings. The semi-synthetic interferograms are produced by pairing real SAR data and synthetic SAR data; the synthetic SAR data is generated from the real data by adding random vectors with predefined average changes of phase and intensity. Our results show that closure phase is only a function of the statistical properties of the phase and intensity of pixels and does not possess the information about the magnitude of physical changes. This casts doubt on the effectiveness of methods that exploit phase triplet as a means to estimate soil moisture or any other deforming or non-deforming changes.

Chapter 6: This chapter is written to be submitted as a paper to *Remote Sensing Journal* (Molan and Lu, 2020b). This work provides a statistical assessment of the influence of soil moisture on InSAR coherence and closure phase and answers the question whether or not InSAR coherence and closure phase can be used for soil moisture estimation. To answer the question whether InSAR coherence and closure phase can be sued to estimate soil moisture changes, we studied the influence of the statistical properties of soil moisture changes on InSAR coherence and closure phase. We generated semi-synthetic multi-looked interferograms, which pairs *n* real single-looked pixels with *n* synthetic single-looked pixels. The synthetic pixels are generated from the real pixels by applying soil moisture changes with pre-defined mean and standard deviation of changes. Our results show that the diversity of soil moisture values within the multi-

look window gives rise to decorrelations, multi-looked phase artifact, and consequently non-zero phase triplet. It is shown that decorrelation, and closure phase increase by increasing the diversity of soil moisture changes within the multi-look window. We showed that compared to soil moisture changes, non-soil moisture changes can lead to larger decorrelations and closure phases. We also show that the diversity of phase changes, decorrelation, and closure phase are correlated with land cover type. We concluded that closure phase and InSAR coherence are independent of the magnitude of soil moisture changes and are inappropriate tools to estimate soil moisture changes.

Chapter 7: This chapter provides conclusions and future works.

References

Hanssen, R. 2001. Radar Interferometry: Data Interpretation and Error Analysis, vol. 2. Dordrecht, The Netherlands: Kluwer.

Lu, Z., and D. Dzurisin. 2014. InSAR Imaging of Aleutian Volcanoes: Monitoring a Volcanic arc from Space, Geophysical Sciences, Springer Praxis Books, Springer: Chichester, UK, 2014, p. 390.

Lopes A. et al. 1992. Phase difference statistics related to sensor and forest parameters. In *Proc. Int. Geosci. Remote Sensing Symp*. (IGARSS'92) Houston, TX, 1992, pp. 779-781.

Bamler, R., and D. Just. 1993. Phase statistics and decorrelation in SAR interferograms. *IEEE Geosci.* Remote *Sens. Symp.*, 980-984. 15.

Tough, R. J. A., D. Blacknell, and S. Quegan. 1994. Estimators and distributions in single and multi-look polarimetric and interferometric data. *IEEE Geosci. Remote Sens. Symp.*, 4, 2176-2178. 17.

Just, D., and R. Bamler. 1994. Phase statistics of interferograms with applications to synthetic aperture radar. *Applied Optics*, 33(20), 4361-4368. doi: 10.1364/AO.33.004361

Anxi, Y., W. Haijun, D. Zhen, and H. Haifeng. 2014. Amplitude and Phase Statistics of Multi-look SAR Complex Interferogram. *Defense Science Journal*, Vol. 64, No. 6, 2014, pp. 564-570, DOI : 10.14429/dsj.64.4747

Lee, J. S., A. R. Miller, and K. W. Hoppel. 1994, Statistics of phase difference and product magnitude of multi-look processed Gaussian signals. *Waves in Random Media*, 4(3), 307-319. doi: 10.1088/0959-7174/4/3/006 18.

Lee, J. S., K. W. Hoppel, and S. A. Mango. 1994. Intensity and phase statistics of multi-look polarimetric and interferometric SAR imagery. *IEEE Trans. Geosci. Remote Sens.*, 32(5), 1017-1028. doi: 10.1109/36.312890

Davenport, Jr., W. B., and W. L. Root. 1987. An Introduction to the Theory of Random Signals and Noise. 1st ed. (Institute of Electrical and Electronics Engineers, New York), Chap. 8, pp. 158-165

Bamler, R., and P. Hartl. 1998. Synthetic Aperture Radar Interferometry. *Inverse Problems*, Vol. 14, R1.

Tough, R. J. A., D. Blacknell, and S. A. Quegan. 1995. Statistical description of polarimetric and interferometric synthetic aperture radar data. In *Proceedings of the Royal Society of London*. Series A: Mathematical and Physical Sciences, 449(1937), 567-589

Berardino, P., G. Fornaro, R. Lanari, and E. Sansosti. 2002. A new algorithm for surface deformation monitoring based on small baseline differential SAR interferograms. *IEEE Transactions on Geoscience and Remote Sensing*,40, 2375–2383.

Schmidt, D. A., and R. Bürgmann. 2003. Time-dependent land uplift and subsidence in the Santa Clara valley, California, from a large interferometric Synthetic Aperture Radar data set. *J. Geophys. Res.,* 108, 2416, doi: 10.1029/2002JB002267, B9.

Ferretti, A., C. Prati, and F. Rocca. 2000. Nonlinear subsidence rate estimation using permanent scatterers in differential SAR interferometry. *IEEE Transactions on Geoscience and Remote Sensing,* 38(5), 2202–2212.

Ferretti, A., C. Prati, and F. Rocca. 2001. Permanent scatterers in SAR interferometry. IEEE Transactions on Geoscience and Remote Sensing, 39, 8–20.

Hooper, A., H. Zebker, B. Segall, and B. Kampes. 2004. A new method for measuring deformation on volcanoes and other natural terrains using InSAR persistent scatterers. *Geophys. Res. Lett.,* 31, L23611.

Gabriel, R. Goldstein, and H. Zebker. 1989. Mapping small elevation changes over large areas: Differential radar interferometry. J. Geophys. Res., vol. 94, no. B7, pp. 9183–9191.

Nolan, M., D. R. Fatland, and L. Hinzman. 2003. DInsar measurement of soil moisture. IEEE Trans. Geosci. Remote Sens., vol. 41, no. 12, pp. 2802–2013.

Zhang, T., Q. Zeng, Y. Li, and Y. Xiang. 2008. Study on relation between InSAR coherence and soil moisture. In Proc. ISPRS Congr., vol. 37, pp. 131–134.

Barrett, B., E. Dwyer, and P. Whelan. 2012. The use of C- and L-band repeatpass interferometric SAR coherence for soil moisture change detectionin vegetated areas. Open Remote Sens. J., vol. 5, no. 1, pp. 37–53.

Hajnsek, I., and P. Prats. 2008. Soil moisture estimation in time with DInSAR. In Proc. *IEEE IGARSS*, vol. III, pp. 546–549.

Nesti, G., D. Tarchi, and J.-P. Rudant. 1995. Decorrelation of backscattered signal due to soil moisture changes. In Proc. Int. Geosci. Remote Sens. Symp., vol. 3, pp. 2026–2028.

Nesti, G., D. Tarchi, D. Despan, J.-P. Rudant, A. Bedidi, P. Borderies, and E. Bachelier. 1998. Phase shift and decorrelation of radar signal related to soil moisture changes. In Proc. 2nd ESA Int. Workshop Retrieval Bio- Geo-Phys. Parameter SAR Data Land Appl., pp. 423–430.

Rudant, J.-P., A. Bedidi, R. Calonne, D. Massonnet, G. Nesti, and D. Tarchi. 1996. Laboratory experiment for the interpretation of phase shift in SAR interferograms. In Proceedings of *FRINGE*.

Hensley, S., T. Michel, J. Van Zyl, R. Muellerschoen, B. Chapman, S. Oveisgharan, Z. S. Haddad, T. Jackson, and I. Mladenova. 2011. Effect of soil moisture on polarimetric-interferometric repeat pass observations by UAVSAR during 2010 Canadian Soil Moisture campaign. In Proc. *IEEE IGARSS*, pp. 1063–1066.

Morrison, K., J. C. Bennett, M. Nolan, and R. Menon. 2011. Laboratory measurement of the DInSAR response to spatiotemporal variations in soil moisture. *IEEE Trans. Geosci. Remote Sens*., vol. 49, no. 10, pp. 3815–3823.

Tsang, L., J. A. Kong, and K. H. Ding. 2000. Scattering of electromagnetic waves: Theories and applications. *John Wiley & Sons.*

Nolan, M. 2003. Penetration depth as a DInSAR observable and proxy for soil moisture. *IEEE Transactions on Geoscience and Remote Sensing*, 41, 532–537.

Zwieback, S., S. Hensley, and I. Hajnsek. 2015a. A Polarimetric First-Order Model of Soil Moisture Effects on the DInSAR Coherence. *Remote Sens.*, 7, 7571–7596, doi: 10.3390/rs70607571

De Zan, F., A. Parizzi, P. Prats-Iraola, and P. Lopez-Dekker. 2014. A SAR interferometric model for soil moisture. *IEEE Transactions on Geoscience and Remote Sensing*, 52, 418–425.

Zwieback, S., S. Hensley, and I. Hajnsek. 2015. Assessment of soil moisture effects on L-band radar interferometry. *Remote Sens. Environ*. 2015, 164, 77–89, doi:10.1016/j.rse.04.012.

Molan, Y.E., J.-W. Kim, Z. Lu, B. Wylie, and Z. Zhu. 2018a. Modeling Wildfire-Induced Permafrost Deformation in an Alaskan Boreal Forest Using InSAR Observations. Remote Sens., 10, 405.

Rykhus, R., and Z. Lu. 2008. InSAR detects possible thaw settlement in the Alaskan Arctic Coastal Plain. *Can. J. Remote Sens*., 34, 100–112.

Liu, L., T. Zhang, and J. Wahr. 2010. InSAR measurements of surface deformation over permafrost on the North Slope of Alaska. *J. Geophys. Res*., 115, F03023, doi:10.1029/2009JF001547.

Zebker, H., and J. Villasenor. 1992. Decorrelation in interferometric radar echoes. *IEEE Trans. Geosci. Remote Sens*., 45, 950–959.

Simard, M., S. Hensley, and M. Lavalle. 2012. An empirical assessment of temporal decorrelation using the uninhabited aerial vehicle synthetic aperture radar over forested landscapes. *Remote Sens.*, 4, 975–986.

Rocca, F. 2007. Modeling Interferograms Stacks. IEEE Trans. Geosci. Remote Sens., 45, 3289–3299.

Luo, X., J. Askne, G. Smith, and P. Dammert. 2001. Coherence characteristics of RADAR signals from rough soil. *Prog. Electromagn. Res*., 31, 68–88.

Zhang, L., J. Shi, Z. Zhang, and K. Zhao. 2003. The estimation of dielectric constant of frozen soil-water mixture at microwave bands. In Proceedings of the *IEEE International Geoscience and Remote Sensing Symposium*, Toulouse, France, 21–25 July 2003, IEEE: Piscataway, NJ, USA, 2003; pp. 2903–2905.

Zhang, T., Q. Zeng, Y. Li, and Y. Xiang. 2008. Study on relation between InSAR coherence and soil moisture. In Proc. *ISPRS Congr*., vol. 37, pp. 131–134.

Borgeaud, M., and U. Wegmueller. 1996. On the use of ERS SAR interferometry for the retrieval of geoand bio-physical information. In Proceedings of the '*Fringe 96'* Workshop on ERS SAR Interferometry, 30 September–2 October 1996, Zurich, Switzerland, pp. 83–94.

Morishita, Y., and R.F. Hanssen. 2015. Temporal Decorrelation in L-, C-, and X-band Satellite Radar Interferometry for Pasture on Drained Peat Soils. *IEEE Trans. Geosci. Remote Sens*., 53, 1096–1104.

Scott, C.P., R.B. Lohman, and T.E. Jordan. 2017. InSAR constraints on soil moisture evolution after the March 2015 extreme precipitation event in Chile. *Sci Rep* 7, 4903. https://doi.org/10.1038/s41598-017-05123-4

Molan, Y.E., J.-W. Kim, Z. Lu, P. Agram. 2018b. L-Band Temporal Coherence Assessment and Modeling Using Amplitude and Snow Depth over Interior Alaska. *Remote Sens*. 10, 150.

Molan, Y.E., and Z. Lu. 2020a. Modeling InSAR Phase and SAR intensity Changes Induced by Soil Moisture, *IEEE TGRS*, DOI: 10.1109/TGRS.2020.2970841.

Molan, Y.E., Z. Lu, and J-W. Kim. 2020. Influence of the statistical properties of phase and intensity on closure phase, *IEEE TGRS*.

Molan, Y.E., and Z. Lu. 2020b. Can InSAR coherence and closure phase be used to estimate soil moisture changes? *Remote Sensing*.

CHAPTER 2

INSAR ANALYSIS: A CASE STUDY OF PERMAFROST DEFORMATION MAPPING AND MODELING

Molan, Y.E., J.-W. Kim, Z. Lu, B. Wylie, and Z. Zhu. 2018. Modeling Wildfire-Induced Permafrost Deformation in an Alaskan Boreal Forest Using InSAR Observations. Remote Sens., 10, 405.

2.1 Introduction

Permafrost plays a significant role in landscape stability, carbon cycling, and socioeconomic development, and is key to regulating biological, hydrological, geophysical, and biogeochemical processes (Zhang et al., 2012). Roughly 37% of the Northern Hemisphere permafrost occurs in western North America, mainly in Alaska and northern Canada, but also further south in the Rocky Mountains (Zhang et al., 1999). A huge amount of carbon is stored in permafrost (Apps et al., 1993), roughly twice as large as the amount of carbon in the atmosphere (Strauss et al., 2012); therefore, disturbance of the permafrost can significantly contribute to climate change (Apps et al., 1993). In addition, permafrost is structurally important, and its thawing has been known to cause erosion, disappearance of lakes, landslides, and ground subsidence. The active layer, defined as the top layer of ground in areas underlain by permafrost, plays a key role in land surface processes in cold regions and is subject to annual thawing and freezing and subsequent subsidence and uplift, respectively (Harris et al., 1998).

Field surveys (including surface geophysical collections), model simulations, and remote sensing observations are used to obtain regional variation of active layer thickness (ALT) (Streletskiy et al., 2012). ALT is usually directly measured by using a metal rod inserted into the soil to measure the depth of thawing (e.g. Machay, 1977). However, the measurement should be done at the end of the thawing season and, if possible, in stone-free soils. Surface geophysical datasets as well as ground-penetrating radar data can also be used to provide very high resolution and accurate estimates of ALT (e.g. Hubbard et al., 2013). Although ground-based ALT measurements are accurate, they provide a spatially limited sampling of a parameter that has significant spatial variability (Liu et al., 2012). At regional scales, using empirical and statistical relationships, ALT can be modeled at coarser spatial resolution by extrapolating ground-based measurements with air temperature, ground temperature, elevation, and surface vegetation (Nelson et al., 1997; Shiklomanov et al., 1999; Panda et al., 2010; Gangodagamage et al., 2014).

In contrast, remote sensing estimation of ALT usually uses Interferometric Synthetic Aperture Radar (InSAR) measurements to estimate ALT from seasonal ground deformation (Schaefer et al., 2015). In the recent years, a few attempts have been made to estimate and model ALT using InSAR. This method eliminates the need to define an empirical or statistical relationship with probing data (Schaefer et al., 2015). InSAR provides an all-weather, day-or-night capability to remotely sense mm–cm surface deformation with a high spatial resolution of tens of meters or better (e.g. Massonnet et al., 1998; Bürgmann et al., 2000; Simons and Rosen, 2007; Lu and Dzurisin, 2014, Kim et al., 2017). Able to collect Synthetic Aperture Radar (SAR) images over a large-scale area, InSAR has proven very useful for deformation monitoring over permafrost in Alaska (e.g. Liu et al., 2012; Rykhus and Lu, 2008; Liu et al., 2010; Short et al., 2011; Liu et al., 2014a; Liu et al, 2015). Liu et al. (Liu et al., 2010) applied InSAR using ERS-1

and -2 data to monitor surface deformation near Prudhoe Bay on the Alaskan North Slope. They studied long-term permafrost-related surface subsidence and argued that the seasonal subsidence and long-term subsidence trends are due to thaw settlement of the active layer and thawing of ice-rich permafrost near the permafrost table, respectively. Liu et al., 2012, estimated the 1992–2000 average ALT of the North Slope of Alaska from InSAR-derived surface subsidence by using the SAR images for thaw season only. By comparing TerraSAR-X, RADARSAT-2, and ALOS PALSAR interferometry, Short et al., 2011, concluded that ALOS-PALSAR provides the most promising data for permafrost degradation monitoring. Liu et al., 2014a, conducted InSAR time-series analysis using ALOS-PALSAR data to detect seasonal thaw settlement in individual drained thermokarst lake basins. Liu et al., 2015, demonstrated the capability of using L-band PALSAR interferograms with short perpendicular baselines to minimize the adverse effects of coherence loss, which made it possible to quantify thermokarst. Liu et al., 2014b, conducted InSAR time series analysis using ALOS PALSAR data to detect an increase in surface subsidence caused by Arctic tundra fire in a permafrost region of north Alaska. Iwahana et al., 2016, investigated the northern part of the Anaktuvuk River fire scar with a two-path differential InSAR technique and measured up to 6.2 cm/year post-fire subsidence within burned tundra relative to surrounding off-scar tundra using three independent InSAR pairs of ALOS PALSAR data. In addition to the use of InSAR to quantify fire-induced permafrost deformations (e.g. Iwahana et al., 2016), some researchers have recently exploited LiDAR datasets to quantify permafrost degradation. Jones et al., 2015, for example, investigated the impact of the large and severe Anaktuvuk River tundra fire on potential, post-fire thermokarst development using two airborne LiDAR datasets acquired two and seven years after the fire.

Among remote sensing methods, optical methods provide the unique opportunity to map fire scar and assess its severity. Spectral analysis of optical images can facilitate fire scar and severity mapping (Lutes et al., 2006; Parks et al., 2014). Optical methods utilize the fire-induced changes in the spectral behavior of pre- and post-fire vegetation over fire scar as well as the differences between the post-fire reflective characteristics of vegetation and off-scar surrounding environment. So far, a number of indices for burned area mapping, including differenced normalized burn ratio (dNBR) (Lutes et al., 2006), relativized dNBR (RdNBR), and relativized burn ratio (RBR) (Parks et al., 2014), have been developed.

The objective of this study is two-fold. First, we intend to demonstrate the capability of L-band InSAR to monitor and quantify fire-induced permafrost deformations over interior Alaskan boreal forest. Second, we introduce a model for the fire-induced post-fire permafrost deformations. To this end, we used L-band ALOS PALSAR data to map permafrost deformations over the Big Creek fire scar, Alaska, and then introduced a model to estimate wildfire-induced changes in ALT, exploiting InSAR-detected deformations in a time series over the fire scar. The InSAR-detected deformation is then used to model fire-induced permafrost deformations in boreal forest. In boreal forest, wildfire is one of the most important agents affecting permafrost. Since a huge amount of carbon is stored in permafrost, the disturbance of the permafrost can significantly contribute to global climate change. In addition, permafrost thawing has been known to cause erosion, disappearance of lakes, landslides, and ground subsidence (e.g. Streletskiy et al., 2012; Liu et al., 2012; Panda et al., 2010). In a study using airborne LiDAR, Jones et al., 2015, assessed fire-induced thermokarst development and concluded that in regions with ice-rich permafrost in the Arctic, the impact of tundra fires for initiating widespread thermokarst development is greater than what has been estimated to so far.

Our study area, which is underlain by discontinuous permafrost (Jorgenson et al., 2008) and located in the Alaskan Yukon River Basin, includes the 2009 Big Creek wildfire. The fire damaged ~686 km^2 from 18 July 2009, to 18 August 2009 (Figure 2.1). The Alaskan Yukon River Basin is mainly composed of upland and lowland evergreen forests, bottomland deciduous forest, emergent and herbaceous wetlands, upland and lowland tundra, and alpine shrub (Spetzman, 1963) and is predominantly underlain by discontinuous permafrost (Jorgenson et al., 2008). The near surface permafrost probability over the study area ranges from ~10% to ~70% (Pastick et al., 2015). The study area, a silty upland, was dominated by black spruce. Black spruce tends to be underlain by permafrost (Viereck et al., 1992) since black spruce stands generally contain a continuous insulating layer of moss and lichens (Johnstone et al., 2010). The area is in a region with low annual precipitation (about 170 mm) and particularly strong variations in seasonal temperature. In Yukon Flats, the average daily temperatures in winter and summer range from −34 °C to about −24 °C and from about 0 to about 22 °C, respectively (Gallant et al., 1995).

First, we applied InSAR to measure ground surface deformations between interferometric pairs ranging from September 2009 to March 2011. Then, using the small baseline subset (SBAS) method (particularly, the TimeFun algorithm (Hetland et al., 2012)), we inverted the measured InSAR phases to deformation time series. Finally, we applied our model to estimate fire-induced changes in ALT using the deformation time series. The rest of this paper is organized as follows. The InSAR analyses and results are provided in Sections 2 and 3, respectively. In Section 4.1., we present our model and estimate wildfire-induced changes in ALT. Validation of results and estimation of uncertainties are included in Section 4.2., followed by conclusions in section 5.

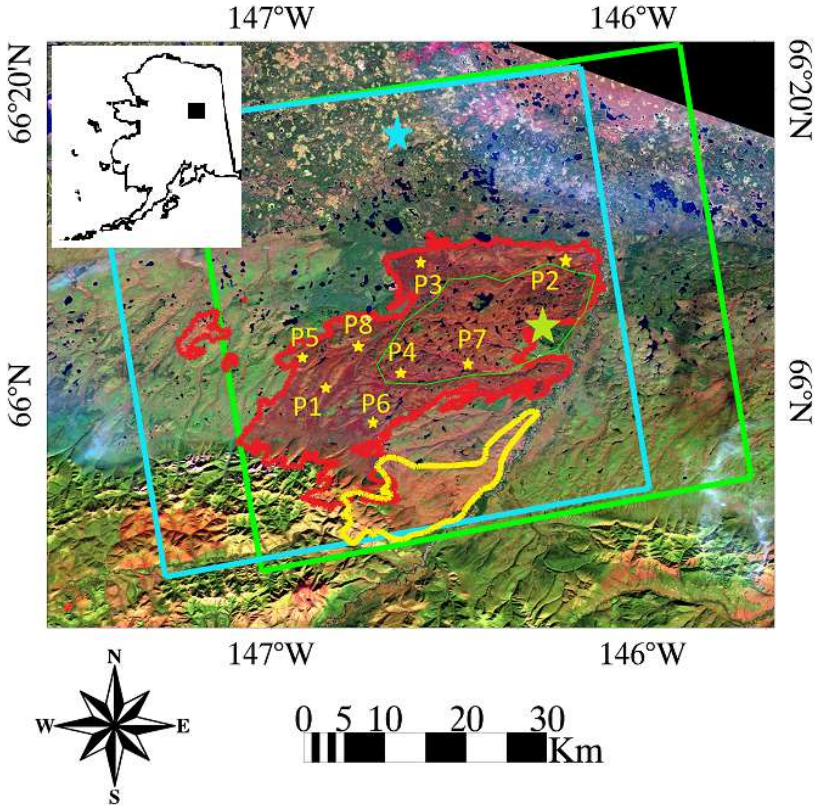

Figure 2.1. The map of 2009 (red) and 2005 (yellow) wildfire perimeters in the study area (The Bureau of Land Management Alaska Fire Service (http://afs.ak.blm.gov/)). The study area covered by paths 252 and 251 (ALOS) are boxed in cyan and green, respectively. Points P1, P2, P3, P4, P5, P6, P7, and P8 are selected points to evaluate InSAR results. The reference point and the location of ground truth measurements are shown by the cyan and green stars, respectively. The area in a green polygon is densely populated by lakes and ponds. The background image of figure is a post-fire false color composite of Landsat ETM+ bands 7 (R), 4 (G), and 2 (B).

2.2 Methods

SAR returns must be coherent to retrieve useful information from interferograms (e.g. Lu et al., 2005). An InSAR coherence estimation image is a cross-correlation product of two co-registered complex-valued SAR images (Lu et al., 2005), and loss of interferometric coherence is the major obstacle for applying InSAR to monitor permafrost deformations in forested areas. InSAR coherence tends to increase with radar wavelength due to the greater capability to

penetrate vegetation cover or forest canopy. For this reason, we employed L-band (23.6 cm wavelength) Japanese ALOS for InSAR analysis in the study area, which is mostly forested and underlain by permafrost. However, our inspection of InSAR coherence over the study area confirmed a strong fire-induced coherence loss that made us unable to quantify surface deformations using interferograms pairing pre- and post-fire SAR images. Figure 2.2 shows the ALOS coherence estimate between 17 July 2007 (pre-fire) and 06 September 2009 (post-fire) images. After the wildfire in 2009, the InSAR coherence decreased due to significant changes on the vegetation cover resulting in altered scattering characteristics from ground surface. When coherence was radically reduced to near zero values, we could not obtain useful information on the ground deformation. However, the coherence map (Figure 2.2) itself still can help delineate the extent of the fire scars.

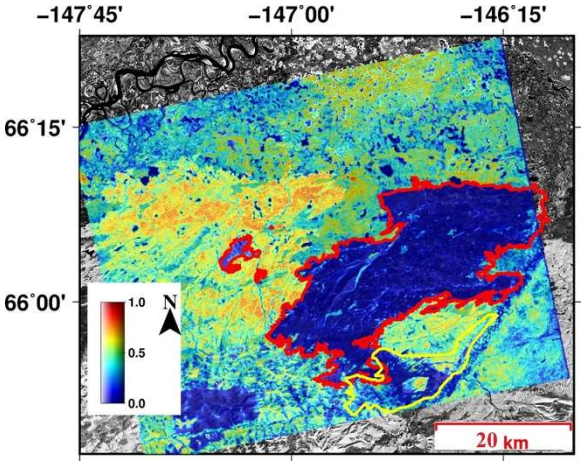

Figure 2.2. ALOS coherence estimate between 17 July 2007 and 06 September 2009 (path 252). Note near zero values over the fire scare, which indicates complete loss of InSAR coherence.

Twelve HH polarized ALOS PALSAR single look complex (SLC) images, eight Fine Beam Single polarization (FBS, 28 MHz bandwidth) and four Fine Beam Dual polarization

(FBD 14 MHz bandwidth), from September 2009 to March 2011 with radar look angle of 38.76° and slant range and azimuth pixel sizes of 4.68 m (in SAR coordinates) and 3.13 m, respectively, were used in this study. First, assisted by high-resolution (12 m) TanDEM-X DEM data, all SLC images have been co-registered based on a single master image, which optimizes the geometric and temporal coherence of the interferogram stack. The resampled SLC images were multi-looked by 6 and 14 in range and azimuth directions, respectively, and then used to generate initial interferograms with ground pixel sizes of about 45 m. Then, flat earth and topography phase components from initial interferograms have been removed using TanDEM-X DEM, and the interferograms were unwrapped using the Minimum Cost Flow (MCF) method (Costantini, 1998). Also, atmospheric correction to remove stratified tropospheric artifacts that tend to correlate with topography has been done on the interferograms by evaluating linear regression of unwrapped phase with respect to height.

The InSAR method quantifies ground surface deformation, but the geometrical and temporal decorrelations and atmospheric artifacts can affect the results. Over the last decade, a variety of SBAS algorithms have been developed and successfully applied in various ground deformation monitoring applications (e.g. Berardino et al., 2002) aiming to generate deformation time series with artifacts removed. Generally, small baseline differential interferograms are generated first and then time series analysis is conducted (e.g. Gong et al., 2016). In this research, the TimeFun method, adapted from the Multiscale InSAR Time Series (MInTS) algorithm (Hetland et al., 2016) and implemented in the Generic InSAR Analysis Toolbox (GIAnT) (Agram et al., 2013), was used to generate deformation time series. TimeFun adapts the same inversion strategy as that used in MInTS, but it is implemented in the data domain (Hetland et al., 2016; Lu et al., 2005; Costantini, 1998; Berardino et al., 2002; Gong et al., 2016; Agram et

al., 2013, 2016). Since it uses a singular value decomposition (SVD) approach with a minimum-norm criterion, TimeFun is capable of inverting networks that are not fully connected (Agram et al., 2016). For every pixel with a coherence value above a user-specified threshold in all interferograms, TimeFun inverts small-baseline interferometric phases into time series measurements. This method is also applied to multi-looked interferograms to further reduce decorrelation noise.

2.3 Results

After careful inspection, 27 post-fire short baseline interferograms possessing relatively good coherence were selected to generate time series of deformations using the TimeFun method. The coherence, dependent on interferograms and ground futures, ranges from around 0.1–0.9. We used pixels with coherence values greater than 0.7 to avoid possible unwrapping errors. Permafrost process, especially post-fire surface dynamics, is complex in nature. Therefore, instead of using high order polynomials, we used spline function, i.e., piecewise polynomials, defined for example in (Ahlberg, 1967), to invert the interferogram network to the time series. As permafrost thaws from top to bottom, due to the change in the type of ground ice being thawed, i.e., pore-ice and/or excess-ice permafrost, temporarily variable deformation rate can be detected by InSAR over permafrost. Regarding this complexity of post-fire deformations over permafrost, spline function seems to be a proper pre-defined function to invert the interferograms to time series deformation. However, this may make time series plots look uneven. Figure 2.3 shows temporal and perpendicular baselines of the interferograms. Since only one interferogram connects two clusters of the images, i.e., interferogram 12 of track 252, the quality of the time series strongly depends on it. This indicates that all noise and artifacts present in the interferogram will be propagated in the time series analysis. Moreover, because of the

orbital drift of the ALOS satellite, the perpendicular baseline generally increases in time (Figure 2.3). Therefore, the topographic error that is proportional to the perpendicular baseline can possibly propagate in our temporal analysis. However, because our study area is flat near the Yukon River Basin, and our modeling scheme that will be presented later can cancel out the terms pertinent to the topographic errors, those errors can be assumed to be negligible. Figure 2.4 illustrates, from each of the tracks, two interferograms of the least connected images. The interferogram, i.e., interferogram 12 of track 252, as well as the other three interferograms illustrated in Figure 2.4, demonstrates expected subsidence over the fire scar. Figure 2.5 shows the post-fire deformation time series of path 252 where the deformations are temporarily relative to 6 September 2009, and spatially relative to a reference point (cyan star in Figure 2.1) that has been shown by field measurements (Clark and Duffy, 2006) to be permafrost-free soil. As seen on the images (Figure 2.5), the time series demonstrates larger subsidence over the burned areas (up to 20 cm) compared to the deformation over the off-scar surrounding area (<5 cm). Generally, InSAR-detected post-fire subsidence is expected to be larger over the burned areas compared to surrounding unburned areas due to permafrost degradation and/or increased ALT as a consequence of wildfire-induced organic layer removal and soil temperature warming.

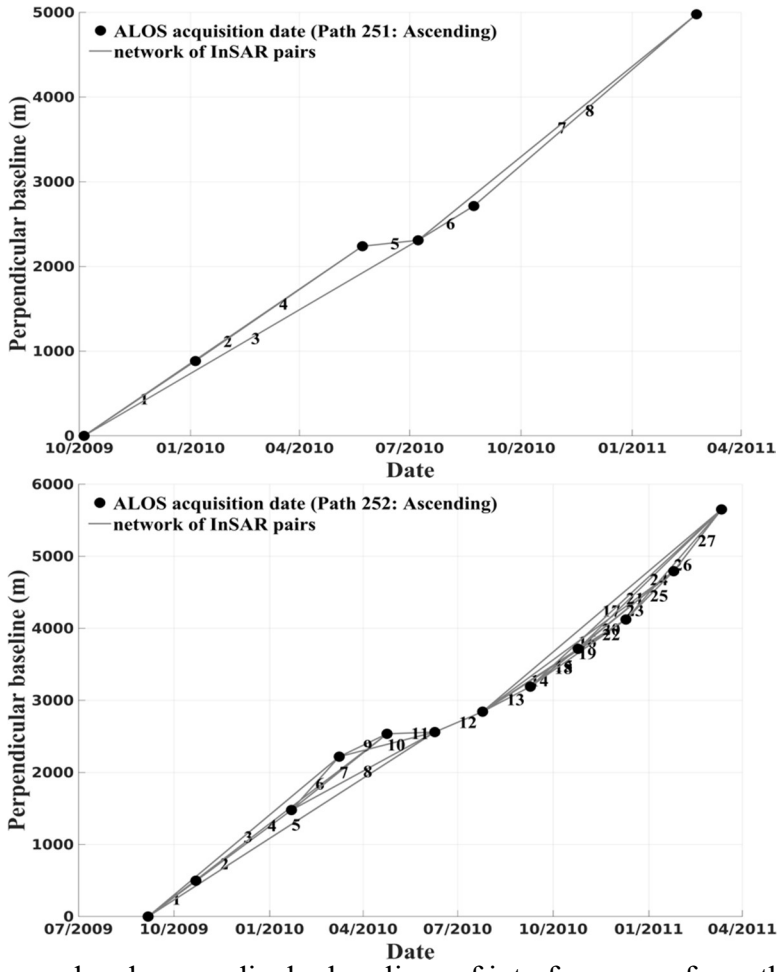

Figure 2.3. Temporal and perpendicular baselines of interferograms for paths 251 and 252.

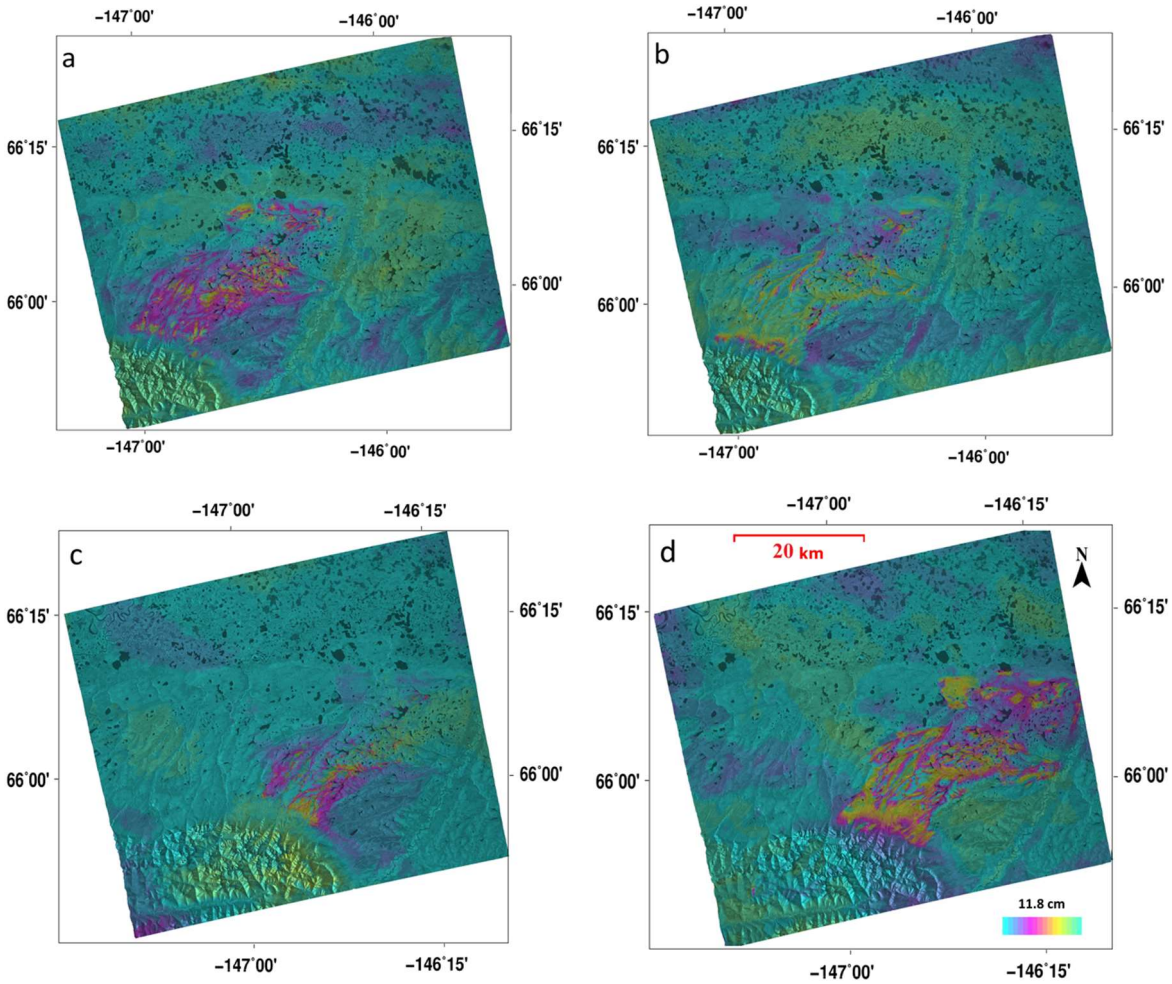

Figure 2.4. Unwrapped interferogram between images (**a**) 25 May 2010 and 8 July 2010 (track 251), (**b**) 8 July 2010 and 23 August 2010 (track 251), (c) 9 June 2010 and 25 July 2010 (track 252), and (d) 25 July 2010 and 9 September 2010 (track 252).

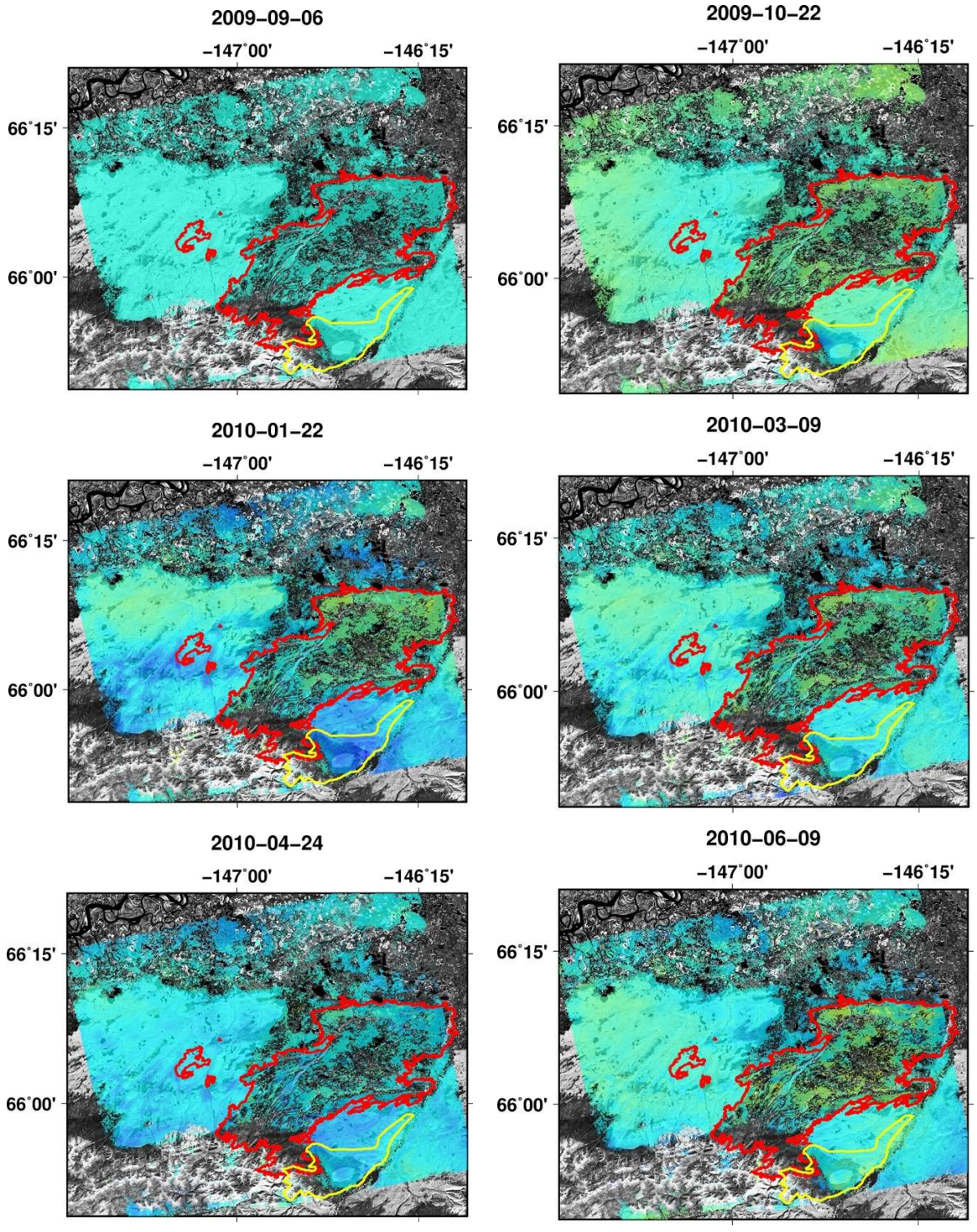
2009–09–06
2009–10–22
2010–01–22
2010–03–09
2010–04–24
2010–06–09
–147°00'
–146°15'
66°15'
66°00'

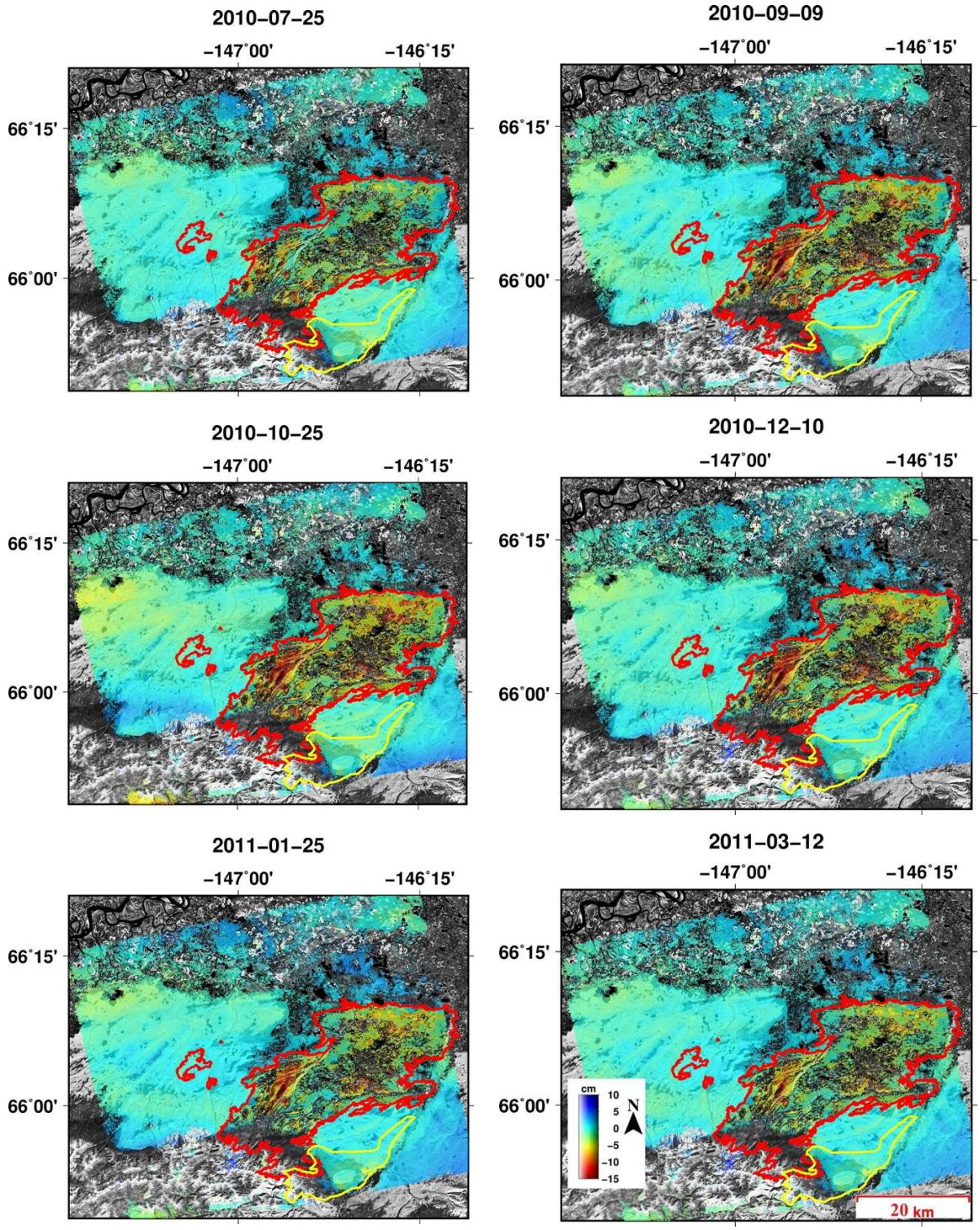

Figure 2.5. Accumulated deformation time series from path 252. Warm colors (red) represent ground subsidence occurring in fire-burned areas.

2.4 Discussions

Ground ice takes up about 9% more volume than groundwater in the unfrozen state. Therefore, subsidence in summer and uplift in winter occur when the active layer thaws and freezes. This repetitive pattern of ground subsidence and uplift, which can be recognized as the seasonal variations of the ground surface, is typical in most permafrost regardless of human/natural perturbations (i.e., deforestation, wildfire). Ground surface deformation over permafrost, detected by InSAR, can be closely related to the volume changes of thawing/freezing ground ice in active layer (Liu et al., 2012). Generally, using InSAR-detected ground surface deformations, one can estimate ALT and change in ALT if the soil characteristics (porosity, saturation) in active layer are well defined.

The winter freeze and summer thaw are completely natural in a permafrost region. However, the extreme fire events in the shrub and forest-covered Alaskan region can degrade both the active layer and underlying permafrost significantly. Wildfire can be triggered by natural processes and human perturbation, but regardless of the cause of wildfires, the drastic changes on the ground surface and underground soil formations induced by high heat can lead to irreversible consequences, such as thawing of permafrost and alteration of the soil characteristics in the active layer. Because of its low coherence, InSAR cannot measure the ground deformation through the comparison of pre- and post-wildfire SAR acquisitions. However, InSAR during post-wildfire can maintain the appropriate coherence, and we still can estimate the ground surface deformation that is closely related to the permafrost degradation and changes in active layer. We cannot disregard the seasonal variation of the movements of ground surface. Hence, we distinguished two major effects (seasonal and degradation effects) in our time-series observation.

2.4.1 Modeling

To model the observed deformation of the study area, we considered a two-layer system of an active layer and an underlying permafrost. The hypothesis is that due to a thinned insulating organic layer and decreased surface albedo, downward heat transfer during post-fire thaw season (summer) increases, leading to increased thaw depth of active layer. Due to the increased thaw depth, based on the type of ground ice in permafrost, different deformation patterns may develop. If the ground ice in permafrost occurs in the form of pore ice, increased thaw depth leads to greater seasonal deformations, i.e., subsidence in summer and uplift in winter, without causing depression of the ground surface. Note that pore ice is the ice fills in the pores of soil and does not include segregated ice. Pore ice, when melting, does not generate water in excess of the pore volume of the soil in unfrozen condition (Harris et al., 1988). On the other hand, permafrost contains excess ice, and ground ice melting due to increased thaw depth generates meltwater in excess of the pore volume of the unfrozen soil. Excess ice is the volume of ice in permafrost that exceeds the total pore volume of the unfrozen soil (Harris et al., 1988). Therefore, due to excess ice melting, long-term ground surface depression, which can be categorized as a consequence of permafrost degradation, happens with no increase in seasonal deformations and measured ALT. Note that ALT is usually measured from the soil surface down and not relative to the original soil surface for the post-fire deformation measurements (e.g. Pastick). In this way, an observer on the ground may not notice the net subsidence of the surface, i.e., ground surface depression, due to thawing of ice-rich permafrost or thawing of transition layer between permafrost and active layer. Therefore, ALT measurements alone cannot show thawing of ice-rich permafrost (Shiklomanov et al., 2013). Our model, however, estimates the increase in ALT (Figure 2.6b) owing to thaw penetration into the pore ice permafrost as well as

the net ground surface depression (Figure 2.6a) due to thawing of excess ice (ice-rich) permafrost.

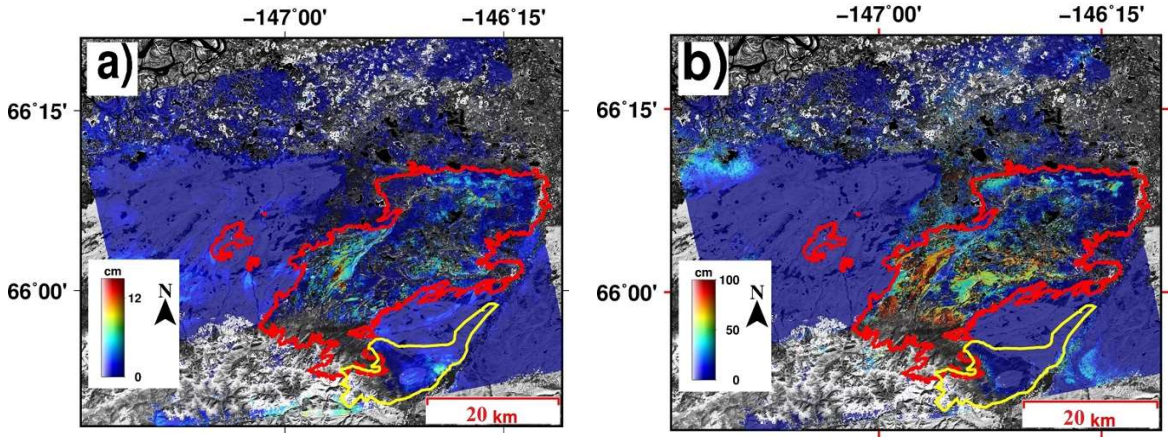

Figure 2.6. Total thickness of (**a**) thawed excess ice and (**b**) pore ice permafrost during the second post-fire thaw season.

Imagine pre-fire seasonal deformation and ALT to be δ_{pre} and ALT_{pre}, respectively. In the first post-fire summer, due to a thinned organic layer, increased downward heat transfer thaws excess ice and/or pore ice permafrost with the thicknesses of T_1^i and T_1^p, respectively. The thickness of thawed ice-rich permafrost, i.e., T_1^i, contributes totally to the subsidence, whereas the contribution of the thawed pore ice permafrost to subsidence depends on the thawed permafrost's thickness, soil porosity, and saturation, as well as the densities of ice and water. By taking permafrost's soil porosity to be constant, its saturation to be 1.0, and the densities of ice and water to be constant, and subsidence depends only on the thickness of thawed pore ice permafrost and increases by increasing the thickness. In the following equations, we try to formulate the relationship between thawed permafrost thickness and InSAR-measured deformations. In the following equations, δ' (primed δ) represents uplift, whereas δ denotes

subsidence. The subscripts 1 and 2 denote first and second year, respectively. Also, superscripts *p* and *i* denote pore ice and excess ice permafrost, respectively. Therefore, we have

$$\delta_1 = \delta_{pre} + \emptyset \frac{\rho_w - \rho_i}{\rho_w} T_1^p + T_1^i \quad (2.1)$$

where δ_1 is the subsidence during the post-fire first year thawing season, Ø is the porosity of pore ice permafrost's soil, ρ_w is the density of water (1.0 g/cm^3), ρ_i is the density of ice (0.917 g/cm^3), T_1^p is the total thicknesses (cm) of thawed pore ice permafrost, and T_1^i is the total thickness (cm) of the thawed excess ice permafrost during the post-fire first thawing season. By the end of first thawing season, the ALT, i.e., ALT_1, increases by T_1^p and becomes $ALT_{pre} + T_1^p$. The meltwater of the thawed excess ice drains away and during the following winter, the new active layer freezes and heaves by

$$\delta_1' = \delta_{pre} + \emptyset \frac{\rho_w - \rho_i}{\rho_w} T_1^p \quad (2.2)$$

where δ_1' is the post-fire uplift at the end of the first winter, calculated by subtracting the accumulated deformation on 22 October 2009 from the accumulated deformation on 24 April 2010. In a similar way, the post-fire second-year subsidence at the end of the thawing season and uplift at the end of the freezing season can be expressed as

$$\delta_2 = \delta_1 + \emptyset \frac{\rho_w - \rho_i}{\rho_w} T_1^p + T_2^i \quad (2.3)$$

$$\delta_2' = \delta_1' + \emptyset \frac{\rho_w - \rho_i}{\rho_w} T_2^p \quad (2.4)$$

where δ_2 is the subsidence at the end of the second thawing season, calculated by subtracting the accumulated deformation on 25 October 2010 from the accumulated deformation on 24 April 2010, δ_2' is the uplift at the end of the second freezing season, calculated by subtracting the accumulated deformation on 25 October 2010 from the accumulated deformation on 12 March 2011, T_2^p is the total thicknesses of thawed pore ice permafrost, and T_2^i is the total thickness of the thawed excess ice permafrost during the second post-fire thawing season. Based on the air temperature measurements in 2009 at Circumpolar Active Layer Monitoring Network (CALM) sites in or study area, i.e., Fort Yukon and Circle sites (https://www2.gwu.edu/~calm/), the air temperature dropped to near zero values at late September and early October. However, there is no soil temperature measured at these sites. The air and soil temperature measurements at the SNOTEL site, Eagle Summit (960) (Natural Water and Climate Center (https://wcc.sc.egov.usda.gov)), which is about 60 km away from the study area, show more than one month phase delay between the air and soil temperatures. Air temperature dropped to below zero values at mid-September and soil temperature remains above zero until mid-December. In our study area, at Circle and Fort Yukon sites, the air temperature became negative at the end of September (or early December). So, considering few weeks phase delay between air and soil temperatures, we estimate soil freezing in our study area to occur no earlier than mid- or late-October.

InSAR estimates δ_1', δ_2, and δ_2'. Therefore, the total thickness of the thawed excess ice permafrost during the second post-fire thaw season can be calculated by subtracting equation

(2.4) from equation (2.3). Likewise, the total thicknesses of thawed pore ice permafrost during the second year can be calculated by rewriting equation (2.4)

$$T_2^p = \frac{\delta_2' - \delta_1'}{\emptyset} \frac{\rho_w}{\rho_w - \rho_i} \tag{2.5}$$

$$T_2^i = \delta_2 - \delta_2' \tag{2.6}$$

Our study area, located in the Yukon Flats, is underlain by more than 88 m of quiet-water silt and silty sand, overlain by alluvial deposits (Williams, 1962). An extensive mantle of eolian silt covers the marginal upland bordering the Yukon Flats (Black, 1951). The loess, which covers the study area, is massive well-sorted homogeneous unconsolidated tan to gray silt and sandy silt (Williams, 1962). Therefore, we set Ø to be 0.46 (the porosity of silt) and solved equations (2.5) and (2.6). Figure 2.6 illustrates the total thickness of thawed excess ice and pore ice permafrost during the second post-fire thaw season. Figure 2.6a illustrates up to 15 cm depression due to excess ice permafrost degradation. Also, Figure 2.6b shows up to 80 cm increase in ALT during the second post-fire year.

Here, the assumption is that the post-fire soil of thawed pore-ice permafrost is fully saturated. However, this assumption may not be correct in cases where, for example, permafrost disappears entirely and becomes permeable for meltwater. Also, the equations assume that the change in the InSAR-detected organic layer deformation between the two post-fire following years, due to vegetation regrowth and soil moisture, is negligible. The change in the volume of the seasonally segregated ice between the first and second post-fire freezing seasons is assumed

to be negligible. However, this assumption may not be true. Yet the main limitation of the model is related to data availability. Estimating seasonal deformations over a thawing/freezing season requires a connected network of interferograms, spanning over the entire thawing/freezing season and covering soil thaw and freeze onset dates. Sometimes, long repeat-pass periods and loss of coherence and/or other artifacts like ionospheric effect reduce the number of available interferograms. In some cases, the available network of interferograms partly covers the full season. In this case, to estimate full-season deformation using a truncated interferogram network, the modified version of the Stefan equation (explained e.g., in (Liu et al., 2010, 2012)) can be used to approximate the depths of thaw and freeze as a function of time and temperature.

Generally, for time series purposes, InSAR measurements are always considered to be relative to a reference point, which is assumed to have no or a predefined deformation time series. However, selecting a reference point can be controversial, and if not properly selected, a non-stable reference point will lead to biased measurements. Not that the bias initiated by using a reference point with seasonal deformations can be completely cancelled out by our model if the reference point has equal frost heave and thaw settlement in winter and summer, respectively. However, in the case of non-equal seasonal deformations of the reference point, i.e., non-equal summer subsidence and winter uplift, the model cannot fully prevent biased measurements.

2.4.2 Validation of InSAR Results and Estimation of Uncertainties

We selected interferograms with no ionospheric effects and the interferograms were flattened, atmospheric correction was applied to remove stratified tropospheric artifacts, and topography phase components have been removed using TanDEM-X DEM. Despite that, the measured InSAR phase may still have contributions from troposphere, topography, ionosphere, DEM errors, etc. Note that the estimated error in $\delta_2' - \delta_1'$ and $\delta_2 - \delta_2'$, due to orbit drift are 0.04

and 0.27 cm. Also, the accuracy of phase unwrapping influences directly the accuracy of InSAR estimations. This is the case especially over low coherence pixels. So we carefully selected high coherence interferograms to avoid unwrapping error.

Here, we present the mean annual deformation velocity to visually inspect the deformations and compare the deformations over fire scar with the deformations over off-scar surrounding areas. Figure 2.7 presents the mean annual velocity map. Off-scar areas have less than 2-cm deformations, which is most likely induced by ground surface processes over permafrost. Also, the study area is almost flat and DEM-induced error is expected to be negligible.

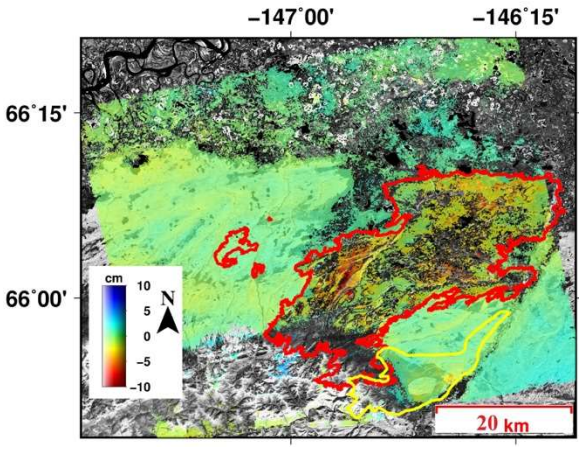

Figure 2.7. Mean annual deformation velocity map of track 252.

To further evaluate the InSAR results, we generated deformation time series using eight post-fire SAR images from path 251, which overlaps path 252 and covers the fire scar. Then, the results of the two independent time series from path 251 and 252 were compared by selecting eight points over the burned area (Figure 2.1). Figure 2.8 shows the plots of deformation time series over the two paths. The comparison showed good agreement between the results.

Although points 2 and 3 (P251-2, P251-3, P252-2, and P252-3 in Figure 2.8) are on the burned area, they have smaller subsidence than other points on the burned area. This may indicate that underground permafrost was either absent or totally destroyed during the first post-fire thawing season, or that the post-fire organic layer was thick enough to keep the permafrost cool. This conclusion can be applied to all other points inside the burned area with small subsidence.

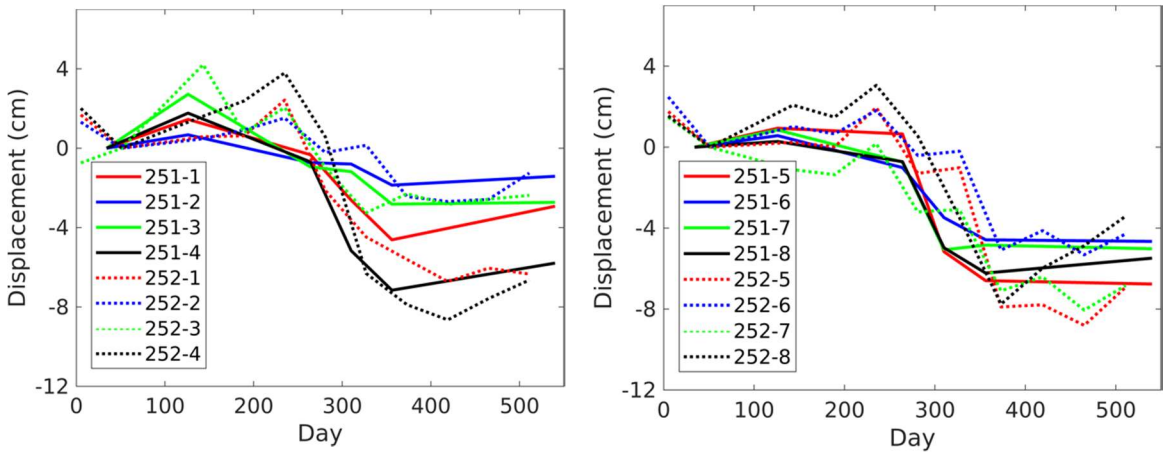

Figure 2.8. Plot of deformation for the eight selected points. Each pair of the same-color solid and dotted lines represent graphs of one selected point over path 251 and 252, respectively. The x-coordinate shows days passed since 1 September 2009.

A careful inspection of the deformation time series demonstrated in Figure 2.5 and the model's results shown in Figure 2.6 reveals that the density of low coherence pixels, i.e., colorless pixels on the images, is higher over the central and eastern part of the fire scar. Not surprisingly, the area is dominated by lakes/ponds (Figure 2.1). This may infer that the area is more dynamic compared to the rest of the study area and experiences surface processes that lead to the loss of coherence, which makes InSAR measurements infeasible. The rest of the area, however, possesses relatively higher coherence values. Over the higher coherence area (away from the lake/pond area), our model estimates up to a 15-cm ground level decline and up to an 80-cm increase in ALT.

Although there is no extensive ground truth data taken from the study area, we generally compared our model's results and limited field measurements in the study area taken from 2010 to 2012 (Nossov eta al., 2013). Thaw depths have been measured from 2010 to 2012 along two 100–200-m transects with different fire disturbance histories. Figure 2.1 shows the location of the sampling site, which is unfortunately located in the low coherence area. The measurements showed that the wildfire-increased ALT with most settlements happened during the first and second year after fire, and the permafrost table was largely stabilized in the third year after fire (Nossov eta al., 2013). From 2010 to 2012, ALT increased by an average of 41 cm, with a maximum of 75 cm, and ground surface elevations declined on average by 9 cm, with a maximum of 39 cm, due to the degradation of ice-rich permafrost (Nossov eta al., 2013). However, since the sampling site falls in the low coherence area, which makes InSAR measurements infeasible, we could only compare the results generally.

In general, the InSAR-estimated ground surface depression over the area away from lakes/ponds is smaller than the ground surface elevation decline measured in the lake/pond dominated area. This may indicate to us that the lake/pond dominated area is underlain by thicker excess ice permafrost. Also, our model shows up to an 80- and 40-cm increase in ALT over the southern and northern parts of the fire scare, respectively, during the first year after the fire. The estimated increase in ALT over the northern part of the study area is in good agreement with the result of ground measurements, i.e., a maximum of a 75-cm increase in ALT from 2010 to 2012 (Nossov eta al., 2013). Since the thawing of excess ice permafrost did not add to ALT whereas pore ice permafrost thawing increased ALT, we can infer that the ground ice underlying the area away from the lakes/ponds, especially the southern part of the study region, is dominated by pore ice permafrost. The large increases over the southern part, i.e., up to 80 cm, indicate the likely

formation of talik. However, no sample has been taken from the southern part of the fire scar to allow us to evaluate the results.

Model uncertainty can be estimated by calculating the uncertainty of each parameter involved in modeling and the sensitivity of the model to changes in the parameter, i.e., the adjoint relative to the parameter. By assuming that the parameters are affecting the model independently, the uncertainty of the model was then calculated by (e.g. Liu et al., 2010)

$$\sigma_{model} = \left(\sum_{k=1}^{n} \left(\frac{\partial M}{\partial P_k} \sigma_k \right)^2 \right)^{1/2} \tag{2.7}$$

where σ_{model} is the uncertainty of the model, P_k denotes parameters, n is the number of parameters, $\frac{\partial M}{\partial P_k}$ is the sensitivity of the model to the changes in parameter P_k, and σ_k represents uncertainty of P_k. Table 2.1 represents the parameters involved in estimating the change in the ALT, their values, uncertainties, relative contribution to the total uncertainty of the model, and cumulative uncertainties.

Equation (2.3) represents the parameters involved in estimating the changes in the ALT, i.e., T_2^p. The value for $\delta_2' - \delta_1'$ was calculated by averaging the difference between the post-fire first and second year seasonal uplifts over the fire-affected area. The uncertainty in the parameter is the standard deviation of the difference between the post-fire first and second year seasonal uplifts over the off-scar areas. Parameter S denotes the saturation of the soil that has been added to the active layer in the second thawing season due to thawed pore ice permafrost. We assumed the soil to be fully saturated, $S = 1.0$. Taking porosity to be a constant value is a source of

uncertainty as it is a site-specific characteristic of soil and should ideally be determined from in situ measurements at all InSAR pixels, thus we choose 0.1 of uncertainty in *S*. However, based on (Williams, 1962; Black, 1951), we estimated the porosity, P, to be in a narrow range around 0.46, i.e., 0.46 ± 0.10. The uncertainty in T_2^i, thawed excess ice permafrost, equals the uncertainty of the parameter $\delta_2 - \delta_2'$. The uncertainty in the parameter is the standard deviation of the difference between the post-fire second year seasonal subsidence and uplift over the off-scar areas, i.e., 1.50 cm. Calculating standard deviation over the unburned area means that we have taken into account the uncertainties due to other sources of noise and artifacts such as long-term deformation trend, atmospheric artifacts, orbit drift, and residual orbital errors.

Parameter	Value	Parameter Uncertainty	Cumulative Uncertainty (cm)	Relative Contribution (%)
$\boldsymbol{\delta_{post-up,2} - \delta_{post-up,1}}$	**2.58 (cm)**	**0.97 (cm)**	**23.43**	**84.36**
Porosity	**0.46**	**±0.10**	**27.06**	**13.09**
Saturation	**1.0**	**0.1**	**27.77**	**2.55**

Table 2.1. Model's parameters, the uncertainties of each parameter, cumulative uncertainty, and relative contribution in the model for estimating changes in the ALT.

2.5 Conclusions

InSAR analyses using L-band ALOS PALSAR images have successfully mapped fire-induced permafrost deformations in interior Alaskan boreal forest where loss of coherence is a major obstacle for applying InSAR. The loss of coherence caused by wildfire was prominent

within the burned area for interferograms pairing both pre- and post-fire SAR images. Although the loss of coherence restricted the total number of viable coherence pairs, by selecting only post-fire interferograms, we were able to establish interferogram networks covering three post-fire freezing and thawing seasons (2009–2010 and 2010–2011 freezing seasons, and 2010 thawing season) and generate post-fire deformation time series.

Our analyses showed that the 2009 fire caused up to 20 cm of subsidence in the thawing season of 2010. The fire increased active layer thickness, which manifested as greater uplift over burned areas compared to unburned areas. Although the permafrost process is complex, we used a simple model that uses deformation time series to estimate fire-induced change in ALT as well as the thickness of thawed excess ice permafrost. The model assumes that deformation happens because ground water takes up to 9% less volume than ground ice.

Our model revealed up to 15 cm of wildfire-induced excess ice permafrost thawing and up to an 80-cm increase in ALT. It can be seen on the map (Figures 2.5 and 2.6) that except for some local patches, almost the entire burned area features ground surface subsidence due to ALT change. This indicates that almost the entire area is underlain by pore ice permafrost. The thawing of excess ice permafrost does not add to ALT, whereas pore ice permafrost thawing increases ALT and its seasonal deformations. It should be noted that ALT is usually measured from the soil surface down and not relative to the original soil surface (e.g. Pastick et al., 2015). Therefore, we can infer that the area is dominated by pore ice permafrost. Some areas underlain by both pore and excess ice permafrost, however, experienced permafrost degradation in addition to ALT change.

A comparison between the results of path 252 and a neighboring track covering the burned area, i.e., path 251, showed a good agreement between the results of the two paths. We

also estimated the uncertainty of the model by calculating the uncertainty of all parameters involved in the model. The uncertainties in the estimated change in the ALT and the thickness of the thawed excess-ice permafrost are 27.77 cm and 1.50 cm, respectively.

The introduced model can be used in other places to estimate fire-induced permafrost degradation and ALT change. However, as discussed earlier in the paper, uncertainties are involved in the model and affect the accuracy of estimated thicknesses. Therefore, pre-and post-fire extensive field sampling in an area, if available, can calibrate the model and improve the results.

Acknowledgments: The ALOS PALSAR data was downloaded from the Alaska Satellite Facility (https://www.asf.alaska.edu/). The high resolution DEM data of the study area, TanDEM-X, were provided by the German Aerospace Center (DLR). This research was financially supported by NASA Earth and Surface Interior Program (NNX16AK56G), U.S. Geological Survey (G14AC00153), and the Shuler-Foscue Endowment at Southern Methodist University. Comments and edits by the academic editor, six anonymous reviewers and Thomas Adamson significantly improved the manuscript.

References

Zhang, Z.Q., and Q.B. Wu. 2012. Predicting changes of active layer thickness on the Qinghai-Tibet Plateau as climate warming. *J. Glaciol. Geocryol.*, *34*, 505–511. (In Chinese)

Zhang, T., R.G. Barry, K. Knowles, J.A. Heginbottom, J. Brown. 1999. Statistics and characteristics of permafrost and ground ice distribution in the Northern Hemisphere. *Pol. Geogr.*, 147.169.

Apps, M.J., W.A. Kurz, R.J. Luxmoore, L.O. Nilsson, R.A. Sedjo, R. Schmidt, L.G. Simpson, and T.S. Vinson. 1993. Boreal forests and tundra. *Water Air Soil Pollut.*, *70*, 39–53.

Strauss, J., L. Schirrmeister, S. Wetterich, A. Borchers, and S.P. Davydov. 2012. Grain-size properties and organic-carbon stock of yedoma ice complex permafrost from the Kolyma lowland, northeastern Siberia. Glob. *Biogeochem. Cycles*, 26, doi:10.1029/2011GB004104.

Harris, S.A., J.A. French, G.H. Heginbottom, B. Johnston, D.C. Ladanyi, and R.O.S. van Sego. 1998. Glossary of Permafrost and Related Ground-Ice Terms, Technical Memorandum No. 142, *National Research Council of Canada*: Ottawa, ON, USA.

Streletskiy, D.A., N.I. Shiklomanov, and F.E. Nelson. 2012. Spatial variability of permafrost active-layer thickness under contemporary and projected climate in northern Alaska. *Pol. Geogr*., 35, 95–116, doi:10.1080/1088937X.2012.680204.

Machay, J. 1977. Probing for the bottom of the active layer. *Can. Geol. Surv.* Pap., 77–1A, 327–328.

Hubbard, S.S., C. Gangodagamage, B. Dafflon, H. Wainwright, J. Peterson, A. Gusmeroli, C. Ulrich, Y. Wu, C. Wilson, J. Rowland, et al. 2013. Quantifying and relating land-surface and subsurface variability in permafrost environments using LiDAR and surface geophysical datasets. *Hydrogeol. J.*, 21, 149–69.

Liu, L., K. Schaefer, T. Zhang, and J. Wahr. 2012. Estimating 1992–2000 average active layer thickness on the Alaskan North Slope from remotely sensed surface subsidence. J. Geophys. Res., 117, doi:10.1029/2011JF002041.

Nelson, F.E., N.I. Shiklomanov, G.R. Mueller, K.M. Hinkel, D.A. Walker, J.G. Bockheim. 1997. Estimating active-layer thickness over a large region: Kuparuk River basin, Alaska, USA. *Arct. Alp. Res*., 29, 367–378, doi:10.2307/1551985.

Shiklomanov, N., and N. Nelson. 1999. Analytic representation of the active layer thickness field, Kuparuk River Basin, Alaska. Ecol. Model., 123, 105–125, doi:10.1016/S0304-3800(99)00127-1.

Panda, S.K., A. Prakash, D.N Solie, V.E. Romanovsky, and M.T. Jorgenson. 2010. Remote sensing and field-based mapping of permafrost distribution along the Alaska Highway corridor, interior Alaska. *Permafr. Periglac. Process*., 21, 271–281, doi:10.1002/ppp.686.

Gangodagamage, C., J.C. Rowland, S.S. Hubbard, S.P. Brumby, A.K. Liljedahl, H. Wainwright, C.J. Wilson, G.L. Altmann, B. Dafflon, J. Peterson, et al. 2014. Extrapolating active layer thickness measurements across Arctic polygonal terrain using LiDAR and NDVI data sets. *Water Resour. Res*., 50, 6339–6357, doi:10.1002/2013WR014283, 2014.

Schaefer, K., L. Liu, A. Parsekian, E. Jafarov, A. Chen, T. Zhang, A. Gusmeroli, S. Panda, H.A. Zebker, and T. Schaefer. 2015. Remotely sensed active layer thickness (ReSALT) at Barrow, Alaska using interferometric synthetic aperture radar. *Remote Sens.,* 7, 3735–3759.

Massonnet, D., and K. Feigl. 1998. Radar interferometry and its application to changes in the Earth's surface. *Rev. Geophys*., 36, 441–500.

Bürgmann, R., P.A. Rosen, and E.J. Fielding. 2000. Synthetic aperture radar interferometry to measure Earth's surface topography and its deformation. Annu. Rev. *Earth Planet. Sci.,* 28, 169–209.

Simons, M., and P. Rosen. 2007. Interferometric Synthetic Aperture Radar Geodesy. *Treatise Geophys. Geodesy*, 3, 391–446.

Lu, Z., and D. Dzurisin. 2014. InSAR Imaging of Aleutian Volcanoes: Monitoring a Volcanic arc from Space, Geophysical Sciences, Springer Praxis Books, Springer: Chichester, UK, 2014, p. 390.

Kim, J., Z. Lu, L. Gutenberg, Z. Zhu. 2017. Characterizing hydrologic changes of the Great Dismal Swamp using SAR/InSAR. *Remote Sens. Environ*., 198, 187–202.

Rykhus, R., and Z. Lu. 2008. InSAR detects possible thaw settlement in the Alaskan Arctic Coastal Plain. Can. J. Remote Sens., 34, 100–112.

Liu, L., T. Zhang, and J. Wahr. 2010. InSAR measurements of surface deformation over permafrost on the North Slope of Alaska. J. Geophys. Res., 115, F03023, doi:10.1029/2009JF001547.

Short, N., B. Brisco, N. Couture, W. Pollard, K. Murnaghan, and P. Budkewitsch. 2011. A comparison of TerraSAR579 RADARSAT-2 and ALOS-PALSAR interferometry for monitoring permafrost environments, case study from Herschel Island, Canada. *Remote Sens. Environ*., 115, 3491–3506.

Liu, L., K. Schaefer, A. Gusmeroli, G. Grosse, B.M. Jones, T. Zhang, A.D. Parsekian, and H.A. Zebker. 2014a. Seasonal thaw settlement at drained thermokarst lake basins, Arctic Alaska. *Cryosphere*, 8, 815–826.

Liu, L., K.M. Schaefer, A.C. Chen, A. Gusmeroli, H.A. Zebker, and T. Zhang. 2015. Remote sensing measurements of thermokarst subsidence using InSAR. *J. Geophys. Res. Earth Surf.*, 120, 1935–1948.

Liu, L., E.E. Jafarov, K.M. Schaefer, B.M. Jones, H.A. Zebker, C.A. Williams, J. Rogan, T. Zhang. 2014b. InSAR detects increase in surface subsidence caused by an arctic tundra fire. *Geophys. Res. Lett*., 41, 3906–3913.

Iwahana, G., M. Uchida, L. Liu, W. Gong, F.J. Meyer, R. Guritz, T. Yamanokuchi, and L. Hinzman. 2016. InSAR Detection and Field Evidence for Thermokarst after a Tundra Wildfire, Using ALOS-PALSAR. *Remote Sens*., 8, 218, doi: 10.3390/rs8030218.

Jones, B.M., G. Grosse, C.D. Arp, E. Miller, L. Liu, D.J. Hayes, C.F. Larsen. 2015. Recent Arctic tundra fire initiates widespread thermokarst development. *Sci. Rep.,* 5, 693, doi:10.1038/srep15865.

Lutes, D.C., R.E. Keane, J.F. Caratti, C.H. Key, N.C. Benson, S. Sutherland, and L.J. Gangi. 2006. FIREMON: Fire effects monitoring and inventory system. Gen. Tech. Rep. RMRS-GTR-164. Fort Collins, CO: U.S. Department of Agriculture, Forest Service, Rocky Mountain Research Station. 1 CD.

Parks, S.A., G.K. Dillon, and C.A. Miller. 2014. New metric for quantifying burn severity: The relativized burn ratio, *Remote Sens.*, 1827–1844.

Jorgenson, M.T., K. Yoshikawa, M. Kanveskiy, Y. Shur, V. Romanovsky, S. Marchenko, G. Grosse, J. Brown, and B. Jones. 2008. Permafrost characteristics of Alaska. In Proceedings of the Ninth International Conference on Permafrost Extended Abstracts, Potsdam, Germany, 20–24 June 2016, Kane, D.L., Hinkel, K.M., Eds., Univ. of Alaska: Fairbanks, AK, USA, 2008, pp. 121–122.

Spetzman, L.A. 1963. Terrain Study of Alaska, Part 5. Vegetation (Map), Engineer Intelligence Study, U.S. Army, Office of Chief Engineers: Washington, DC, USA.

Pastick, N.J., M.T. Jorgenson, B.K. Wylie, S.J. Nield, K.D. Johnson, and A.O. Finley. 2015. Distribution of near-surface permafrost in Alaska: Estimates of present and future conditions. *Remote Sens. Environ.*, 168, 301–315.

Viereck, L.A., C.T. Dyrness, A.R. Batten, and K.J. Wenzlick. 1992. The Alaska Vegetation Classification, General Technical Report PNW-GTR-286, Department of Agriculture, Forest Service, Pacific Northwest Research Station: Portland, OR, USA, p. 278.

Johnstone, J.F., F.S. Chapin, T.N. Hollingsworth, M.C. Mack, V. Romanovsky, and M. Turetsky. 2010. Fire, climate change, and forest resilience in interior Alaska. *Can. J. For. Res.,* 40, 1302–1312.

Gallant, A.L., E.F. Binnian, J.M. Omernik, and M.B. Shasby. 1995. Ecoregions of Alaska US Geological Survey Professional Paper, US Department of Interior: Washington, DC, USA, p. 1567.

Hetland, E.A., P. Muse, M. Simons, Y.N. Lin, P.S. Agram, and C.J. Di Caprio. 2012. Multiscale InSAR Time Series (MInTS) analysis of surface deformation. *J. Geophys. Res. Solid Earth*, 117, doi:10.1029/2011JB008731.

Lu, Z., C. Wicks, J.O. Kwoun, J.A. Power, and D. Dzurisin. 2005. Surface deformation associated with the March 1996 earthquake swarm at Akutan Island, Alaska, revealed by C-band ERS and L-band JERS radar interferometry. Can. J. *Remote Sens.,* 31, 7–20.

Costantini, M. 1998. A novel phase unwrapping method based on network programming. *IEEE Trans. Geosci. Remote Sens.*, 36, 813–821.

Berardino, P., G. Fornaro, R. Lanari, and E. Sansosti. 2002. A new algorithm for surface deformation monitoring based on small baseline differential SAR interferograms. IEEE Transactions on Geoscience and Remote Sensing,40, 2375–2383.

Gong, W., A. Thiele, S. Hinz, F.J. Meyer, A. Hooper, and P.S. Agram. 2016. Comparison of Small Baseline Interferometric SAR Processors for Estimating Ground Deformation. *Remote Sens.,* 8, 330, doi:10.3390/rs8040330.

Agram, P.S., R. Jolivet, B. Riel, Y.N. Lin, M. Simons, E. Hetland, M.P. Doin, and C. Lasserrre. 2013. New Radar Interferometric Time Series Analysis Toolbox Released. *Eos Trans. Am. Geophys. Union*, 94, 69–70.

Agram, P.S., R. Jolivet, and M. Simons. 2016. Generic InSAR Analysis Toolbox (GIAnT), User Guide, 2016. Available online: http://earthdef.caltech.edu (accessed on Feb 26, 2017).

Ahlberg, J.H., E.N. Nielson, and J.L. Walsh. 1967. The Theory of Splines and Their Applications, Academic Press: New York, NY, USA, ISBN 0-12-044750-9.

Clark, M.H., and M.S. Duffy. 2006. Soil Survey of Denali National Park Area, Alaska, Palmer, A.K., Ed., Natural Resource Conservation Service: Washington, DC, USA, p. 822.

Harris, S.A., H.M. French, J.A. Heginbottom, G.H. Johnston, B. Ladanyi, D.C. Sego, and R.O. van Everdingen. 1988. Glossary of Permafrost and Related Ground-Ice Terms, Glossary of Permafrost and Related Ground-Ice Terms, Permafrost Subcommittee, Associate Committee on Geotechnical Research, National Research Council of Canada: Ottawa, ON, USA.

Shiklomanov, N.I., D.A. Streletskiy, J.D. Little, and F.E. Nelson. 2013. Isotropic thaw subsidence in undisturbed permafrost landscapes, *Geophys. Res. Lett.,* 40, 6356–6361, doi:10.1002/2013GL058295.

Williams, J.R. 1962. Geologic Reconnaissance of the Yukon Flats District Alaska, US Geological Survey Bulletin 1111-H. United States Government Printing Office, Washington, pp. 289–331.

Black, R.F. 1951. Eolian deposits of Alaska. *Arctic*, 4, 89–111.

Nossov, D.R., M.T. Jorgenson, K. Kielland, and M.Z. Kanevskiy. 2013. Edaphic and microclimatic controls over permafrost response to fire in interior Alaska. *Environ. Res. Lett*., 8, doi:10.1088/1748-9326/8/3/035013.

CHAPTER 3

MODELING INSAR TEMPORAL COHERENCE USING SAR AMPLITUDE: A CASE STUDY OF INTERIOR ALASKA

Molan, Y.E., J-W. Kim, Z. Lu, and P. Agram. 2018. L-band temporal coherence assessment and modeling using amplitude and snow depth over interior Alaska, *Remote Sensing*, 10(1):150.

3.1 Introduction

Interferometric synthetic aperture radar (InSAR) provides an all-weather, day-or-night capability to remotely sense mm to cm scale surface deformation with a high spatial resolution of tens of meters or better (e.g. Massonnet et al., 1998; Bürgmann et al., 2000; Simons and Rosen, 2007; Lu and Dzurisin, 2014). InSAR has been successfully used to detect surface deformation due to various mechanisms, such as volcanism, subsidence, permafrost, and landslides (Ferretti, et al., 2001; Kim et al., 2016; Hu et al., 2016; Rykhus and Lu, 2008; Liu et al., 2010). So far numerous methods and approaches have been developed to improve InSAR performance. However, temporal decorrelation, regardless of the processing methodology, is one of the major obstacles for all InSAR applications especially over vegetated areas. The main sources of the loss of coherence, i.e. decorrelation, are temporal decorrelation, spatial decorrelation, volume decorrelation, thermal decorrelation, and processing errors (e.g. Zebker and Villasenor, 1992; Just and Bamler, 1994). Generally, InSAR coherence decreases by increasing spatial and temporal baselines between two images.

InSAR coherence is sensitive to the changes in surface backscattering, which is dominated by surface dielectric constant and roughness on the scale of the radar wavelength (Simard et al., 2012; Rocca, 2007; Luo et al., 2001). It has been documented that temporal coherence can be influenced by temporal variations of surface backscattering due to changes in soil moisture, snow depth, surface roughness, and vegetation biomass (Simard et al., 2012; Rocca, 2007; Luo et al., 2001; Zwieback et al., 2015a, 2015b, 2015c; Lavalle et al., 2012; Zhang et al., 2003; Zhang et al., 2008; Borgeaud and Wegmueller, 1996; Morishita and Hanssen, 2015). Simard et al., 2012, found precipitation events to be the main cause of temporal decorrelation using fully polarimetric airborne L-band acquisitions over forested landscapes with up to 9 days temporal baselines,. Also, they argued that correlation decreases by increasing canopy height regardless of forest type and polarization. Zwieback et al., 2015b, evaluated soil moisture effects on L-band InSAR and revealed that the phase difference between two SAR images increased with increasing soil moisture difference, whereas the coherence decreased at the same time. Zhang et al., 2008, in a case study using C-band ERS SAR data, assessed the relationship between InSAR coherence and soil moisture and inferred that the relation between the two may satisfy an exponential distribution.

Although the effect of the changes in surface backscattering on InSAR coherence has been documented (e.g. Simard et al., 2012; Zwieback et al., 2015a; Lavalle et al., 2012), it has been largely neglected in the coherence models introduced so far. Temporal coherence in general is modeled as a univariate exponential function of temporal baseline (Zebker and Villasenor, 1992) with the assumption that the change in the position of scatterers, i.e. mutual displacements of scatterers, is the source of decorrelation (Lee et al., 2013). However, we argue that other variables, in addition to temporal baseline, should be added to the coherence function to

compensate the effect of temporal variation of surface backscattering on InSAR coherence. In this paper using ALOS-2 PALSAR-2 images, we analyzed temporal decorrelation of forested and shrub landscapes in Delta Junction, Alaska, and introduced a new InSAR coherence model, which takes into account the effects of the temporal variations of surface backscattering on InSAR coherence. The model considers the changes in the geometry and dielectric constant of scatterers to be the main sources of decorrelations. The effect of the gradual and natural change in scatterers' geometry has been modeled as a decaying exponential function, which is equivalent to the exponential function of temporal coherence found in the literature (Zebker and Villasenor, 1992; Rocca, 2007). The effect of the change in the surface backscattering, mainly due to the change in dielectric constant of scatterers on InSAR coherence has been modeled by utilizing the change in InSAR intensity as a proxy for it. The model also takes into account the decorrelation due to the change in snow depth between two images, which induces reversible and seasonal decorrelations. The model, in general and with difference constants, is applicable to model L-band InSAR coherence in other environments and may not be expanded to X-band or C-band SAR observations.

The importance of temporal decorrelations models and their practical use can be better understood by considering the following reasons. Basically, temporal changes of surface parameters describe processes occurring on time scales of the orbit repeat time. In other words, modeling temporal decorrelations provides a means to understand and remotely estimate a wide variety of surficial processes such as vegetation growth, permafrost freezing and thawing, and soil moisture and vegetation layer induced effects (Simard et al., 2012).

For instance, it has been shown that both phase and coherence can be used to retrieve soil moisture (e.g. Zwieback et al., 2015a). The coherence, being generally independent of

deformation, provides a better means to estimate soil moisture. However, to retrieve soil moisture using temporal coherence, a decorrelation model should be implemented to separate the soil moisture induced decorrelation, i.e. the change in dielectric constant, from other decorrelation contributions such as the decorrelation due to the change in the geometry of scatterers.

The second area of interest is in the design of orbit repeat for new satellite missions, which is driven by considering some important factors such as tolerable error levels, the attainable baseline, and the expected decorrelation with time of signals from the regions of interest to be mapped (Simard et al., 2012). In this case, temporal decorrelation models can facilitate a priori assessment of the expected coherence levels of interferograms for a new satellite mission designed for a specific application.

Finally, temporal decorrelation models can help better estimate vegetation layer parameters. The total InSAR coherence is the product of spatial, temporal, thermal, volume, and processing coherences (e.g. Lee et al., 2013). Most models used to invert vegetation layer parameters (in PolInSAR studies) only consider the volume decorrelation contribution of the interferometric coherence and ignore other decorrelation contributions. However, leaving non-volumetric decorrelations uncompensated leads to a less accurate parameter estimation. In repeat-pass InSAR systems, the most critical non-volumetric decorrelation contribution is the temporal decorrelation caused by the change of the geometric and/or dielectric properties of the scatterers (Lee et al., 2013) and its contribution to decorrelation can be quantify using temporal decorrelation models.

The rest of this paper is organized as follows. In section 2, InSAR coherence estimates are presented over the study area, Delta Junction, Alaska. The temporal decorrelation model and

evaluation with real data are described in section 3 followed by discussions and conclusions in sections 4 and 5, respectively.

3.2 Study area and data

Our test site, illustrated in Figure 3.1, is located in Delta Junction, interior Alaska. The area is mostly covered by forest and shrub landscapes (Homer et al., 2015) and underlain by discontinuous permafrost. The Alaskan interior between the Alaska and Brooks Mountain Ranges has a strong continental climate with moderate temperatures and precipitation in summer and exceedingly cold and dry weather in winter (O'Neill et al., 2003). The average minimum and maximum annual temperatures in Big Delta station (1937– 2005), which is located in the study area, are -6.9 °C and -2.7 °C, respectively. The lowest and highest temperatures occur in January (-23.7 °C) and July (20.8 °C). Average total precipitation, average total snow-fall, and average snow depth are, respectively, about 29, 111.25, 10.2 centimeters (National Weather Service (http://www.wrcc.dri.edu)).

To study temporal evolution of InSAR coherence, 32 Single Look Complex (SLC) SAR images of L-band ALOS-2 (23.6 cm wavelength) from three ascending and three descending orbital paths in the fine beam and horizontal-horizontal (HH) polarization mode have been used. The data are spanning from August 2014 to March 2017. Each group of the SLC SAR images have been co-registered based on a single master image, which optimizes the geometric and temporal coherence of the interferogram stack. The SLC images were then used to generate interferograms with pixel size of about 30x30 meters. After removing topographic phase, simulated using the National Elevation Dataset (NED) DEM, and applying range spectral shift and azimuth common band filters, linear weighting window size of 5 * 5 (in pixels) was used to estimate correlation. Then, interferograms affected by ionospheric artifacts were excluded and a

total number of 75 interferograms with no or very limited effects of ionospheric artifacts have been selected to analyze temporal coherence. Table 3.1 gives the information of data and interferograms used in this study.

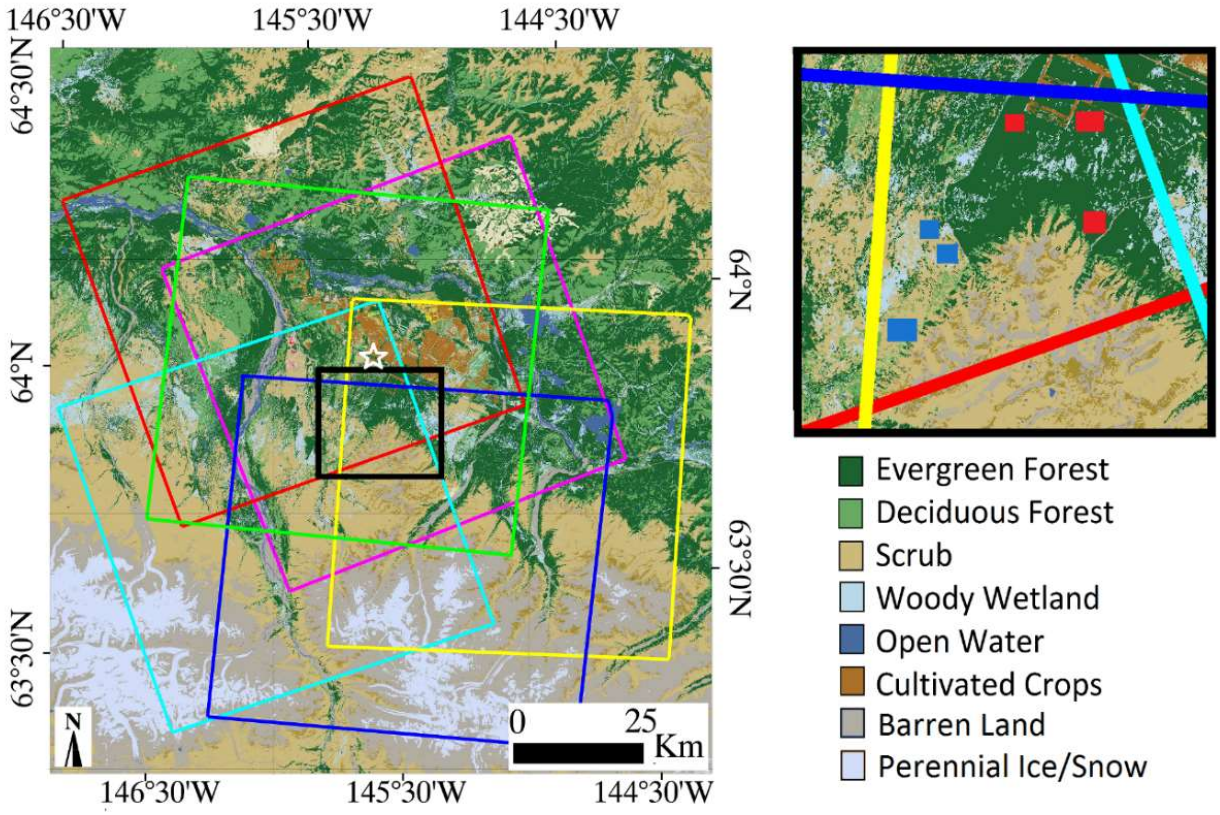

Figure 3.1. Land cover map of the study area (National Land Cover Database 2011 (NLCD 2011)). The orbit- frames covering the study area are shown with different colors (explained in Table 3.1). The black rectangle box shows the overlapping area. The Forested and shrub patches are boxed in red and blue, respectively. The location of SNOTEL Site Granite Creek (963) (Natural Water and Climate Center (https://wcc.sc.egov.usda.gov)) is shown by a white star.

For each of the two major land cover types in the study area, forest and shrub, three patches within flat areas with a total number of 1963 and 1729 pixels, respectively, on geo-referenced coherence images that are fully overlapped with all ALOS-2 observations have been

selected. Figure 3.1 shows the selected patches in red (forest) and blue (shrub) boxes. For each of the interferograms, average coherence values of the selected pixels of each of the land cover types have been calculated. Therefore, each interferogram has two coherence values, one for each of the land cover types, evergreen forest and shrub. Figure 3.2 illustrates the scatter plot of the average coherence versus temporal baseline for the selected patches.

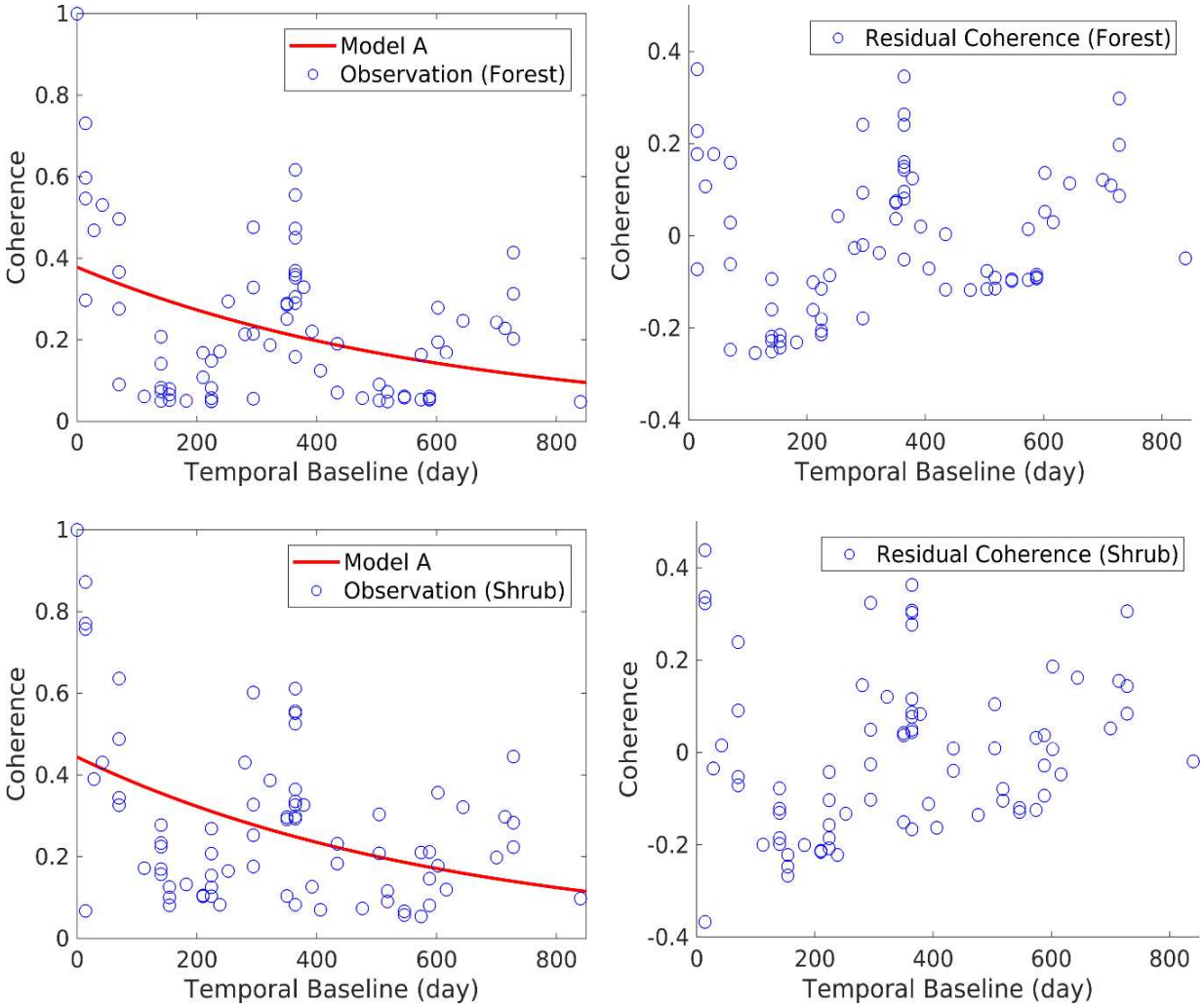

Figure 3.2. Scatter plot of coherence versus temporal baseline and the plot of model A (left) and scatter plot of residual coherence (Observation – Model A) versus temporal baseline (right) for forest (top) and shrub (bottom) landscapes.

Path-Frame	Orbit direction	Number of interferograms	Color of frame on figure 3.1
0040-2330	**D**	**4**	**Yellow**
0041-2330	**D**	**16**	**Blue**
0042-2320	**D**	**10**	**Green**
0137-1280	**A**	**10**	**Magenta**
0138-1280	**A**	**29**	**Red**
0139-1270	**A**	**6**	**Cyan**

Table 3.1. Data used in this study. The letters A and D denote ascending and descending, respectively.

3.3 Methods

3.3.1 InSAR coherence

An InSAR coherence estimation image is a cross-correlation product of two co-registered complex-valued SAR images (e.g. Zebker and Villasenor, 1992; Lu and Freymueller, 1998; Dzurisin and Lu, 2007) which quantifies radar wavelength-scale changes in backscattering characteristics. Decorrelation, i.e. loss of coherence, is generally increased by increasing spatial and temporal baselines between two image acquisitions (Zebker and Villasenor, 1992; Dzurisin and Lu, 2007; Hanssen, 2001). InSAR coherence assesses the accuracy of the estimated deformation and depends on the amount of phase error in an interferogram (Hanssen, 2001;

Bamler and Hartl, 1998; Touzi et al., 1999). Over a small window of pixels, InSAR coherence is estimated by

$$\gamma = \left| \frac{\sum C_1 \, C_2^* \, e^{-j\emptyset}}{\sqrt{\sum |C_1|^2 \sum |C_2|^2}} \right| \tag{3.1}$$

where, C1 and C2 are complex-valued backscattering coefficients, C2* is the complex conjugate of C2, Ø is the deterministic phase due to baseline error, topography, or large deformation in the correlation window.

The total InSAR coherence is the product of spatial (γ_spatial), temporal (γ_temporal), thermal (γ_thermal), volume (γ_volume), and processing (γ_processing) coherences (Lu and Dzurisin, 2014; Zebker and Villasenor, 1992; Hanssen, 2001)

$$\gamma = \gamma_{spatial} * \gamma_{volume} * \gamma_{temporal} * \gamma_{thermal} * \gamma_{processing.} \tag{3.2}$$

The spatial (perpendicular) baselines of our data set, except for two interferograms with spatial baselines of 308 and 347 meters, are smaller than 284 meters with a mean of ~108 meters, whereas the critical baseline of the data is about 11 km. Therefore, a perpendicular baseline of 108 meters, i.e. the mean value of perpendicular baselines, will decrease the coherence by the value of ~0.01 which is negligible. In long wavelength (L-band) SAR sensor, such as ALOS-2 PALSAR-2, the small perpendicular baseline will not affect the variation of spatial decorrelation

much. Therefore, we assumed that the spatial decorrelation from the small range of change in the perpendicular baseline is constant. Also, with such small perpendicular baselines, the volumetric decorrelation is negligible (e.g. Simard et al., 2012). Here, we focus only on temporal decorrelation by assuming that other decorrelation terms are constant or relatively not significant.

3.3.2 Temporal coherence modeling

The temporal coherence is usually considered as a univariate exponential function of time (e.g. Rocca, 2007; Lombardini and Griffiths, 1998) by taking random motion of scatterers in the resolution cell to be the main source of decorrelation,

$$\gamma_A = \gamma_0 e^{-\frac{t}{\tau}} \tag{3.3}$$

where, subscript A denotes model A, $\Upsilon 0$ is initial coherence, t is the time separation between two SAR images, and $1/\tau$ is its decorrelation rate and is mainly dependent on the wavelength of the radar. Based on model A, the exponential decay of coherence values is expected in general by increasing temporal baselines. However, the scatter plots of the observed coherence versus temporal baseline and the scatter plots of the residual coherence, i.e. observation – model A, versus temporal baseline, illustrated in figure 3.2, feature strong undulation with local peaks at temporal baselines around one and two years. Model A takes into account decorrelations due to long-term variations of scatterers' geometry. In real world, however, in addition to the natural and gradual long-term changes in scatterers' geometry, seasonal and/or sudden changes in surface backscattering parameters may also contribute to temporal decorrelation. Generally,

backscattering is dominated by surface dielectric constant and roughness among other surface characteristics. Surface parameters such as soil moisture, vegetation, and temperature alter dielectric constant and roughness, and consequently backscattering coefficients (e.g. Zwieback et al., 2015c; Morishita and Hanssen, 2015; Ulaby et al, 1979). Therefore, other term(s) should be added to the temporal coherence function to compensate the effects of changes in surface backscattering between two image acquisitions.

In this paper, we have modified the coherence model to accommodate decorrelations due to the change in surface backscattering parameters. Since SAR backscatter coefficient and consequently SAR intensity varies as a function of the changes in surface parameters (e.g. Zhang et al., 2003; Zibri et al., 2014), here, we use the change in SAR intensity as a proxy for the changes in surface backscattering. Figure 3.3 shows semi-logarithmic scatter plot of coherence ratio, i.e. observation / model A, versus relative intensity change between two images. Relative intensity is calculated by $r = |10\log(i_2/i_1)|$, which i2 and i1 are SAR intensities of first and second images, respectively. Considering the linear trend fitted to the semi-logarithmic scatter plots (note R^2 value and very small *P-value* of the linear regressions), model B is postulated to be

$$\gamma_B = \gamma_0 \, e^{-(\frac{t}{\tau}+\frac{r}{\rho})} \tag{3.4}$$

where, r is the relative change in SAR intensity, i.e. backscattering baseline, and 1/ρ is its decorrelation rate. For each of the fitted linear trend, R^2 and *P-value* of the regression are calculated and shown on the plots. Note that if the P-value of a t-test is smaller than the common alpha values of 0.1, 0.05, and 0.01 (the confidence level of 90, 95, and 99%, respectively), the

null-hypothesis is rejected. It means that the additional term related to the relative change in SAR intensity is likely correlated with temporal correlation.

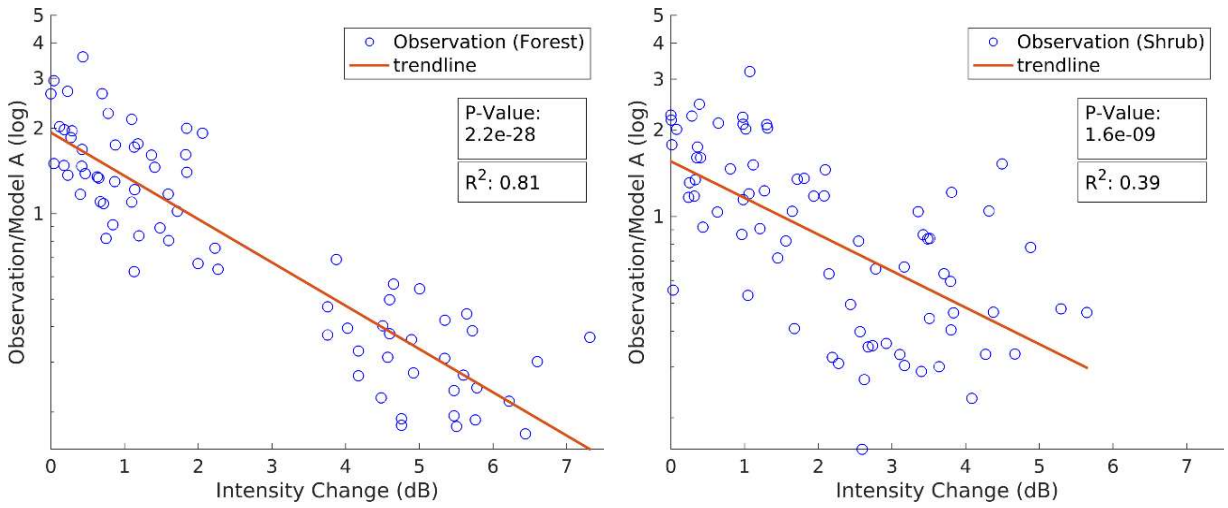

Figure 3.3. Semi-logarithmic scatter plot of coherence ratio, i.e. observation / model A, versus relative intensity changes for forested and shrub land cover types.

The unknown parameters in models A and B, i.e. $\Upsilon 0$, τ, and ρ can be estimated by solving the equations using known variables, i.e. Υ, t, and r. The coherence, Υ, is estimated using equation (3.1). The temporal baseline of the interferograms, t, ranges between 14 and 840 days. Figure 3.4 illustrates the scatter plots of model B, observed coherence, and residual coherence values (observation – model B) for the two landscapes. For comparison, the scatter plot of water body's coherence is also shown in the figure. Also, table 3.2 exhibits the model parameters and RMS error for each model. The RMS error values of model B for the both land cover types are

smaller than those of model A, indicating that model B estimates more accurate coherence values. A detail discussion of how significant is the improvement has been provided in section 4.

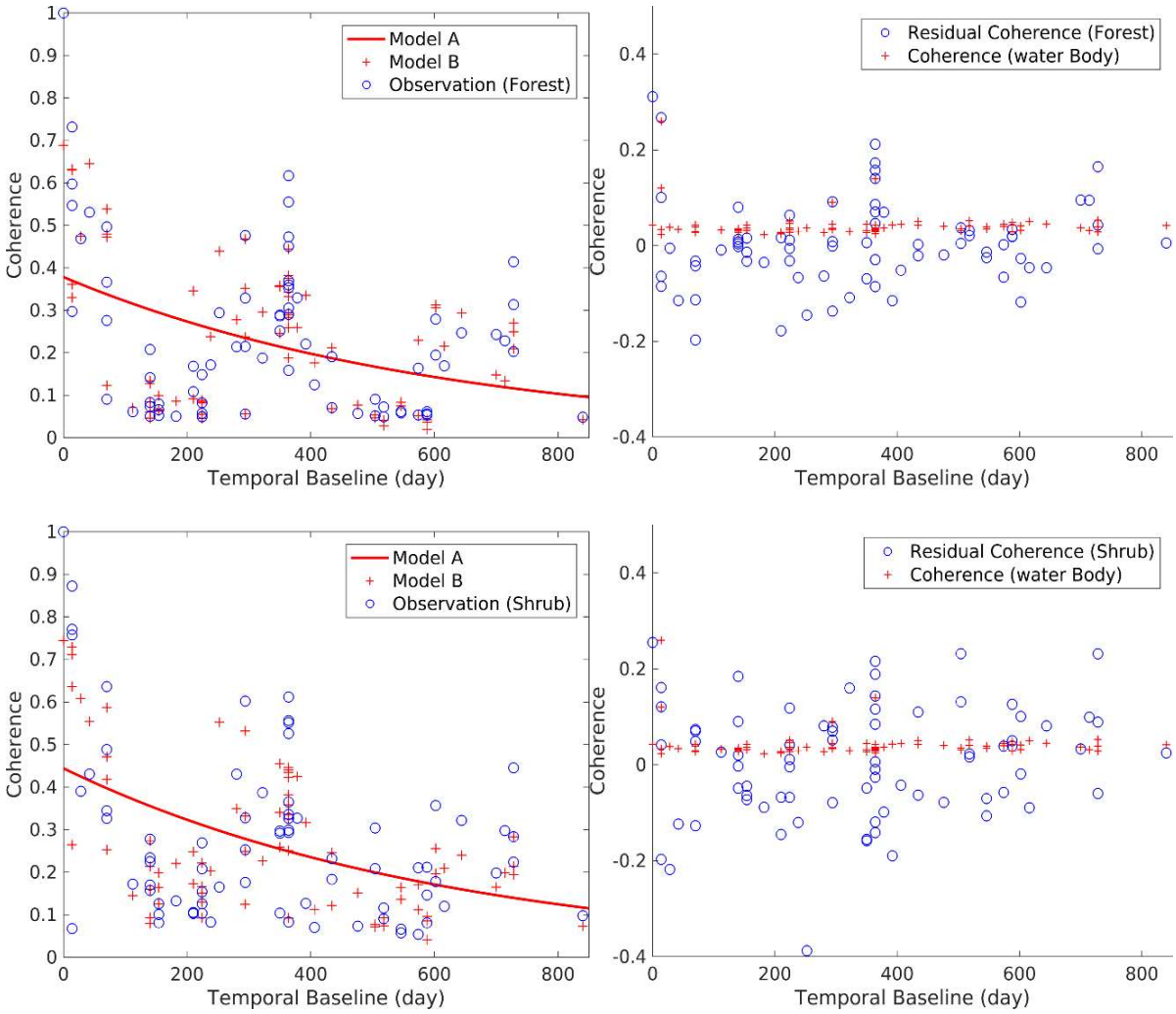

Figure 3.4. Plot of model A and the scatter plot of model B and observed coherence values, scatter plot of residual coherences (observation – model B) versus temporal baseline for the two landscapes and scatter plot of coherence of a water body.

model	Land cover	Υ_0	τ (day)	ρ	σ	RMS	f-test	C_f (α=0.01)
A	**Forest**	**0.37824**	**616.49**	**-**	**-**	**0.180**	**-**	**-**
	Shrub	**0.444**	**629.53**	**-**	**-**	**0.186**	**-**	**-**
B	**Forest**	**0.68885**	**861.07**	**2.5406**	**-**	**0.092**	**205.84**	**6.99**
	Shrub	**0.74482**	**879.27**	**2.5467**	**-**	**0.121**	**102.38**	**6.99**
C	**Forest**	**0.73842**	**903.7**	**3.3464**	**0.62062**	**0.083**	**16.23**	**7.00**
	Shrub	**0.79153**	**913.47**	**5.6462**	**0.37348**	**0.101**	**29.64**	**7.00**

Table 3.2. Model parameters of the two land cover types. Cf is critical f-value.

Different snow depths between two images of an interferometric pair is one of the factors that can induce variations in surface scattering behavior, which in turn leads to decorrelation. Basically, between two winter images in stable frozen conditions with no change in soil moisture, the change in dielectric constant is negligible and high coherence values can be expected for open areas (Thiel and Schmullius, 2016). However, the change in snow depth between the two images may change surface scattering behavior, which in turn causes decorrelation. Here, we intend to modify our coherence model by adding the decorrelation term of snow depth changes. The basic assumption here is that the intensity and snow depth changes are independent parameters, i.e. systematic snow depth change doesn't produce systematic intensity change. Figure 3.5, illustrating scatter plot of intensity change versus snow depth changes, shows no trend and indicates that the two parameters are independent.

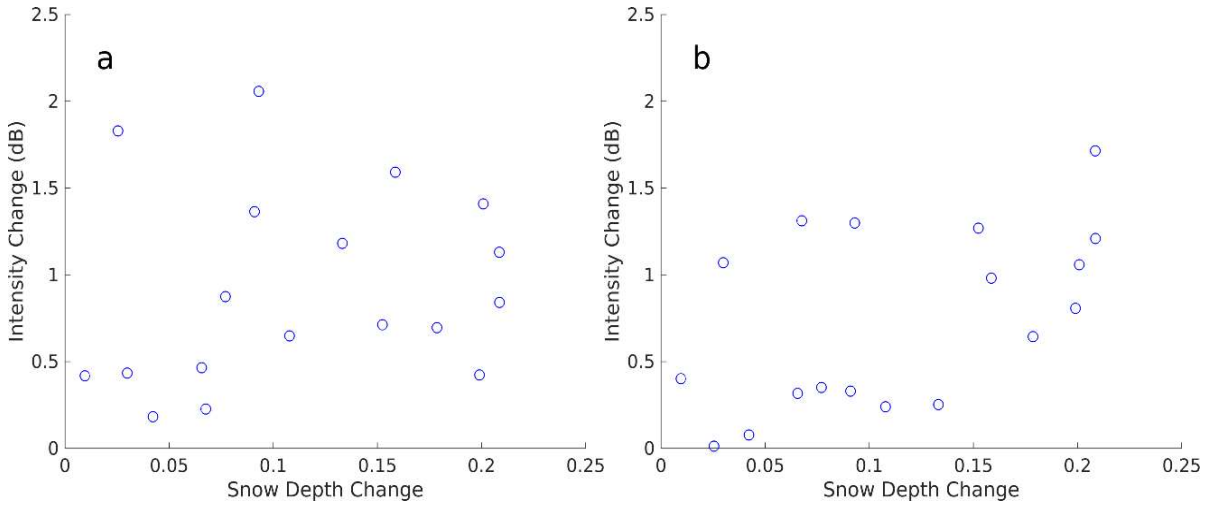

Figure 3.5. Scatter plot of model intensity changes (dB) versus snow depth changes (meter) for a) forested and b) shrub land cover types.

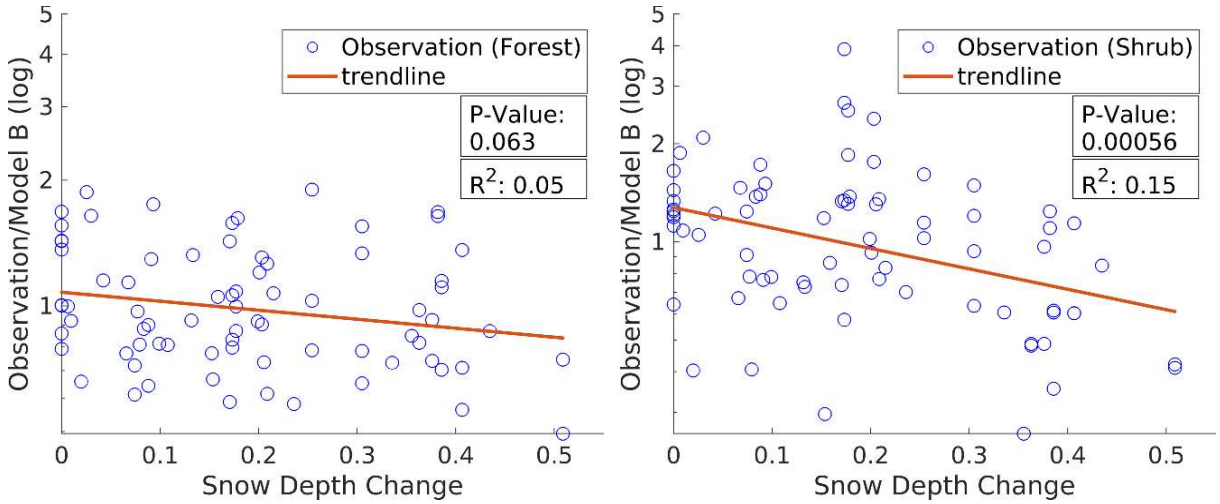

Figure 3.6. Semi-logarithmic scatter plot of coherence ratio, i.e. observation / model B, versus snow depth changes (meter) for forested and shrub land cover types.

Figure 3.6 shows semi-logarithmic scatter plot of coherence ratio, i.e. observation / model B, versus snow depth change between two images. Considering the linear trend fitted to the semi-logarithmic scatter plots, model C is postulated to be

$$\gamma_C = \gamma_0 \, e^{-(\frac{t}{\tau}+\frac{r}{\rho}+\frac{s}{\sigma})} \tag{3.5}$$

where, s is snow depth changes between to images and 1/σ is its decorrelation rate. The unknown parameters in model C is estimated by solving the equations using known variables. The snow depth values are acquired from SMAP level 4 data (National Snow and Ice Data Center (http://nsidc.org)) and the measurements at the SNOTEL Site Granite Creek (963) (Natural Water and Climate Center (https://wcc.sc.egov.usda.gov)), which is located in our study area (white star in Figure 3.1). Figure 3.7 illustrates the scatter plots of model C, observed coherence, and residual coherence values (observation – model C) for the two landscapes. For comparison, the scatter plot of water body's coherence is also shown. Also, Table 3.2 exhibits the model parameters and RMS error for each model. The RMS error values of model C for the two land cover types are smaller than those of model B. This means that the change in snow depth leads to decorrelation and taking into account its effect on InSAR coherence improves the model's performance. A statistical analysis of how significant is the improvement has been provided in the next section.

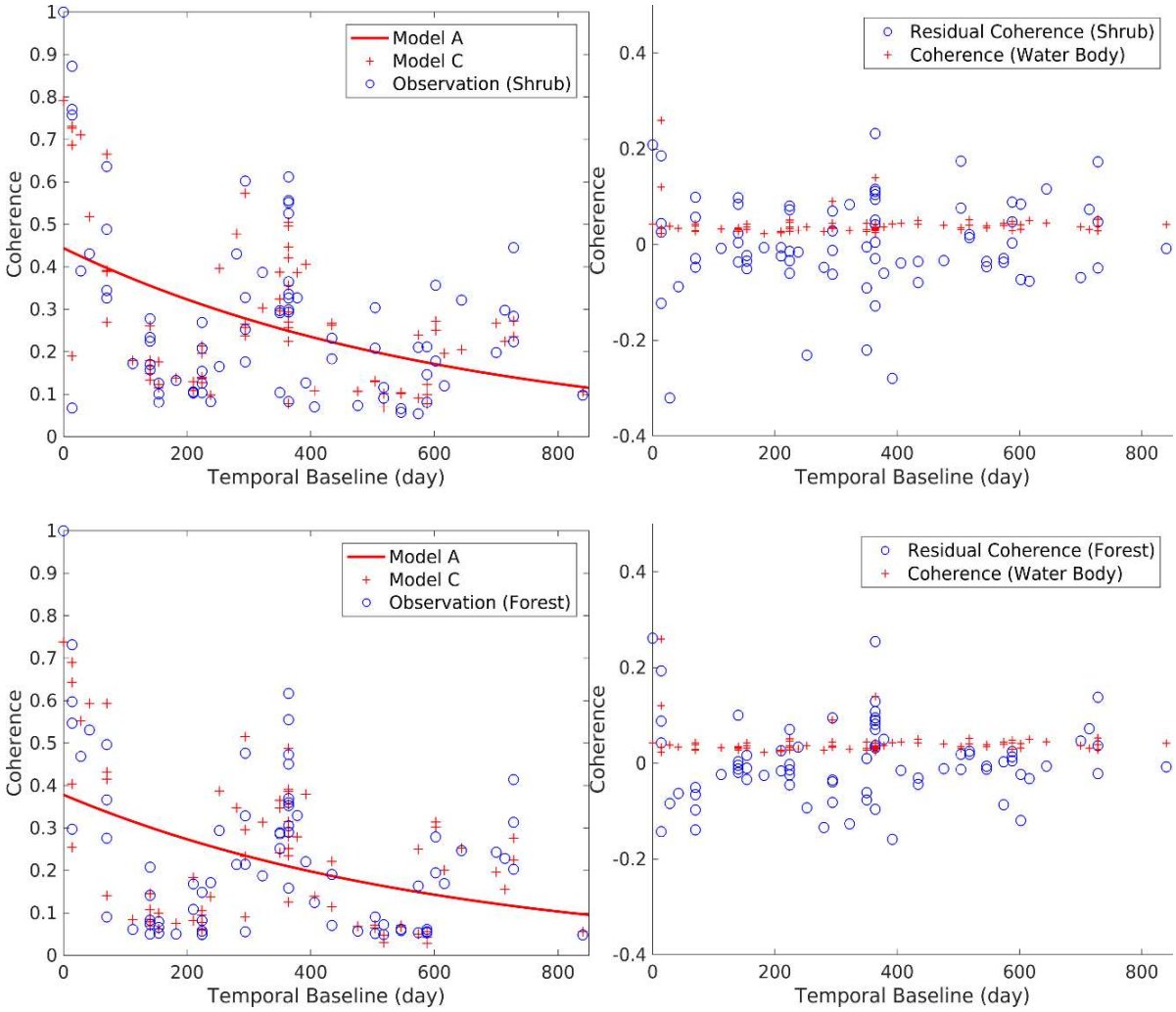

Figure 3.7. Plot of model A and the scatter plot of model C and observed coherence values, scatter plots of residual coherences (observation – model C) versus temporal baseline for forested and shrub land cover types and scatter plot of water body's coherence.

3.4 Discussion

3.4.1 Scatterers' type and decorrelation sources

Model C has three terms. The first term, exp (-t/τ), is the long-term irreversible decorrelation due to the temporal change in scatterers' geometry. The second term, exp (-r/ρ), is the decorrelation due to the changes in backscattering between two images. As stated earlier, the

change in SAR intensity was used as a proxy for the change in the surface backscattering. Figure 3.8 shows the plot of SAR intensity (dB) over forest and shrub landscapes versus the soil moisture measured at the SNOTEL Site Granite Creek (963) (Natural Water and Climate Center (https://wcc.sc.egov.usda.gov)) which is located in our study area and is 12 km away in average from the patches (see figure 3.1). The plots demonstrate a general correlation between soil moisture and SAR intensity, indicating that the change in backscattering and SAR intensity is most likely dominated by the change in dielectric constant of scatterers induced by the change in soil and biomass water content.

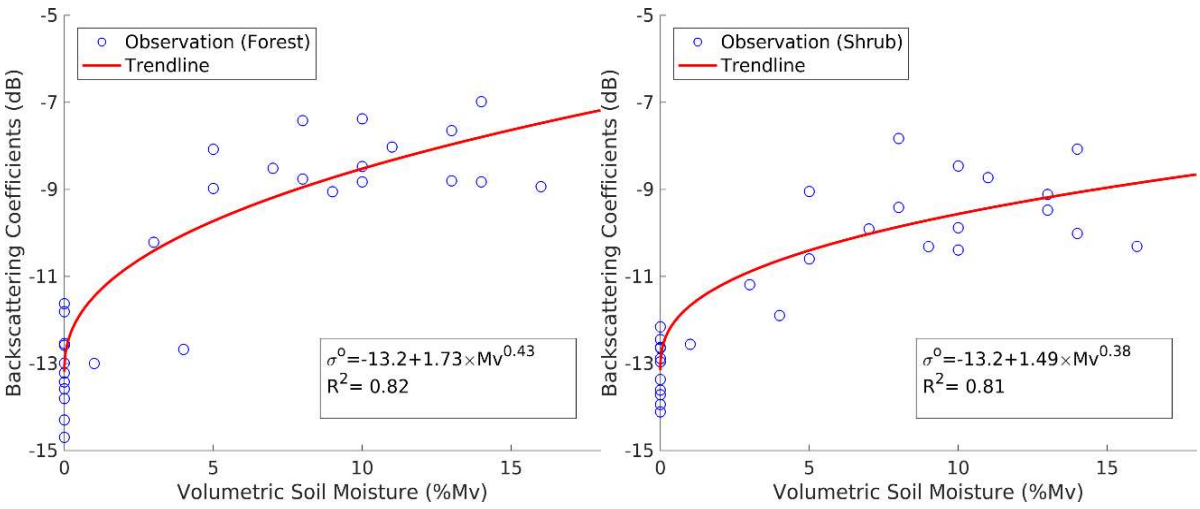

Figure 3.8. Plot of the change in SAR intensity versus the change in soil moisture measured at the SNOTEL Site Granite Creek (963) (Natural Water and Climate Center (https://wcc.sc.egov.usda.gov)). Data under conditions of frozen and unfrozen are included.

The third term, exp (-s/σ), is the decorrelation due to the change in snow depth between two images. The scatterplot of InSAR intensity change (dB) versus snow depth change for soil moisture-free, i.e. winter-winter, interferograms (Figure 3.5) shows no correlation between SAR

intensity change and snow depth change over forested and shrub landscape indicating that snow depth change-induced decorrelation is most likely dominated by the change in scatterers' geometry. In the section 4.3, we will perform statistical assessment to show that the improvement made by considering snow depth change in the model is statistically significant.

In a case where the temporal evolution of surface parameters such as soil moisture, vegetation layer parameters, and snow depth are known, the general coherence is postulated to be

$$\gamma = \gamma_0 \, e^{-\left(\frac{t}{\tau} + \sum_{i=1}^{n} \frac{p_i}{\mu_i}\right)} \tag{3.6}$$

where, 1/μi is the decorrelation rate of the parameter pi, which is the change in the surface parameters between two images.

In general, shrub landscape is more stable as changes happen in scatterers' geometry and dielectric constant. Except the decorrelation rate of the change in snow depth, which is lower for forest, the decorrelation rates of long-term and backscattering are lower, i.e. higher τ and ρ values, for shrub landscape compared to the forested landscape (Table 3.2). The scatterers within a resolution cell are of two types, scatterers associated with ground surface and scatterers associated with vegetation layer. Forested landscape (coniferous in this research) possess more backscattering contribution from vegetation layer compared to shrub landscape. Since the mutual position of scatterers within a vegetation layer, i.e. the geometry of scatterers, is more likely subject to change than the geometry of the scatterers within a non-vegetated surface, forested area in long term decorrelates faster than non-forested area as time lapses. Therefore shrub is

expected to have lower decorrelation rate associated with the long-term change in scatterer's mutual position (table 3.2). Also, the observed higher backscattering decorrelation rate of the forested area is associated in part with dielectric variation within the vegetation layer due to, for example, changing water content within the trees. Similarly, the observed higher snow depth decorrelation rate in shrub is associated with the type of scatterers within each landscape. Lower proportion of snow-covered scatterers within vegetation layer causes forested landscape to lose coherence with lower rate compared to non-forested landscape as the change in snow depth increases.

The long-term decorrelation rate of forest is slightly higher than the one of shrub landscape, whereas the backscattering decorrelation rate of forest is almost two times greater than that of shrub landscape. This infers that, with short-baseline data sets, the difference between the temporal decorrelation of snow-free forested and non-forested areas is dominated by the decorrelation induced by the change in the dielectric constant of scatterers within vegetation layer and not by the change in the geometry of scatterers within the vegetation layer.

3.4.2 The effect of seasonality on temporal coherence

Figure 3.9 depicts coherence as a 3D surface and provides a visual comparison of coherence evolutions of the two land cover types, forested and shrub. The x-axis of the plot is the relative change in SAR intensity and ranges between 0 and 0.65, i.e. the maximum measured relative intensity change, whereas the y-axis is the change in snow depth and ranges between 0 and 0.65 m. It is shown that the both land cover types, even with short temporal baselines, can lose coherence due to the changes in dielectric constant and snow depth. Also, it is illustrated that forest loses coherence with higher rate than shrub with changing backscattering (dielectric

constant), whereas shrub is more prone to decorrelation as the change in snow depth between two image increases.

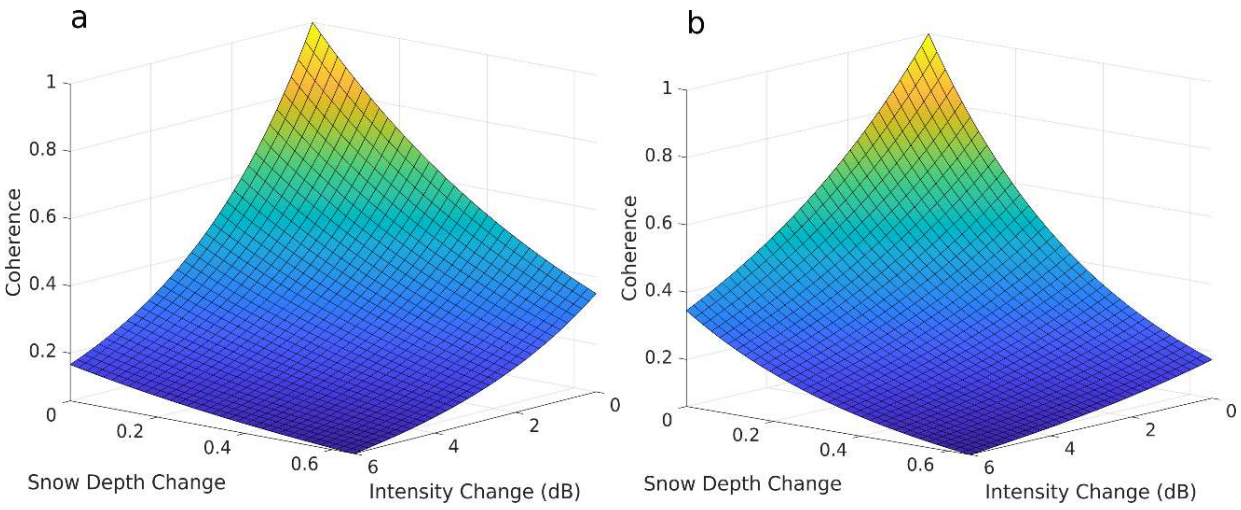

Figure 3.9. Coherence curve of the two land cover types, a) forest, and b) shrub land cover types.

Land cover	Group	Mean	SD	SD/Mean
	S	**0.3433**	**0.0711**	**0.2070**
Forest	**W**	**0.3703**	**0.0680**	**0.1835**
	C	**0.0896**	**0.0407**	**0.4546**
	S	**0.3905**	**0.0974**	**0.2495**
Shrub	**W**	**0.4074**	**0.0836**	**0.2052**
	C	**0.1522**	**0.0566**	**0.3720**

Table 3.3. Statistical properties, i.e. mean and Standard Deviation (SD), of interferograms categories. The letters S, W, and C denote summer-summer, winter-winter, and cross-season interferogram groups.

Table 3.3 shows statistical properties of the observed coherence values of the two land cover types. The interferograms of each land cover type is subdivided into three sub-groups, summer, winter, and cross-season interferogram categories. It is shown that shrub has higher coherence value than forest. Also, winter and cross-season interferogram categories possess highest and lowest coherence values in general.

Basically, the different scatterers' type and structure within forested and non-forested resolution cells may result in different decorrelation processes when seasonal or sudden variations in surface parameters and meteorological conditions happen. During a frozen season, decreased dielectric constant leads to reduced attenuation and deeper penetration of electromagnetic waves into forest canopy (Thiel and Schmullius, 2016; Kwok et al., 1994; Way et al., 1988). Consequently, this will cause a decrease in backscatter and influence polarimetric signature and InSAR coherence (Thiel and Schmullius, 2016; Kwok et al., 1994; Way et al., 1988; Dobson et al., 1990; Santoro et al., 2015). In terms of coherence, between two winter images in stable frozen conditions, water content (soil moisture) changes do not occur leading to low temporal decorrelation for open areas (Thiel and Schmullius, 2016). This means that higher InSAR coherence is expected for winter interferograms. Basically, over frozen forests, compared to unfrozen condition, more volumetric decorrelation is expected to happen as perpendicular baseline increases, owing to deeper penetration of electromagnetic waves into frozen forest canopy (Thiel and Schmullius, 2016). However, with short-baseline interferograms of L-band ALOS-2 and future data sets with narrower orbital tubes, the volumetric decorrelation induced by the deeper penetration of electromagnetic waves into frozen soil and frozen forest canopy becomes low resulting in higher winter coherences.

During unfrozen condition, changing soil moisture, variable water content within the trees, growth-related changes, and wind are among the major sources of temporal decorrelation (Dobson, 1988; McDonald et al., 2002). The variation of the aforementioned surface parameters and meteorological conditions, in turn, results in decreased temporal coherence of unfrozen condition compared to frozen condition (Thiel and Schmullius, 2016).

3.4.3 Statistical assessment on models' performance

To statistically assess the improvements of models B and C, which have respectively one and two more parameters compared to model A, we used F-test (explained, for example, in (Davis, 2002)),

$$F = \frac{SSR_1 - SSR_2}{SSR_2} \frac{n - P_2}{P_2 - P_1} \tag{3.7}$$

where SSR is the sum of squared residuals of the model, P is the number of free model parameters, and n is the number of observations. If the calculated F-test value is greater than the upper-tailed critical value of the F-distribution, FP2-P1, n-P2, α, then with 1-α percentage confidence, the null hypothesis is rejected, i.e. the improvement is statically significant. The calculated F-test values and critical F-distributions values with 99% confidence level (probability level of 0.01) have been presented in table 3.2. All the calculated F-test values are greater than the critical values in a 99% confidence level, indicating that the improvements made by new models are statistically significant.

3.5 Conclusions

Model C, takes into account the long-term irreversible/long-term changes in scatterers' geometry, reversible/seasonal changes in scatterers' dielectric constant, induced mainly by the change in soil and biomass water content, and reversible/seasonal changes in scatterers' geometry, i.e. the third term, due to the change in snow depth. Shrub, in general is more stable than forest as time lapses and variations happen in surface backscattering properties. Also, the results show high coherence values for winter interferograms compared to summer ones owing to the stable condition of frozen season. Our model illustrates that snow depth difference between interferogram pair causes decorrelation, which is shown to be mainly resulted from the change in scatterers' geometry.

This paper argues that with short-baseline interferograms of L-band ALOS-2 and future data sets with narrower orbital tubes, the differences between temporal decorrelation rates of forest and non-forested areas, in snow free condition, is dominated by the change in dielectric constant of scatterers and not by the change in their geometry. It should be noted that the model introduced here is based on L-band data and therefore might not be expanded to C-band or X-band InSAR observations. The model provides accurate estimation of InSAR coherence for coniferous forested and shrub land cover types. However, its accuracy over other terrain types should be assessed.

Acknowledgments: ALOS-2 PALSAR data copyrighted Japan Aerospace Exploration Agency (JAXA). We thank Paul Siqueira for facilitating the data access and Scott Hensley for providing several good references. The work was funded by the NASA Earth Surface & Interior Program (NNX16AK56G) and the Shuler-Foscue Endowment at Southern Methodist University.

The authors would like to thank the academic editor and three reviewers for their very constructive comments and suggestions.

References

Massonnet, D., and K. Feigl. 1998. Radar interferometry and its application to changes in the Earth's surface, *Rev. Geophys.,* 36, 441-500.

Bürgmann, R., P.A. Rosen, and E.J. Fielding. 2000. Synthetic aperture radar interferometry to measure Earth's surface topography and its deformation. Annu. Rev. *Earth Planet. Sci.,* 28, 169–209.

Simons, M., and P. Rosen. 2007. Interferometric Synthetic Aperture Radar Geodesy. *Treatise Geophys. Geodesy*, 3, 391–446.

Lu, Z., and D. Dzurisin. 2014. InSAR Imaging of Aleutian Volcanoes: Monitoring a Volcanic arc from Space, Geophysical Sciences, Springer Praxis Books, Springer: Chichester, UK, 2014, p. 390.

Ferretti, A., C. Prati, and F. Rocca. 2001. Permanent scatterers in SAR interferometry. IEEE Transactions on Geoscience and Remote Sensing, 39, 8–20.

Kim, J.W., Z. Lu, and K. Degrandpre. 2016. Ongoing Deformation of Sinkholes in Wink, Texas, Observed by Time-Series Sentinel-1A SAR Interferometry (Preliminary Results), *Remote Sensing*, 8, 313, doi:10.3390/rs8040313.

Hu, X., T. Wang, T.C. Pierson, Z. Lu, J.W. Kim, and T.H. Cecere. 2016. Detecting seasonal landslide movement within the Cascade landslide complex (Washington) using time-series SAR imagery. *Remote Sensing of Environment*, 187, 49-61.

Rykhus, R., and Z. Lu. 2008. InSAR detects possible thaw settlement in the Alaskan Arctic Coastal Plain. *Can. J. Remote Sens*., 34, 100–112.

Liu, L., T. Zhang, J. and Wahr. 2010. InSAR measurements of surface deformation over permafrost on the North Slope of Alaska. *J. Geophys. Res*., 115, F03023, doi: 10.1029/2009JF001547.

Zebker, H., and J. Villasenor. 1992. Decorrelation in interferometric radar echoes. *IEEE Trans. Geosci. Remote Sens*., 45, 950–959.

Just, D., and R. Bamler. 1994. Phase statistics of interferograms with applications to synthetic aperture radar. *Applied Optics*, 33(20), 4361-4368. doi: 10.1364/AO.33.004361

Simard, M., S. Hensley, and M. Lavalle. 2012. An empirical assessment of temporal decorrelation using the uninhabited aerial vehicle synthetic aperture radar over forested landscapes. *Remote Sens.*, 4, 975–986.

Rocca, F. 2007. Modeling Interferograms Stacks. IEEE Trans. Geosci. Remote Sens., 45, 3289–3299.

Luo, X., J. Askne, G. Smith, and P. Dammert. 2001. Coherence characteristics of RADAR signals from rough soil. *Prog. Electromagn. Res*., 31, 68–88.

Zwieback, S., S. Hensley, and I. Hajnsek. 2015a. Assessment of soil moisture effects on L-band radar interferometry. *Remote Sens. Environ*. 2015, 164, 77–89, doi:10.1016/j.rse.04.012.

Zwieback, S., C. Paulik, and W. Wagner. 2015b. Frozen soil detection based on advanced scatterometer observations and air temperature data as part of soil moisture retrieval. *Remote Sens.,* 7 (3), pp. 3206–3231.

Zwieback, S., S. Hensley, and I. Hajnsek. 2015c. A Polarimetric First-Order Model of Soil Moisture Effects on the DInSAR Coherence. *Remote Sens.*, 7, 7571–7596, doi: 10.3390/rs70607571

Lavalle, M., M. Simard, S. Hensley. 2012. A temporal decorrelation model for polarimetric radar interferometers. *IEEE Transactions on Geoscience and Remote Sensing*, 50, pp. 2880-2888, 10.1109/TGRS.2011.2174367.

Zhang, L., J. Shi, Z. Zhang, and K. Zhao. 2003. The estimation of dielectric constant of frozen soil-water mixture at microwave bands. In Proceedings of the *IEEE International Geoscience and Remote Sensing Symposium*, Toulouse, France, 21–25 July 2003, IEEE: Piscataway, NJ, USA, 2003; pp. 2903–2905.

Zhang, T., Q. Zeng, Y. Li, and Y. Xiang. 2008. Study on relation between InSAR coherence and soil moisture. In Proc. ISPRS Congr., vol. 37, pp. 131–134.

Borgeaud, M., and U. Wegmueller. 1996. On the use of ERS SAR interferometry for the retrieval of geoand bio-physical information. In Proceedings of the '*Fringe 96'* Workshop on ERS SAR Interferometry, 30 September–2 October 1996, Zurich, Switzerland, pp. 83–94.

Morishita, Y., and R.F. Hanssen. 2015. Temporal Decorrelation in L-, C-, and X-band Satellite Radar Interferometry for Pasture on Drained Peat Soils. *IEEE Trans. Geosci. Remote Sens*., 53, 1096–1104.

Lee, S.-K., F. Kugler, K.P. Papathanassiou, and I. Hajnsek. 2013. Quantification of temporal decorrelation effects at L-band for polarimetric SAR interferometry applications. IEEE J. Sel. Top. Appl. Earth Obs. *Remote Sens*., 6, 1351–1367.

Homer, C.G., J.A. Dewitz, L. Yang, S. Jin, P. Danielson, G. Xian, J. Coulston, N.D. Herold, J.D. Wickham, and K. Megown. 2015. Completion of the 2011 National Land Cover Database for the conterminous United States-Representing a decade of land cover change information. *Photogrammetric Engineering and Remote Sensing*, v. 81, no. 5, p. 345-354.

O'Neill, K.P., E.S. Kasischke, and D.D. Richter, 2003. Seasonal and decadal patterns of soil carbon uptake and emission along an age-sequence of burned black spruce stands in interior Alaska, *Journal of Geophysical Research*, 108 (D1), doi:1029/2001JD000443.

Lu, Z., and J. Freymueller. 1998. Synthetic aperture radar interferometry coherence analysis over Katmai volcano group, Alaska, *J. Geophys. Res*., 103, 29,887-29,894.

Dzurisin, D., and Z. Lu. 2007. Interferometric Synthetic Aperture Radar (InSAR) (Chapter 5): Volcano Deformation: Geodetic Monitoring Techniques (by D. Dzurisin), Springer-Praxis Publishing Ltd., UK, 153-194.

Hanssen, R. 2001. Radar Interferometry: Data Interpretation and Error Analysis, vol. 2. Dordrecht, The Netherlands: Kluwer.

Bamler, R., and P. Hartl. 1998. Synthetic Aperture Radar Interferometry. *Inverse Problems*, Vol. 14, R1.

Touzi, R., A. Lopes, J. Bruniquel, and P. Vachon, 1999. Coherence estimation for SAR imagery. *IEEE Trans. Geosci. Remote Sens*., vol. 37, no. 1, pp. 135–149.

Lombardini, F., and H. Griffiths. 1998. Effect of temporal decorrelation on 3D SAR imaging using multiple pass beamforming, in Proc. IEE/ EUREL Meet. Radar Sonar Signal Process., Peebles, U.K., Jul. 1998, pp. 1–4.

Ulaby, F. T., G. A. Bradley, and M. C. Dobson. 1979. Microwave backscatter dependence on surface roughness, soil moisture, and soil texture, II, Vegetation covered soil. *IEEE Trans. Geosci. Electron*., GE-17, 33- 40.

Zribi, M., A. Gorrab, N. Baghdadi. 2014. A new soil roughness parameter for the modelling of radar backscattering over bare soil. *Remote Sens. Environ*., 152, 62–73.

Thiel, C., and C., Schmullius. 2016. The potential of ALOS PALSAR backscatter and InSAR coherence for forest growing stock volume estimation in Central Siberia, *Remote Sensing of Environment*, 173 , 258-273.

Kwok, R., E. J. M. Rignot, J. Way, A. Freeman, and J. Holt. 1994. Polarization signatures of frozen and thawed forests of varying environmental state. *IEEE Transactions on Geoscience and Remote Sensing,* 32, 371–381.

Way, J., J. Paris, E. Kasischke, C. Slaughter, L. Viereck, N. Christensen, and J. Weber. 1990. The effect of changing environmental-conditions on microwave signatures of forest

ecosystems — Preliminary-results of the March 1988 Alaskan aircraft SAR experiment. *International Journal of Remote Sensing*, 11, 1119–1144.

Dobson, M. G., K. McDonald, and F.T. Ulaby. 1990. Effects of temperature on radar backscatter from boreal forests. In R. Mills (Ed.), IEEE international geoscience and remote sensing symposium IGARSS (pp. 2481–2484). College Park, Maryland, USA: *IEEE Publications*.

Santoro, M., L. Eriksson, and J. Fransson. 2015. Reviewing ALOS PALSAR backscatter observations for stem volume retrieval in Swedish forest. *Remote Sensing*, 7, 4290–4317.

Dobson, M. C. 1988. Diurnal and seasonal variations in the microwave dielectric constant of selected trees. In T. D. Guyenne, & J. J. Hunt (Eds.), *IEEE international geoscience and remote sensing symposium IGARSS 1988* (pp. 1754). Edinburgh, U.K.: ESA Publications Devision.

McDonald, K. C., R. Zimmermann, and J.S. Kimball. 2002. Diurnal and spatial variation of xylem dielectric constant in Norway spruce (Picea abies [L.] karst.) as related to microclimate, xylem sap flow, and xylem chemistry. *IEEE Transactions on Geoscience and Remote Sensing*, 40, 2063–2082.

Davis, J.C. 2002. Statistics and Data Analysis in Geology, 3rd Edition. *John Wiley and Sons*, Hoboken.

CHAPTER 4

INFLUENCE OF THE STATISTICAL PROPERTIES OF PHASE AND INTENSITY ON INSAR PHASE AND COHERENCE, AND CLOSURE PHASE

Molan, Y.E., Z. Lu, and J-W. Kim. 2020. Influence of the statistical properties of phase and intensity on closure phase, *IEEE TGRS*.

4.1 Introduction

InSAR has the ability to remotely sense mm to cm scale surface deformation with a high spatial resolution of tens of meters or better, irrespective of weather and time of day (Massonnet and Feigl, 1998; Lu and Dzurisin, 2014). Surface deformations due to various mechanisms, such as volcanism, subsidence, permafrost, and landslides, have been successfully detected using InSAR (Shirzaei, and R. Bürgmann, 2013; Molan et al., 2018a, 2018b; Ferretti et al., 2001; Rykhus and Lu, 2008; Agram et al., 2013; Fattahi etal., 2007). In addition to deformation mapping, interferometric phase has been also used to estimate soil moisture changes (De Zan et al., 2015; Zwieback et al., 2016; Molan and Lu, 2020; Nolan et al., 2003). The common approach in the literature to estimate soil moisture is to define a relationship between the mean soil moisture value and InSAR phase and intensity changes. This is because the change in soil moisture will induce a change in dielectric constant. Dielectric constant of soil manipulates the depth and the attenuation of electromagnetic waves penetrating the soil. Basically, the depth of penetration decreases but at the same time wave-number increases by increasing soil moisture.

This leads to phase increase, which is manifested as subsidence on interferograms (Zwieback et al., 2016; Hensley et al., 2011).

The phase of interferograms generated from single-looked pixels are rather noisy due to strong effects of decorrelations and noises. One way to deal with this problem is using multi-looked interferograms. Multi-looking reduces the noise and improves the reliability of phase unwrapping by averaging adjacent pixels in the complex interferogram (Ferretti et al., 2015; Goldstein et al., 1988). Another approach is exploring SqueeSAR (Ferretti et al., 2015), and the component extraction and selection SAR (CAESAR) algorithms (Fornaro et al., 2015; Verde et al., 2018), which have been developed to extend Persistent Scatterers Interferometry (PSI) analysis. SqueeSAR overcomes the influence of temporal and geometrical decorrelation on Distributed Scatterers (DSs) in non-urban areas (Ferretti et al., 2015; 15, Fornaro et al., 2015; Verde et al., 2018). The strength of CAESAR is the possibility of extracting multiple dominant scattering mechanisms within a resolution element based on the analysis of the covariance matrix (Verde et al., 2018).

Multi-looking, however, leads to non-zero phase triplet. Two SAR images from the same orbital track taken at different times can be used to generate a multi-looked interferogram. Likewise, using three SAR images, three mutual interferograms can be generated. One may assume that the phase of the multi-looked interferogram pairing the first and the last SAR images equals the summation of the phases of the two intermediate interferograms. In the real world, however, the assumption is violated because experiences show otherwise; this phenomenon is known as phase inconsistency.

The possible causes of non-zero phase triplet have been recently discussed in the literature. De Zan et al., 2015, argued that phase inconsistencies can arise when different

scatterer populations with independent phase behaviors interfere with each other. They illustrated that changes in the water content of soil and vegetation could contribute to phase inconsistency. The three-dimensional structure of the scatterers within the resolution cell can also possibly cause phase inconsistency in the case of a non-zero spatial baseline (De Zan et al., 2015). Zwieback et al., 2016, argued that apart from deformations, which do not cause phase inconsistency, there should be other factors influencing phase inconsistency. The authors attributed the phase inconsistencies to non-random effects of decorrelation noise, the change in dielectric constant, and non-zero spatial baselines. The phase inconsistency induced by the changes in dielectric constant has been reported in the observations and interferometric models introduced recently (De Zan et al., 2015). The change in dielectric constant is ascribed to the change in soil moisture and water content of vegetation (De Zan et al., 2015; Zwieback et al., 2016; Molan and Lu, 2020) and also to the freeze-thaw condition of soil (Zwieback et al., 2016).

Unlike previous studies that attribute non-zero phase closure to the changes in three dimensional-structure or dielectric constant of single-looked pixels, in this paper, we show that non-zero phase triplet is only related to the statistical properties of the pixels within the multi-looked window. One simple reason for this argument is that phase inconsistency, i.e. non-zero phase triplet, does not exist in single looked images but rather only in multi-looked images. Therefore, analyzing the influence of the statistical properties of intensity and phase changes of single-looked pixels on multi-looked phase would quantify the extent of their influence on phase triplet.

Multi-looked phase and coherence are functions of phase (deforming and non-deforming) changes of single-looked pixels and the way that the physical changes are distributed in the multi-looking window (Just and Bamler, 1994; Anxi et al., 2014; Lopes et al., 1992). This is to

say that the multi-looked phase contains a physical phase and a statistical phase. Therefore, we first quantify the contributions of physical changes and statistical properties of pixels on multi-looked phase and coherence and then assess the extent of their influences on closure triplet. Specifically, we answer the question: does the non-zero phase triplet demonstrates statistical characteristics of multi-looked window or does it instead possess information about phase changes corresponding to absolute physical changes, *i.e.* deforming and non-deforming processes such as soil moisture changes. This is of great importance because if the former statement is true, closure phase cannot be used as a proxy for estimating physical changes in the pixels.

This paper is structured as follows: Section II analyzes multi-looked phase, coherence, and closure phase; Section III includes the multi-looked interferometric phase generated from synthetic data and presents the results of interferometric phase and coherence along with phase triplet. Section IV provides results generated using real SAR data and a discussion of the results; and finally, conclusions appear in Section V.

4.2 Methods

4.2.1 Multi-looked Interferometric Phase

Let $u_1 = [u_1^1, u_1^2, \dots, u_1^n]'$ and $u_2 = [u_2^1, u_2^2, \dots, u_2^n]'$ to be master and slave SAR images each containing *n* pixels. Every pixel on each image is a random speckled quantity and can be written as the product of the unspeckled physical quantity s_i^k and the independent speckle random process n_i^k (Just and Bamler, 1994; Anxi et al., 2014; Lopes et al., 1992)

$$u_i^k = s_i^k . n_i^k \tag{4.1}$$

where k is the pixel position. Note that, throughout the paper, superscripted parenthesized numbers indicate pixel numbers, subscripted numbers show image numbers, and subscripted letters indicate the association. Also, bold letters represent vectors.

The noise vector is a zero-mean value complex Gaussian random vector with the phase that is uniformly distributed over [-π, π] (Lopes et al., 1992; Bamler and Just, 1993; Tough et al., 1994; Lee et al., 1994a; Lee et al., 1994b). For the two images, n_1 and n_2 are statistically independent of each other and of $s_1$and s_2 (Just and Bamler, 1994). Therefore, u_1 and u_2 are zero-mean random complex variables. Hence, the coherence of two complex SAR images u_1 and u_2, is defined as follows (Lopes et al., 1992; Bamler and Just, 1993; Tough et al., 1994)

$$\gamma = \frac{E[u_1 u_2^*]}{\sqrt{E[|u_1|^2]E[|u_2|^2]}} = |\gamma| e^{i\varphi_0} \tag{4.2}$$

where φ_0 is the expected noise-free phase, u_2^* is the complex conjugate of the second image, and E[.] denotes the expectation value that in practice will be approximated with a sampled average (Just and Bamler, 1994; Anxi et al., 2014; Lopes et al., 1992). Hence, over statistically uniform areas, the sampled coherence can be computed as (Bamler and Just, 1993; Tough et al., 1994; Lee et al., 1994a; Lee et al., 1994b)

$$\hat{\gamma} = \frac{\sum_1^n u_1 u_2^*}{\sqrt{\sum_1^n |u_1|^2 \sum_1^n |u_2|^2}} = |\hat{\gamma}| e^{j(\varphi_0 + \varphi_n)} = |\hat{\gamma}| e^{i\varphi} \tag{4.3}$$

where $|\hat{\gamma}|$ and φ are the magnitude and phase of the multi-looked interferogram. The joint probability density function (PDF) of magnitude and phase of an interferogram depends on the number of looks and satisfies Wishart distribution. The marginal PDF of InSAR phase can be derived from the joint PDF (Just and Bamler, 1994; Lee et al., 1994a; Lee et al., 1994b; Davenport and Root, 1987; Bamler and Hartl, 1998; Tough et al., 1995) that is characterized with a mean of φ_0 and a variance, which is a function of InSAR coherence value |γ | (Bamler and Hartl, 1998; Tough et al., 1995). Thus we have

$$\varphi = \varphi_0 + \varphi_n \text{ with } E[\varphi] = \varphi_0 \tag{4.4}$$

where φ_n denotes a zero-mean additive noise, upon which its variance is independent of the magnitude φ (Bamler and Hartl, 1998). The expected value of interferometric phase is φ_0 regardless of the magnitude of changes, number of looks and the value of complex correlation coefficient (Lopes et al., 1992; Bamler and Just, 1993; Tough et al., 1994; Lee et al., 1994a; Lee et al., 1994b; Davenport and Root, 1987; Bamler and Hartl, 1998).

4.2.2 The Influence of Intensity and Phase Changes of Single-looked Pixels on Multi-looked Pixel's Phase

Some physical processes, *i.e.* deforming or non-deforming changes, can cause intensity changes as well as phase changes. Soil moisture and vegetation biomass changes, for instance, initiate dielectric constant changes that in turn cause intensity and phase changes (De Zan et al., 2015; Zwieback et al., 2016; Hoekstra, and A. Delaney, 1974; Hallikainen et al., 1985). This is to say that in addition to phase changes of the pixels that occur between two images taken at

different times, their intensities are also subject to change. Plus, the two variables may be correlated to some degree. Basically, the amplitude and phase of SAR images are statistically independent random variables (Bamler and Just, 1993; Tough et al., 1994; Lee et al., 1994a; Lee et al., 1994b; ; Davenport and Root, 1987; Bamler and Hartl, 1998; Tough et al., 1995; Oliver and Quegan, 1998). However, between two images that are used to generate an interferogram, the intensity of pixels and their phase changes may not be independent variables. Therefore, we quantify the contribution of the statistical characteristics of intensity changes within the multi-looking window, and the correlation between intensity and phase changes on the multi-looked phase and coherence. By considering $u = a\, e^{j(\boldsymbol{\theta}_1)}$ in (2), we can rewrite equation (4.2) as

$$\gamma = \frac{E[u_1 u_2^*]}{\sqrt{E[|u_1|^2]E[|u_2|^2]}} = \frac{E\left[\boldsymbol{I}_{1,2}\, e^{j(\boldsymbol{\theta}_{1,2})}\right]}{\sqrt{E[\boldsymbol{I}_1]E[\boldsymbol{I}_2]}}$$

$$= \frac{1}{\sqrt{E[\boldsymbol{I}_1]E[\boldsymbol{I}_2]}}\left(E\left[\boldsymbol{I}_{1,2}\right]E\left[\, e^{j(\boldsymbol{\theta}_{1,2})}\right] + cov\left(\boldsymbol{I}_{1,2},\, e^{j(\boldsymbol{\theta}_{1,2})}\right)\right) =$$

$$|\gamma_0|\, e^{j(\varphi_0)} + |\gamma_s|\, e^{j(\varphi_s)} \tag{4.5}$$

In the equations above $\boldsymbol{I}_{1,2} = \boldsymbol{a}_1.\boldsymbol{a}_2$ is the vector of the product of the amplitudes of the first and second images, and $\boldsymbol{\theta}_{1,2} = \boldsymbol{\theta}_1 - \boldsymbol{\theta}_2$ is the vector of their phase differences. The coherence vector γ is the vector summation of two vectors. The amplitudes of the vectors are $|\gamma_0|$ and $|\gamma_s|$ and their phases are φ_0 and φ_s. The angle of coherence can be written in terms of the expected phase φ_0

$$arg\{\gamma\} = \varphi_0 + \Delta\varphi_{cov} \tag{4.6}$$

where $\Delta\varphi_{cov}$ is the phase change due to the influence of $cov\left(\boldsymbol{I}_{1,2},\ e^{j(\boldsymbol{\theta}_{1,2})}\right)$ and can be calculated by using equation (4.5)

$$\Delta\varphi_{cov} = arg\{E[\boldsymbol{I}_{1,2}\ e^{j(\boldsymbol{\theta}_{1,2})}]\} - arg\{E[\ e^{j(\boldsymbol{\theta}_{1,2})}]\} \tag{4.7}$$

Similarly, the sampled coherence, *i.e.* interferogram, can be rewritten as

$$\hat{\gamma} = \frac{1}{\frac{1}{n}\sqrt{\sum_{k=1}^{n}\boldsymbol{I}_1^k\ \sum_{k=1}^{n}\boldsymbol{I}_2^k}}\left(\frac{1}{n^2}\left(\sum\nolimits_{k=1}^{n}\boldsymbol{I}_{1,2}^k\sum\nolimits_{k=1}^{n}e^{j(\boldsymbol{\theta}_{1,2}^k)}\right) + cov\left(\boldsymbol{I}_{1,2},\ e^{j(\boldsymbol{\theta}_{1,2})}\right)\right) =$$

$$|\hat{\gamma}_0|\ e^{j(\varphi_0')} + |\hat{\gamma}_s|\ e^{j(\varphi_s)} \tag{4.8}$$

where $\varphi_0' = \varphi_0 + \varphi_{n,0}$. Note that the superscripts indicate pixel numbers and subscripts show image numbers. The sampled coherence vector $\hat{\gamma}$ is the vector summation of two vectors with the angles of φ_0' and φ_s and the amplitudes of $|\hat{\gamma}_0|$ and $|\hat{\gamma}_s|$. φ_0' is dominated with the expected phase φ_0 plus a zero-mean random phase $\varphi_{n,0}$, which corresponds to the statistical properties of the phase changes within the multi-looking window. φ_s is however associated with statistical properties of the intensity and phase changes of the pixels. Similarly, the interferometric phase can be expressed as

$$\varphi = arg\{|\hat{\gamma}_0|\ e^{j(\varphi_0')} + |\hat{\gamma}_s|\ e^{j(\varphi_s)}\} = \varphi_0' + \Delta\varphi_{cov}$$

$$= \varphi_0 + \varphi_n + \Delta\varphi_{cov} \tag{4.9}$$

where $\Delta\varphi_{cov}$ is the phase change due to the influence of $cov\left(\boldsymbol{I}_{1,2},\ e^{j(\boldsymbol{\theta}_{1,2})}\right)$ on the interferogram's phase that can be calculated by using equation (4.9)

$$\Delta\varphi_{cov} = \ arg\left\{\sum_{k=1}^{n} \boldsymbol{I}_{1,2}\ e^{j(\boldsymbol{\theta}_{1,2}^{k})}\right\} - arg\left\{\sum_{k=1}^{n} e^{j(\boldsymbol{\theta}_{1,2}^{k})}\right\} \tag{4.10}$$

In this paper, φ_0' and $\Delta\varphi_{cov}$ are called, respectively, intensity-independent and intensity-dependent phases for simplicity. The intensity-independent phase represents the expected physical changes φ_0, *e.g.* deformation, soil moisture change, of single-looked pixels plus a zero-mean random phase φ_n, which is related to phase statistics within the multi-looking window. In other words, the intensity-independent phase is related to physical phase and statistical properties of single-looked pixels' phase. The intensity-dependent phase, on the other hand, is associated with the statistical properties of both phase and intensity of single-looked pixels (see equations (4.5-4.7)).

4.2.3 Coherence Changes Related to the Statistical Properties of Single-looked Pixels' Intensity and Phase

The coherence changes induced by $cov\left(\boldsymbol{I}_{1,2},\ e^{j(\boldsymbol{\theta}_{1,2})}\right)$ is calculated in equations (4.5) and (4.8). Considering the sampled coherence as

$$|\hat{\gamma}| = \left|\left|\hat{\gamma}_p\right| e^{j(\varphi_0')} + |\hat{\gamma}_s|\ e^{j(\varphi_s')}\right| \tag{4.11}$$

We can calculate the coherence changes that is induced by the statistical properties of the phase and intensity of pixels

$$\Delta|\hat{\gamma}_{cov}| = \left|\left|\hat{\gamma}_p\right| e^{j(\varphi_0')} + |\hat{\gamma}_s| e^{j(\varphi_s')}\right| - \left|\left|\hat{\gamma}_p\right| e^{j(\varphi_0')}\right| \tag{4.12}$$

where $\Delta|\hat{\gamma}_{cov}|$ is the coherence change induced by $cov\left(\boldsymbol{I}_{1,2},\ e^{j(\boldsymbol{\theta}_{1,2})}\right)$ and is called intensity-dependent coherence in this paper.

4.2.4 The Contribution of Statistical Properties of Single-looked Pixels' Intensity and Phase on Phase Closure

Three SAR images from the same orbital track taken at different times can be used to generate three multi-looked interferograms. Closure phase is the difference between the phase of the interferogram pairing the first and the last SAR images and the summation of the phases of the two intermediate interferograms. For multi-looked pixels with $cov\left(\boldsymbol{I}_{1,2},\ e^{j(\boldsymbol{\theta}_{1,2})}\right) = 0$, using equation (4.4), we can write

$$\ddot{\varphi} = \varphi_{0,1} + \varphi_{n,1} + \varphi_{0,2} + \varphi_{n,2} - \varphi_{0,3} - \varphi_{n,3} \tag{4.13}$$

where $\ddot{\varphi}$ is the closure phase. By considering $\varphi_{0,1} + \varphi_{0,2} - \varphi_{0,3} = 0$, we have

$$\ddot{\varphi} = \varphi_{n,1} + \varphi_{n,2} - \varphi_{n,3} = \ddot{\varphi}_n \tag{4.14}$$

It should be noted that the noise phases are zero-mean random variables that are related to the magnitude of the coherence, which is related to the standard deviation of phase changes of the pixels within the multi-looking window. Thus, we have

$$E[\ddot{\varphi}] = 0 \quad \text{and } \sigma_{\ddot{\varphi}} = \sqrt{\sigma_{\varphi_{n_1}}^2 + \sigma_{\varphi_{n_2}}^2 + \sigma_{\varphi_{n_3}}^2} \tag{4.15}$$

Likewise, the closure phase of a multi-looked pixel with $cov\left(\boldsymbol{I}_{1,2},\ e^{j(\boldsymbol{\theta}_{1,2})}\right) \neq 0$ can be stated as

$$\ddot{\varphi}' = \ddot{\varphi}_n + \Delta\ddot{\varphi}_{cov} \tag{4.16}$$

with the expected value and standard deviation of

$$E[\ddot{\varphi}] = \Delta\ddot{\varphi}_{cov} \quad \text{and } \sigma_{\ddot{\varphi}} = \sqrt{\sigma_{\sigma_{\ddot{\varphi}}}^2 + \sigma_{\Delta\ddot{\varphi}_{cov}}^2} \tag{4.17}$$

where $\Delta\ddot{\varphi}_{cov} = \Delta\varphi_{cov,1} + \Delta\varphi_{cov,2} - \Delta\varphi_{cov,3}$ is the contribution of intensity-dependent phase ($\Delta\varphi_{cov}$ in equation (4.9)) of the three interferograms to the closure phase. Comparing equations (4.14) and (4.16) we can see that over pixels with $cov\left(\boldsymbol{I}_{1,2},\ e^{j(\boldsymbol{\theta}_{1,2})}\right) = 0$, phase triplet is a function of phase distribution within the multi-looked window, *i.e.* φ_n, with the expected value

of zero. In other words, over pixels with intensity homogeneity, *i.e.* the intensity dispersion index $D_I = {\sigma_{\boldsymbol{I}_{1,2}}}/{\bar{I}_{1,2}} = 0$, the expected value of closure phase is zero. Yet, for the cases where $cov\left(\boldsymbol{I}_{1,2},\ e^{j(\boldsymbol{\theta}_{1,2})}\right) \neq 0$, it also contains contributions from statistical properties of intensity as well as phase, *i.e.* $\Delta\varphi'_{cov}$.

4.3 Semi-Synthetic Data

4.3.1 Semi-Synthetic Interferograms

The equations in the previous section calculate the influence of statistical properties of intensity and phase changes on interferometric phase and coherence and closure phase. Here we investigate their effect by exploiting semi-synthetic interferograms. The first image of the semi-interferograms is a real SAR image and the second image is synthetic data generated from the real data by applying a predefined intensity and phase changes compared to the first image. Imagine a patch on a SAR data containing *p.q=n* pixels, which is called image one $\boldsymbol{Z_1}$ here. Image two $\boldsymbol{Z_2}$ can be generated by adding a change vector $\Delta\boldsymbol{Z_{1,2}}$ to $\boldsymbol{Z_1}$ as

$$\boldsymbol{Z_2} = \Delta\boldsymbol{Z_{1,2}} + \boldsymbol{Z_1} \tag{4.18}$$

where

$$\Delta\boldsymbol{Z_{1,2}} = \left[\Delta Z_{1,2}^{(1)}, \Delta Z_{1,2}^{(2)}, \dots,\ \Delta Z_{1,2}^{(n)}\right]'. \tag{4.19}$$

Each element of the change vector is associated with an intensity ratio $\alpha_{1,2}^{(\mathrm{i})} = I_2^{(\mathrm{i})}/I_1^{(\mathrm{i})}$, and a phase change $\Delta\theta_{1,2}^{(\mathrm{i})} = \theta_2^{(\mathrm{i})} - \theta_1^{(\mathrm{i})}$ so that for *ith* pixels of image one and two we can write

$$Z_1^{(\mathrm{i})} = \sqrt{I_1^{(\mathrm{i})}}\exp(j\theta_1^{(\mathrm{i})})$$

$$Z_2^{(\mathrm{i})} = \sqrt{\alpha_{1,2}^{(\mathrm{i})} I_1^{(\mathrm{i})}}\exp\left(j\left(\theta_1^{(\mathrm{i})} + \Delta\theta_{1,2}^{(\mathrm{i})}\right)\right) \tag{4.20}$$

The intensity ratio and phase change vectors are random variables

$$\boldsymbol{\alpha} = \bar{\alpha} + \boldsymbol{n_\alpha} \text{ and}$$

$$\Delta\boldsymbol{\theta} = \overline{\Delta\theta} + \boldsymbol{n_{\Delta\theta}} \tag{4.21}$$

where $\bar{\alpha}$ and $\overline{\Delta\theta}$ are the average intensity ratio and phase change and $\boldsymbol{n_\alpha}$ and $\boldsymbol{n_{\Delta\theta}}$ are zero-mean random variable vectors. The intensity and phase of SAR images have exponential and uniform distributions, respectively (Lee et al., 1994b; Davenport and Root, 1987; Oliver and Quegan, 1998). Therefore, by applying random vectors of intensity ratio and phase changes, the distribution properties of a real SAR image's intensity and phase will be preserved in the synthetic image $\boldsymbol{Z_2}$.

This allows to generate an interferogram between the two images that have pre-defined phase and intensity differences represented as random variable vectors. Figure 4.1 shows a series

of histograms of interferometric phases. Each of the histograms was generated from 200,000 such semi-synthetic interferograms. The first image of the semi-synthetic interferograms is a patch of real SAR data including L-band ALOS PALSAR, ALOS-2 PALSAR-2, and C-band Sentinel-1. The size of the patch for ALOS PALSAR and ALOS-2 PALSAR-2 images is 14 by 7 pixels in azimuth and range, respectively. For Sentinel-1 images, it is 20 by 4 pixels in azimuth and range, respectively. For each interferogram, the second image was generated by applying random intensity and phase changes to the pixels of the first image.

The first cluster of interferograms ('Cluster 1', blue histograms in figure 4.1) was generated by considering intensity homogeneity of the images. This means the amplitude of all pixels on every pair of images are considered to be one. Therefore, only the vector of phase changes was used. This cluster of interferograms represents phase changes over an ideal homogenous pixel (intensity homogeneity). The average and standard deviation of phase change are +1.25 and 1.0 radians, respectively. Figure 4.1 (blue) illustrates the probability density function (pdf) of interferometric phases of cluster one. It should be noted that we used images from over a wide variety of land cover types with different multi-looking numbers and different magnitudes of intensity and phase changes. However, we only show results from over three regions: Delta Junction, Alaska, Idaho, and New Mexico, where the multi-looked pixel patches were selected over forest, sparsely vegetated soil, and agricultural fields, respectively. As shown in figure 4.1 and in general, the interferometric phase values φ center at φ_0 (see equations (4.2) and (4.4)) regardless of the wavelength and polarization of data, magnitude of the changes, and land cover type.

The second cluster of interferograms represents interferometric phase changes over a non-homogeneous pixel where both intensity and phase changed. For this cluster, we used the

same phase change vectors applied to generate the first cluster. The intensity of the second image was, however, generated by applying an average and standard deviation of changes of +4 dB and 3 dB to the intensity of the first image.

As discussed previously, some natural processes such as soil moisture and vegetation biomass changes may induce correlated phase and intensity changes. Next, we investigated the effect of correlated intensity and phase changes on interferometric phase and coherence. To do this, the third cluster of interferograms were generated by applying the same changes in intensity and phase applied to generate the second cluster. However, they differ in their correlation coefficients between intensity and phase changes, which are 0.0 and 0.75 for the second and third clusters, respectively. The third cluster of interferometric phase values center at $\Delta\varphi_{cov}$ (see equations (4.9) and (4.10)), which is the phase shift due to the influence of $cov\left(\boldsymbol{I}_{1,2},\ e^{j(\boldsymbol{\theta}_{1,2})}\right)$ on the interferogram's phase. The coherence of the third cluster is also greater than the second one (see equations (4.11) and (4.12)).

Figure 4.1 shows that for each cluster of interferograms, all three histograms over different land cover type center at the same angle. It can be seen that the coherence of interferograms, however, differ depending on the polarization combination, wavelength, land cover type, homogeneity of pixels, and the covariance between intensity and phase changes. Note that the height of a histogram is a measure of its coherence. In other words, coherent interferograms have thinner histograms due to noise reduction.

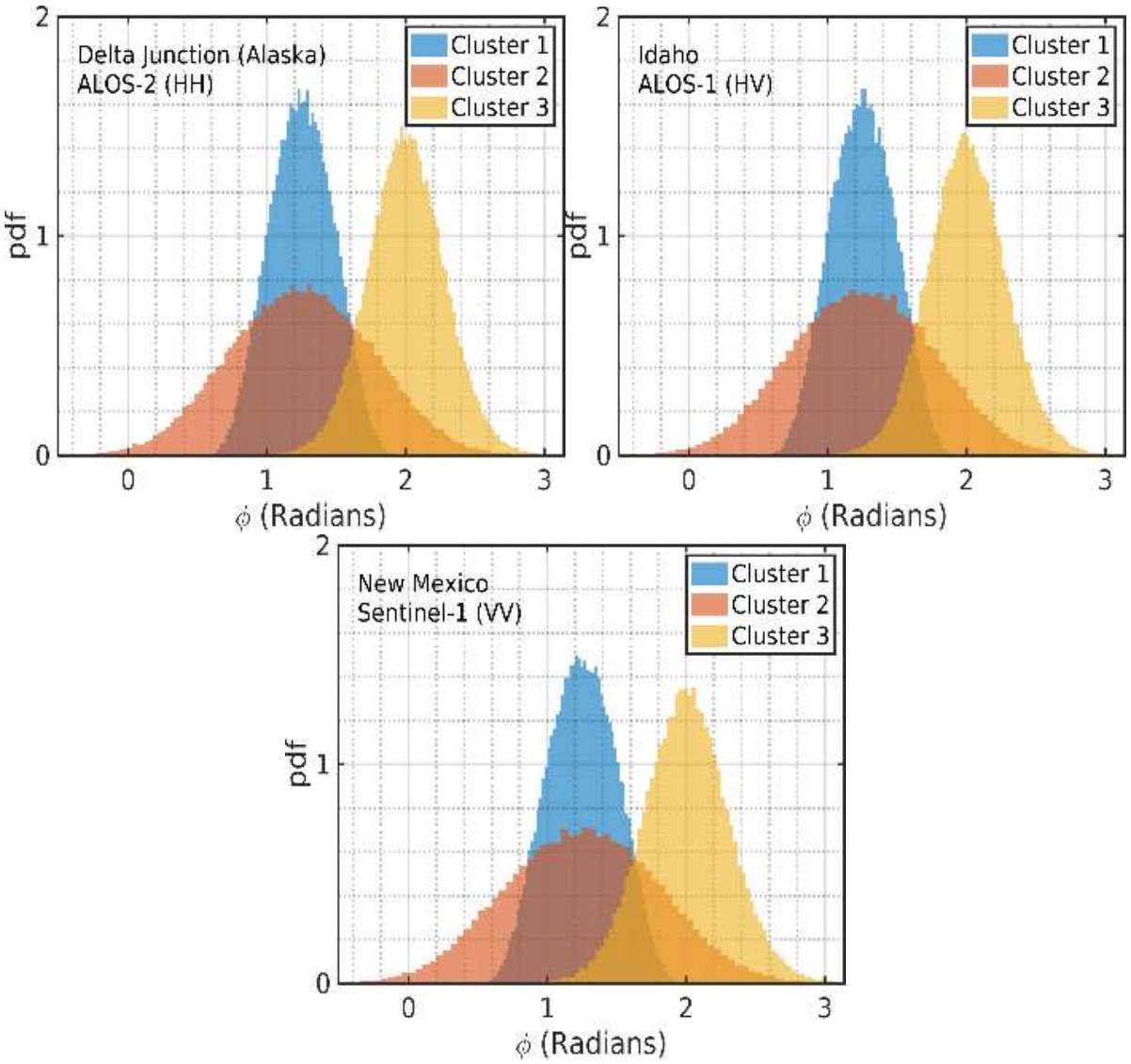

Figure 4.1. Probability density function of interferometric phases over Delta Junction, Alaska (forest), Idaho (sparsely vegetated soil), and New Mexico (agricultural field). Cluster 1 has phase changes with no intensity changes. Cluster 2 has changes over non-homogeneous pixels where both intensity and phase changed. Like Cluster 2, Cluster 3 also has changes over non-homogeneous pixels, but Cluster 3 has a correlation coefficient between intensity and phase change of 0.75 (vs. 0.0 for Cluster 2).

4.3.2 Closure Phase of Semi-Synthetic Interferograms

Synthetic data were also used to investigate the influence of statistical properties of pixels on closure phase. To do this, two categories of closure phases were generated, *i.e.* closure phases

of interferograms with independent intensity and phase changes (Cluster 2), and closure phases of interferograms with correlated intensity and phase changes (Cluster 3). For each category, three types of closure phases were generated so that we have six types of closure phases in total, which are 2-a, 2-b, 2-c, 3-a. 3-b, and 3-c). For 2-a and 3-a types, the average phase changes of +1.0, +0.5, and -1.5 have been applied to generate three interferograms of a closure phase. For 2-b and 3-b types, half of the phase changes (+0.5, +0.25, and -0.75) is applied to generate three interferograms. For 2-c and 3-c types, zero phase changes were applied to generate the interferograms. Figure 4.2 shows the histogram of closure phase for the second and third cluster of interferograms (see figure 4.1). Note that each interferogram histogram is generated from 200,000 semi-synthetic interferograms.

It can be seen that the histogram of closure phase corresponding to the second cluster centers at zero, which is suggested by equation (4.15). For the third cluster, however, the histograms centers at $\Delta\ddot{\varphi}_{cov}$ (see equation (4.17)). Note that the results for the first cluster of interferograms (not shown here) are similar to the results of the second cluster.

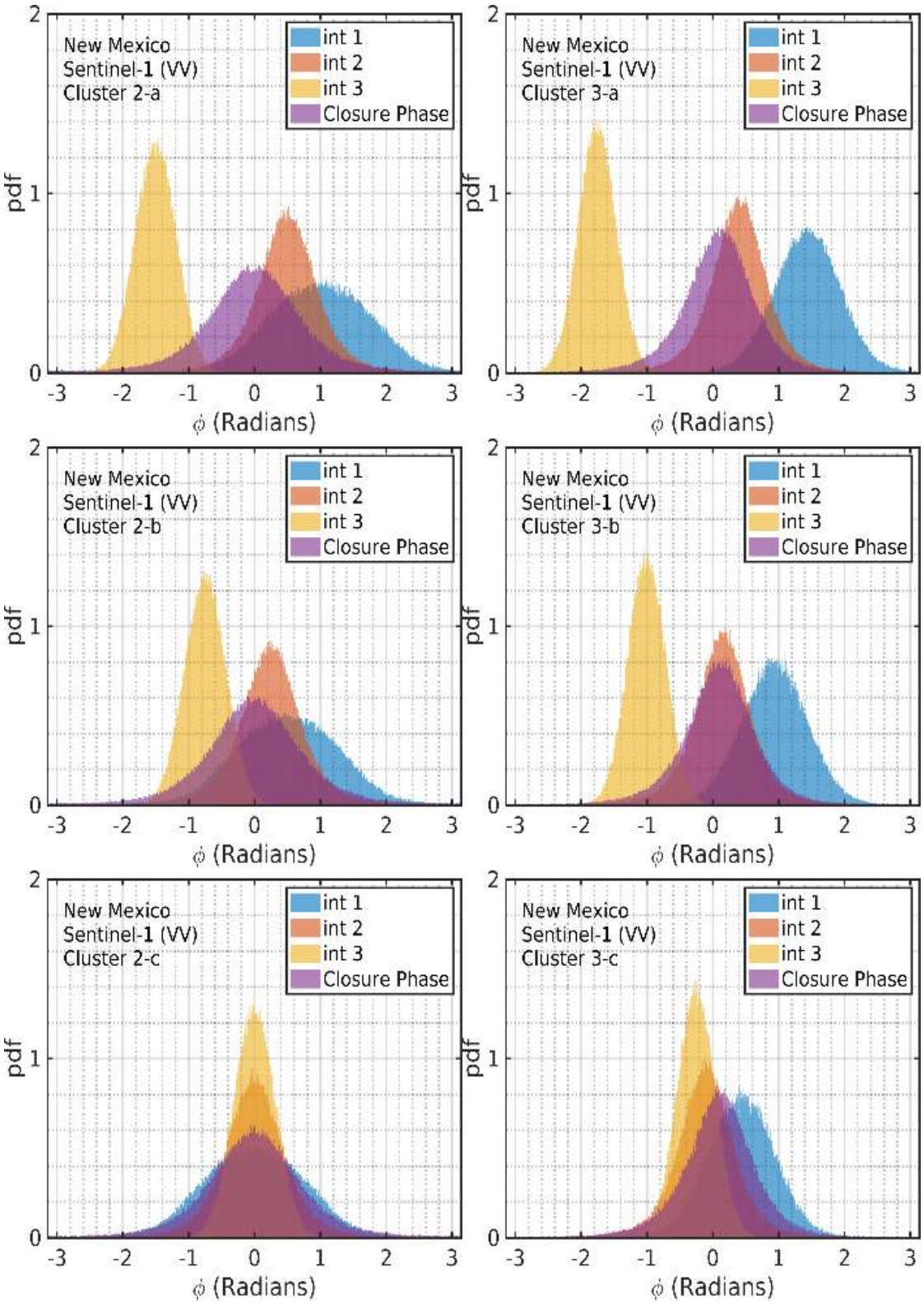

Figure 4.2. Probability density function of closure phase over New Mexico (sparsely vegetated soil). In the legend, int 1, int 2, and int 3, respectively, represent the histograms of the first, second, and third interferograms.

4.4 Real Data Interferograms and Discussion

4.4.1 Real Data Interferograms

Equation (4.9) shows that interferometric vector is a summation of two vectors, which are called intensity-independent and intensity-dependent components in this paper. One example of the intensity-independent and intensity-dependent vectors are illustrated in figure 4.3. In figure 4.3, the interferometric vector and its first and second components are illustrated in green, blue, and red, respectively. The angle of the first vector φ_0' is dominated by change in physical properties of the pixels, *i.e.* expected phase φ_0, plus a zero-mean random phase $\varphi_{0,n}$, which corresponds to the statistical properties of the phase changes within the multi-looking window. Therefore, its expected value is φ_0. The angle of the second vector φ_s, however, is associated with statistical properties of the intensity and phase changes of the pixels. It is a function of the dispersion index of intensity $D_I = {\sigma_{\boldsymbol{I}_{1,2}}}/{\bar{I}_{1,2}}$, the standard deviation of the phase changes $\sigma_{\,e^{j(\boldsymbol{\theta}_{1,2})}}$, and the correlation coefficient between $\boldsymbol{I}_{1,2}$ and $e^{j(\boldsymbol{\theta}_{1,2})}$

$$\frac{cov\left(\boldsymbol{I}_{1,2},\, e^{j(\boldsymbol{\theta}_{1,2})}\right)}{\frac{1}{n}\sqrt{\sum_{k=1}^{n}\boldsymbol{I}_1^k\ \sum_{k=1}^{n}\boldsymbol{I}_2^k}} = D_{\boldsymbol{I}}\ \sigma_{\,e^{j(\boldsymbol{\theta}_{1,2})}}\ cor\left(\boldsymbol{I}_{1,2},\, e^{j(\boldsymbol{\theta}_{1,2})}\right) \tag{4.22}$$

Its value is zero when either the dispersion index of intensity or the standard deviation of the phase changes is zero, *i.e.* over pixels with intensity or phase homogeneities. Also, its value becomes zero when $cor\left(\boldsymbol{I}_{1,2},\, e^{j(\boldsymbol{\theta}_{1,2})}\right) = 0$.

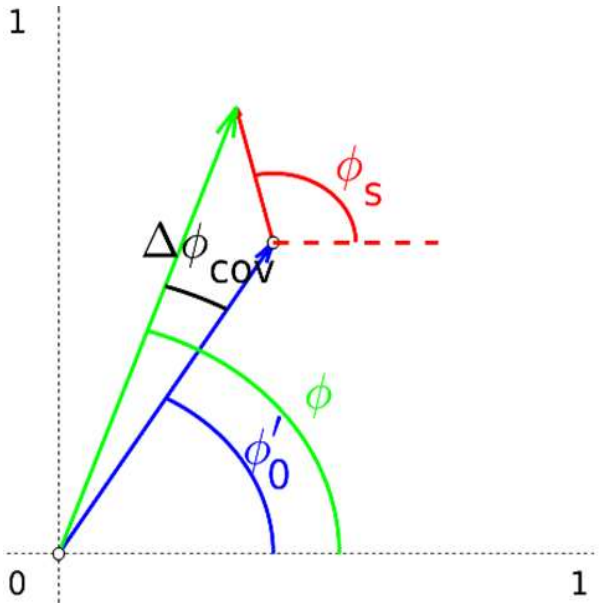

Figure 4.3. Interferometric (φ in equation (4.9)), intensity-independent (φ'_0 in equation (4.9)), and intensity-dependent ($\Delta\varphi_{cov}$ in equation (4.9)) vectors and phases. φ_s is the phase of $cor\left(\boldsymbol{I}_{1,2},\ e^{j(\boldsymbol{\theta}_{1,2})}\right)$ (see equation (4.10)).

Figure 4.3 also shows an interferometric phase φ in green. It can be seen that the interferometric phase is a scalar summation of intensity-independent φ'_0 and intensity-dependent $\Delta\varphi_{cov}$ phases. By comparing the two angles illustrated in figure 4.3, *i.e.* $arg\{E[\ e^{j(\boldsymbol{\theta}_{1,2})}]\}$ and $arg\{cor\left(\boldsymbol{I}_{1,2},\ e^{j(\boldsymbol{\theta}_{1,2})}\right)\}$ (see equation (4.10)), one can conclude that the difference between the two angles and consequently $\Delta\varphi_{cov}$ decrease by increasing homogeneity of $\boldsymbol{I}_{1,2}$. Figure 4.1 features examples of interferometric phase histogram generated from semi-synthetic interferograms. It illustrates intensity-dependent and intensity-independent phase contributions to the interferometric phase.

Figure 4.2 illustrates histogram of closure phases generated from semi-synthetic interferograms with different statistical properties of intensity and phase changes. It can be seen that the shapes of interferogram histograms and closure phase histograms don't change by

varying the magnitude of changes (compare the three histogram types of a, b, and c). This means that closure phase and interferometric coherence are independent of the magnitude of changes. Also, by comparing the histograms of Cluster 2 and Cluster 3, we can conclude that, when intensity and phase changes are independent (Cluster 2), the expected closure phase is zero. Unlikely, the expected closure phase becomes non-zero when intensity and phase changes are correlated (Cluster 3). These evaluations using synthetic data support our argument made in section II (see equations (4.13)-(4.17)).

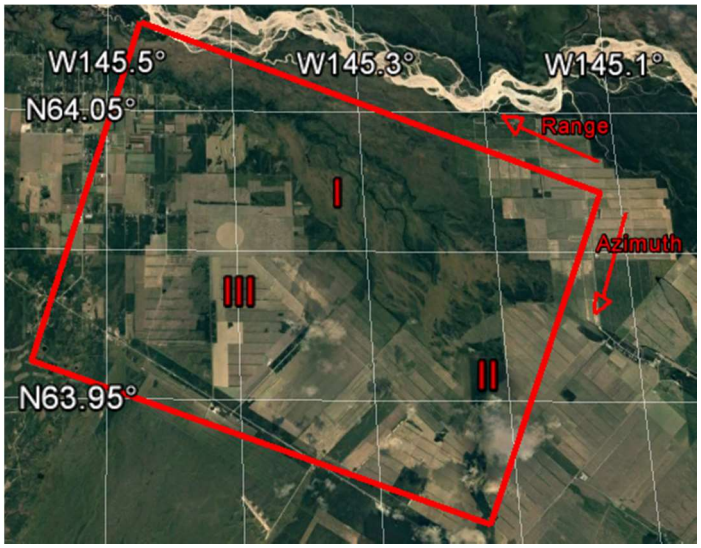

Figure 4.4. Study area in Delta Junction, Alaska (red box). The three major land cover types on the images are scarcely to moderately vegetated soil (area I), heavily vegetated area - forest (area II), and agricultural field (area III).

Next, we use real data to show that closure phase correlates with land cover types and is highly correlated with coherence values. We generated intensity-dependent ($\Delta\varphi_{cov}$ in equation (4.9)) and intensity-independent (φ_0' in equation (4.9)) phase images exploiting real SAR data. Using two images of ALOS-2 PALSAR-2 over Delta Junction (Alaska) taken on March 22, 2015 and March 6, 2016, we generated intensity-independent and intensity-dependent phases

quantified in equations (4.9) and (4.10). Figure 4.4 shows the study area. The three major land cover types on the images are scarcely to moderately vegetated soil (area I), forest (area II), and agricultural field (area III). The results are illustrated in figure 4.5. It can be seen that the intensity-independent phase (figure 4.5 (a)) correlates with land cover type. This is because different land cover types experience different physical processes between the two images. Unlike intensity-independent phase (φ_0' in equation (4.9)), the intensity-dependent phase ($\Delta\varphi_{cov}$ in equation (4.9)) (figure 4.5 (b)) is rather noisy. Its absolute value (figure 4.5 (c)), however, correlates with land cover type to some extent. Small intensity-dependent phase values correspond to homogenous areas where the coherence is higher and the larger values are associated with low-coherence areas (see figure 4.6 for comparison). This is because both coherence and $cov\left(\boldsymbol{I}_{1,2},\ e^{j(\boldsymbol{\theta}_{1,2})}\right)$ increase by increasing the standard deviations of intensity and phase changes. Figure 4.5 shows that the intensity-dependent phase does not possess information about physical changes but rather is a proxy to estimate the homogeneity of pixels.

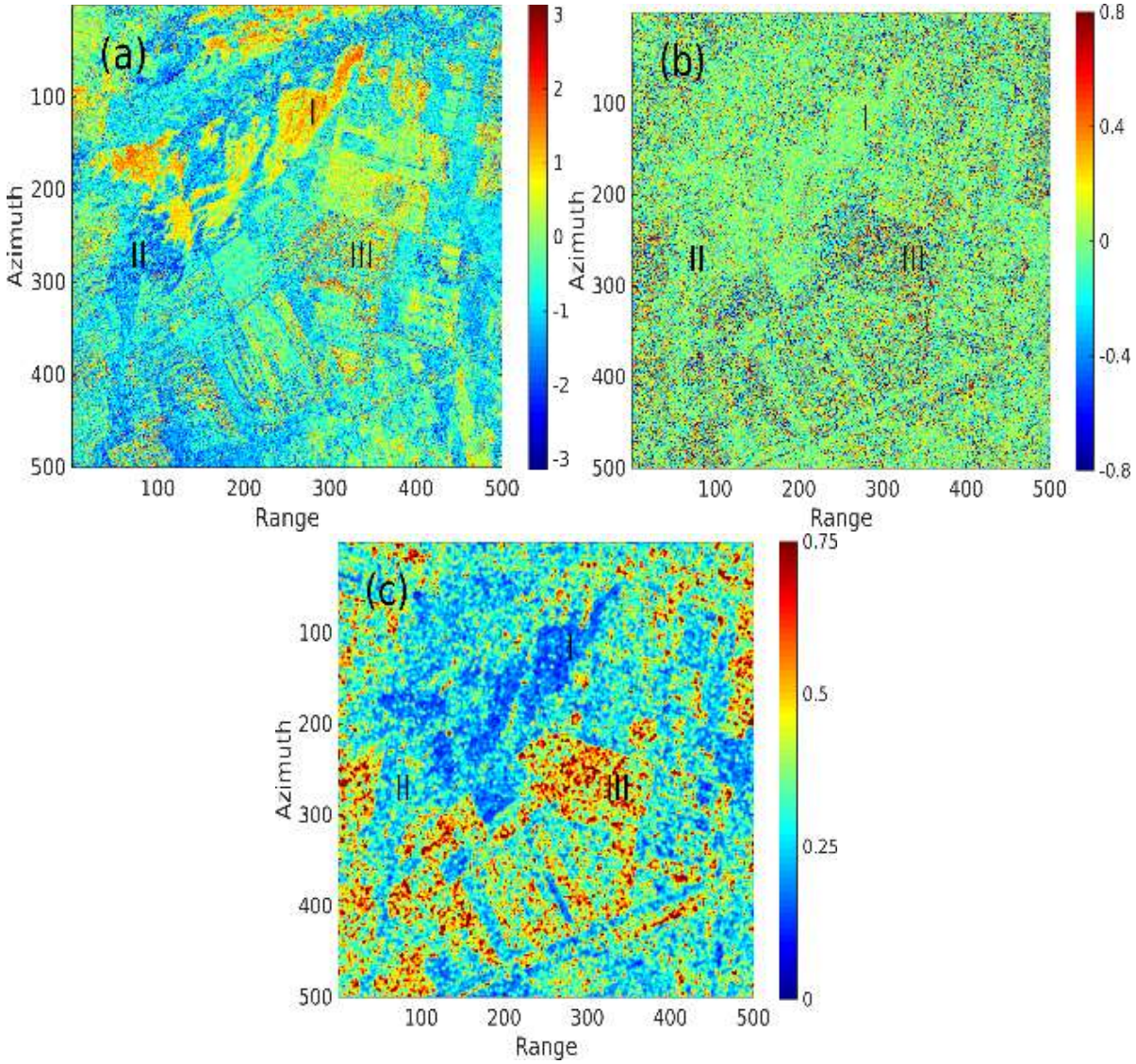

Figure 4.5. a) Intensity-independent phase (φ_0' in equation (4.9)), b) intensity-dependent phase ($\Delta\varphi_{cov}$ in equation (4.9)), and c) absolute intensity-dependent phase generated using ALOS-2 PALSAR_2 data over Delta Junction (Alaska).

In addition to phase contribution of statistical properties of pixels, changes in multi-looked coherence are also expected based on equation (4.12) and is shown in the phase histogram in figure 4.1. Figure 4.6 shows the interferometric coherence (6a), intensity-independent coherence (6b), and intensity-dependent coherence ($\Delta|\hat{\gamma}_{\mathrm{cov}}|$ *in* equation (4.12)) (6c), *i.e.* the difference between the two coherence values. Also in figure 4.3, the length of vectors

represent the magnitude of coherence values. The intensity-independent coherence (6b) is represented by the length of blue vector in figure 4.3. It is related to the phase statistics of single looked pixels and independent of intensity statistics. The interferometric coherence (6a), on the other hand, is dependent on phase and intensity statistics. The intensity-dependent coherence ($\Delta|\hat{\gamma}_{cov}|$ in equation (4.12))) is the length difference between green and blue vectors. In figure 4.3, it can be seen that the magnitude of interferometric coherence (the length of the green vector) increases by decreasing the difference between the phase of the statistical vector (red vector) and the phase of the intensity-independent vector (blue vector). The average intensity-dependent coherence of 0.1 can be seen on the image with lower amount on low-coherence pixels and higher values over homogenous areas.

Figure 4.7 shows closure phase images generated using three images of ALOS-2 PALSAR-2 over Delta Junction (Alaska) taken on March 08, 2015, March 22, 2015 and March 6, 2016. As shown in equation (4.16), closure phase is a function of noise and statistical phases, *i.e.* $\ddot{\varphi}_n + \Delta\ddot{\varphi}_{cov}$. Figure 4.7(a) illustrates the phase triplet of $\ddot{\varphi}_n$ whereas, figure 4.7(b) illustrates the phase triplet of $\Delta\ddot{\varphi}_{cov}$. $\ddot{\varphi}_n$ is a function of standard deviation of phase changes and its probability increases with a decreasing in coherence. This means that high $\Delta\varphi_n$ values correlate with low coherence values as seen in figure 4.6 and figure 4.7(c). Figure 4.7(d) shows that the absolute value of $\Delta\ddot{\varphi}_{cov}$ is also correlated with low coherence values. Therefore, we expect $\ddot{\varphi}_n$ and $\Delta\ddot{\varphi}_{cov}$ to be correlated with each other and inversely with coherence, as in figure 4.6 and figure 4.7.

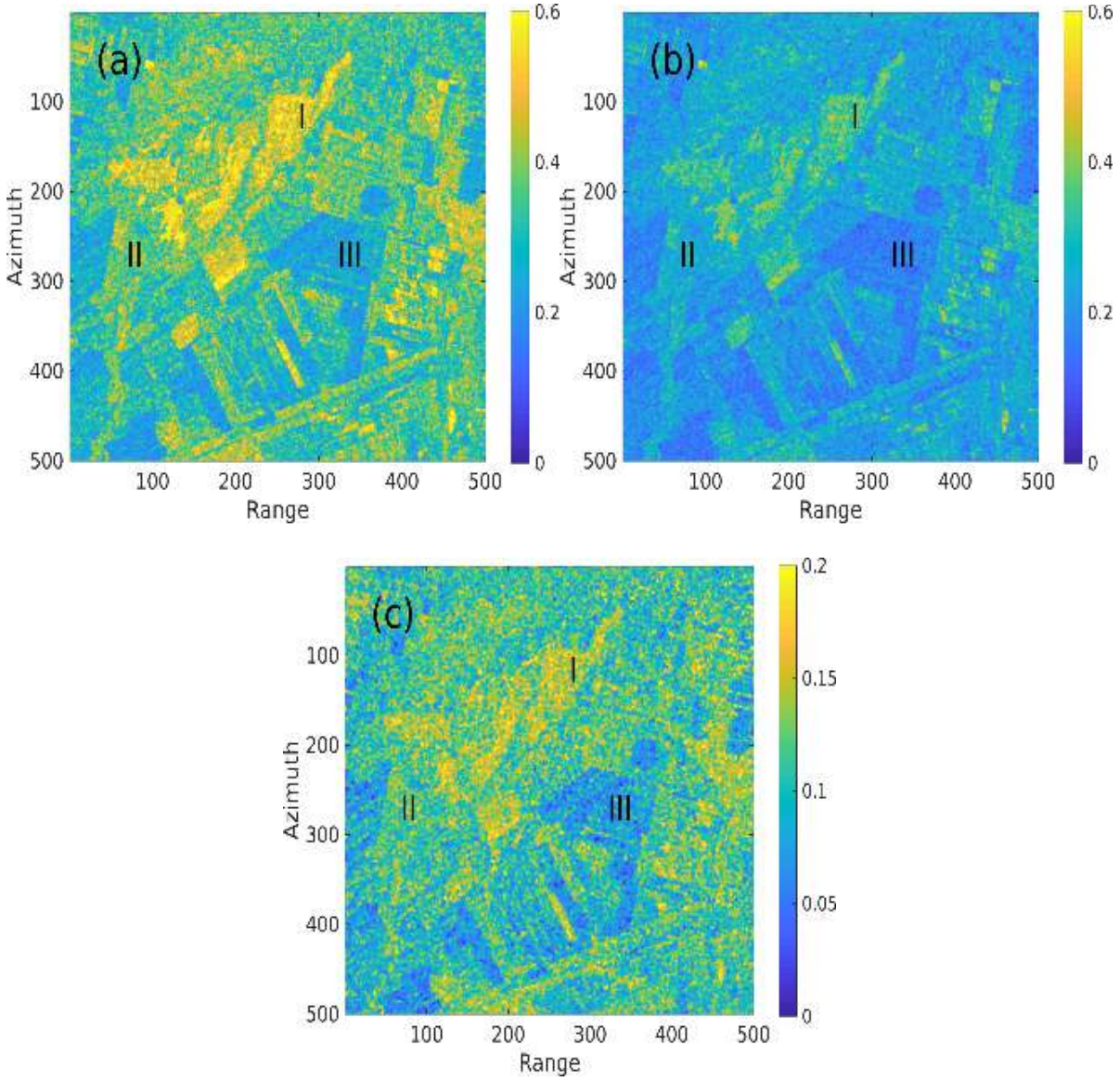

Figure 4.6. a) Interferometric coherence, b) intensity-independent coherence ($|\hat{\gamma}_p|$ in equation (4.11)), and c) the difference between interferometric and intensity-independent coherences (intensity-dependent coherence ($\Delta|\hat{\gamma}_{cov}|$ in equation (4.12))). The three major land cover types on the images are scarcely to moderately vegetated soil (area I), heavily vegetated area, forest (area II), and agricultural field (area III).

The mathematical analyses and the results of synthetic data show that none of the phase triplet components is directly related to the magnitude of phase or intensity changes. Rather, they are functions of statistical properties. Also, our real data results show that absolute closure phase

values correlate with coherence values. This fact makes the closure phase less appropriate for soil moisture change estimation.

4.4.2 Soil Moisture Estimation Using InSAR Phase and Closure Phase

As stated previously, in addition to deformation mapping, interferometric phase has been also used to estimate soil moisture changes (De Zan et al., 2015; Zwieback et al., 2016). The change in soil moisture will induce a change in dielectric constant that in turn leads to phase increase, which is manifested as subsidence on interferograms (Hensley et al., 2011; Ferretti, et al., 2011). However, the phase of interferograms generated from single-looked pixels are rather noisy due to strong effects of decorrelations and noises. Therefore, we prefer multi-looked pixel. Multi-looking reduces the noise and improves the reliability of phase unwrapping by averaging adjacent pixels in the complex interferogram (Hensley et al., 2011; Ferretti, et al., 2011). In practice, multi-looking process makes strong pixels contribute more to interferometric phase. This is desired for deformation mapping purposes because the effect of weak pixels is cancelled out to some extent. This leads to increased effect of the strong pixels and lower uncertainties in phase estimation.

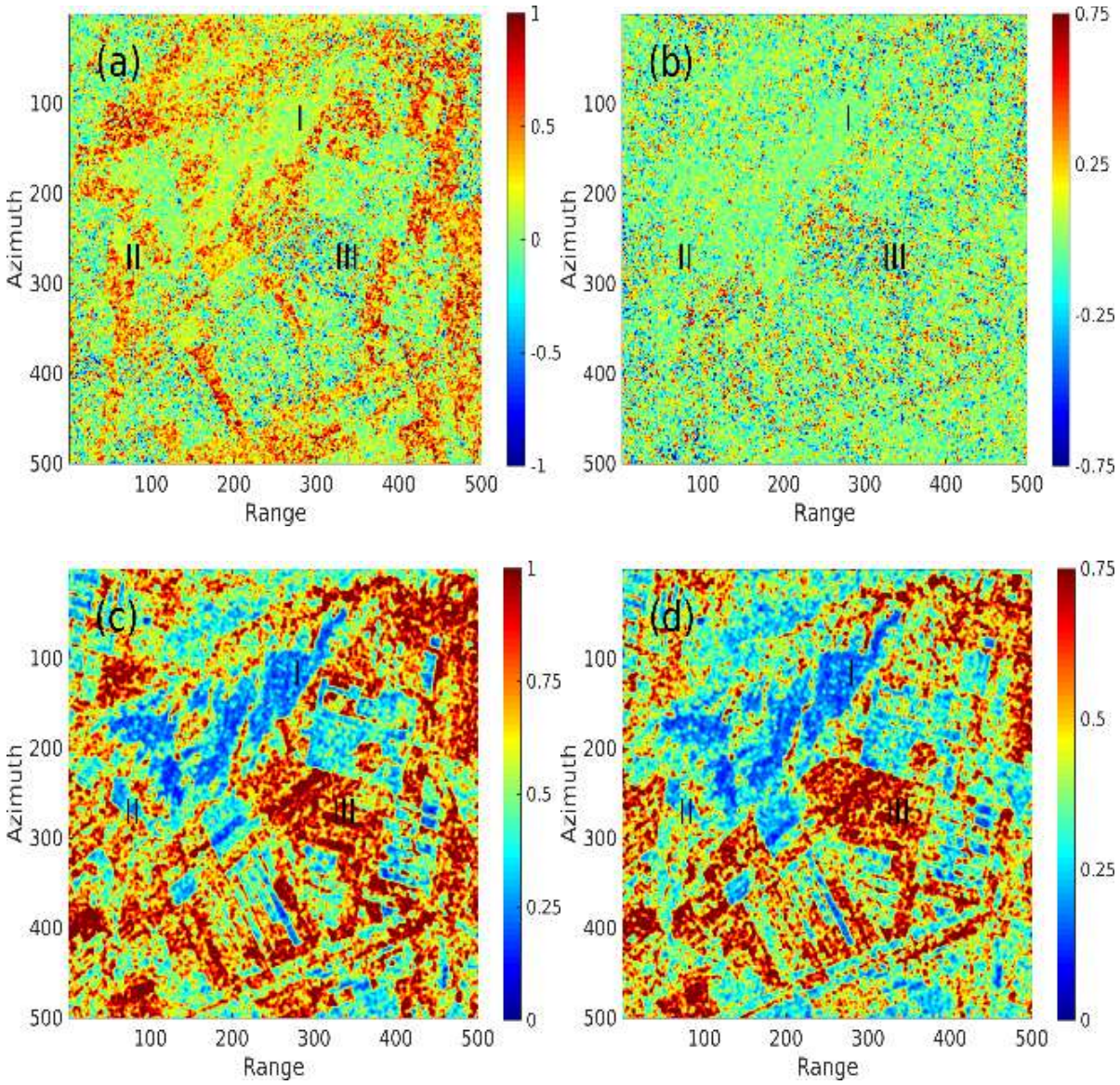

Figure 4.7. a)The closure phase of $\ddot{\varphi}_n$, b) the closure phase of $\Delta\ddot{\varphi}_{cov}$, c) the absolute closure phase of $\ddot{\varphi}_n$, and d) the absolute closure phase of $\Delta\ddot{\varphi}_{cov}$ generated using ALOS-2 PALSAR_2 data over Delta Junction (Alaska).

For many cases, pixels are covered by natural materials such as soil and vegetation layer. In these cases, the change in the physical properties of pixels such as soil moisture and vegetation biomass changes will cause intensity changes as well as phase changes. In this paper we showed that intensity changes can contribute to phase and coherence changes of multi-looked

pixels. The effect of the statistical properties of intensity on multi-looked phase and coherence (equation (4.10)) are called intensity-dependent phase and coherence, respectively, in this paper. The intensity-independent component of the multi-looked interferometric phase is dominated by the change in physical properties of the pixels plus a zero-mean random phase related to phase statistics within the multi-looking window. The intensity-dependent phase is only associated with statistical properties of the intensity and phase changes in the multi-looking window. The intensity-dependent phase is rather small over homogeneous pixels but its magnitude increases over heterogeneous areas such as pixels over vegetation layer. Therefore, understanding the contribution of intensity-dependent phase on InSAR phase, we suggest that care should be taken when multi-looked phase is used to estimate absolute physical changes, especially over non-homogeneous pixels.

Multi-looking also leads to non-zero closure phase. It has been argued in the literature that closure phase has the potential to be used as a proxy to estimate soil moisture changes. We showed that closure phase is a function of phase and intensity statistical properties and similar to InSAR coherence, it contains no information about the magnitude of physical changes. It can be used for soil moisture estimation only when a strong correlation between absolute soil moisture changes and its standard deviation can be found.

4.5 Conclusion

The magnitude and the standard deviation of phase changes associated with physical changes contribute to multi-looked phase changes. InSAR coherence is relate to the standard deviation of phase changes in the multi-looking window. In this paper, we showed that the statistical properties of the intensity of pixels contributes to phase and coherence of multi-looked pixels. The influence of intensity increases by increasing the standard deviation of phase

changes, dispersion index of intensity, and the correlation between intensity and phase changes. This paper demonstrated that non-zero closure phase originates from statistical properties of phase and intensity of the pixels within the multi-looking window.

We showed that phase closure is associated with the standard deviation of phase changes and dispersion index of intensity and does not relate to the magnitude of physical, deforming and non-deforming changes. Therefore, this casts doubt on the effectiveness of using phase triplet as a means to estimate soil moisture changes or any changes corresponding to dielectric changes.

Semi-synthetic interferograms are used to support the findings of this paper. Semi-synthetic interferograms pair a real image and a synthetic SAR image, which is generated from the real SAR image by applying random changes in intensity and phase with defined magnitude of changes. We also used real SAR images to generate interferograms over different land cover types. The histogram of generated semi-synthetic interferograms accord with the findings of the paper.

Acknowledgment: The work was funded by the NASA Earth Surface & Interior Program (80NSSC19K1491 and NNX16AK56G) and the Shuler-Foscue Endowment at Southern Methodist University.

References

Massonnet, D., and K. Feigl. 1998. Radar interferometry and its application to changes in the Earth's surface, *Rev. Geophys.,* 36, 441-500.

Lu, Z., and D. Dzurisin. 2014. InSAR Imaging of Aleutian Volcanoes: Monitoring a Volcanic arc from Space, Geophysical Sciences, Springer Praxis Books, Springer: Chichester, UK, 2014, p. 390.

Shirzaei, M., and R. Bürgmann. 2013. Time-dependent model of creep on the hayward fault from joint inversion of 18 years of insar and surface creep data. *J. Geophys. Res. Solid Earth*, 118, 1733–1746.

Molan, Y.E., J.-W. Kim, Z. Lu, and P. Agram. 2018a. L-Band Temporal Coherence Assessment and Modeling Using Amplitude and Snow Depth over Interior Alaska. *Remote Sens*. 10, 150.

Ferretti, A., C. Prati, and F. Rocca. 2001. Permanent scatterers in SAR interferometry. IEEE Transactions on Geoscience and Remote Sensing, 39, 8–20.

Molan, Y.E., J.-W. Kim, Z. Lu, B. Wylie, and Z. Zhu. 2018b. Modeling Wildfire-Induced Permafrost Deformation in an Alaskan Boreal Forest Using InSAR Observations. Remote Sens., 10, 405.

Rykhus, R., and Z. Lu. 2008. InSAR detects possible thaw settlement in the Alaskan Arctic Coastal Plain. *Can. J. Remote Sens*., 34, 100–112.

Agram, P.S., R. Jolivet, B. Riel, Y.N. Lin, M. Simons, E. Hetland, M.P. Doin, and C. Lasserrre. 2013. New Radar Interferometric Time Series Analysis Toolbox Released. *Eos Trans. Am. Geophys. Union*, 94, 69–70.

Fattahi, H., F. Amelung, E. Chaussard, and S. Wdowinski. 2015. Coseismic and postseismic deformation due to the 2007 M5. 5 Ghazaband fault earthquake Balochistan Pakistan. *Geophysical Research Letters*, vol. 42, no. 9, pp. 3305-3312.

De Zan, F., M. Zonno,and P. López-Dekker. 2015. Phase inconsistencies and multiple scattering in SAR interferometry. *IEEE Trans. Geosci. Remote Sens.*, 53, 6608–6616.

Zwieback, S., X. Liu, S. Antonova, B. Heim, A. Bartsch, J. Boike, and I. Hajnsek. 2016. A statistical test of phase closure to detect influences on DInSAR deformation estimates besides displacements and decorrelation noise: Two case studies in high-latitude regions. *IEEE Trans. Geosci. Remote Sens.*, vol. 54, no. 9, pp. 5588-5601.

Molan, Y.E., and Z. Lu. 2020a. Modeling InSAR Phase and SAR intensity Changes Induced by Soil Moisture, *IEEE TGRS*, DOI: 10.1109/TGRS.2020.2970841.

Nolan, M., D. R. Fatland, and L. Hinzman. 2003. DInsar measurement of soil moisture. IEEE Trans. Geosci. Remote Sens., vol. 41, no. 12, pp. 2802–2013.

Hensley, S., S., T. Michel, J. Van Zyl, R. Muellerschoen, B. Chapman, S. Oveisgharan, Z. S. Haddad, T. Jackson, and I. Mladenova. 2011. Effect of soil moisture on polarimetric-interferometric repeat pass observations by UAVSAR during 2010 Canadian Soil Moisture campaign. In Proc. *IEEE IGARSS*, pp. 1063–1066.

Ferretti, A., A. Fumagalli, F. Novali, C. Prati, F. Rocca, and A. Rucci. 2011. A new algorithm for processing interferometric data-stacks: SqueeSAR. *IEEE Transactions on Geoscience and Remote Sensing*, 49, 3460–3470. http://dx.doi.org/10.1109/TGRS.2011.2124465.

Goldstein, R.M., H.A. Zebker, and C.L. Werner. 1988. Satellite Radar Interferometric: Two-dimensional phase unwrapping. *Radio Sci.*, Vol.23, No.4, pp.713-720.

Fornaro, G., S. Verde, D. Reale, and A. Pauciullo. 2015. CAESAR: an approach based on covariance matrix decomposition to improve multibaseline-multitemporal interferometric SAR processing. *IEEE Trans. Geosci. Rem. Sens.,* 53 (4), pp. 2050-2065

Verde, S., D. Reale, A. Pauciullo, and G. Fornaro. 2018. Improved Small Baseline processing by means of CAESAR eigen-interferograms decomposition. *ISPRS Journal of Photogrammetry and Remote Sensing*, Volume 139, Pages 1-13, ISSN 0924-2716.

Just, D., and R. Bamler. 1994. Phase statistics of interferograms with applications to synthetic aperture radar. *Applied Optics*, 33(20), 4361-4368. doi: 10.1364/AO.33.004361

Anxi, Y., W. Haijun, D. Zhen, and H. Haifeng. 2014. Amplitude and Phase Statistics of Multi-look SAR Complex Interferogram. *Defense Science Journal*, Vol. 64, No. 6, pp. 564-570, DOI : 10.14429/dsj.64.4747

Lopes A. et al. 1992. Phase difference statistics related to sensor and forest parameters. In Proc. *Int. Geosci. Remote Sensing Symp*. (IGARSS'92) Houston, TX, pp. 779-781.

Bamler, R., and D. Just. 1993. Phase statistics and decorrelation in SAR interferograms. *IEEE Geosci.* Remote *Sens. Symp.*, 980-984. 15.

Tough, R. J. A., D. Blacknell, and S. Quegan. 1994. Estimators and distributions in single and multi-look polarimetric and interferometric data. *IEEE Geosci. Remote Sens. Symp.*, 4, 2176-2178. 17.

Lee, J. S., A. R. Miller, and K. W. Hoppel. 1994. Statistics of phase difference and product magnitude of multi-look processed Gaussian signals. *Waves in Random Media*, 4(3), 307-319. doi: 10.1088/0959-7174/4/3/006 18.

Lee, J. S., K. W. Hoppel, and S. A. Mango. 1994. Intensity and phase statistics of multi-look polarimetric and interferometric SAR imagery. *IEEE Trans. Geosci. Remote Sens.*, 32(5), 1017-1028. doi: 10.1109/36.312890

Davenport, Jr., W. B., and W. L. Root. 1987. An Introduction to the Theory of Random Signals and Noise. 1st ed. (Institute of Electrical and Electronics Engineers, New York), Chap. 8, pp. 158-165

Bamler, R., and P. Hartl. 1998. Synthetic Aperture Radar Interferometry. *Inverse Problems*, Vol. 14, R1.

Tough, R. J. A., D. Blacknell, and S. A. Quegan. 1995. Statistical description of polarimetric and interferometric synthetic aperture radar data. In *Proceedings of the Royal Society of London*. Series A: Mathematical and Physical Sciences, 449(1937), 567-589

Hoekstra, P. and A. Delaney. 1974. Dielectric properties of soils at UHF and microwave frequencies. *J. Geophys. Res.*, 79:1699-1708.

Hallikainen, M., F. Ulaby, M. Dobson, M. El-Rayes, and L.K. Wu. 1985. Microwave dielectric behavior of wet soil — Part 1: Empirical models and experimental observations. *IEEE Transactions on Geoscience and Remote Sensing,* 23, 25–34.

Oliver, C. J., and S. Quegan. 1998. Understanding Synthetic Aperture Images. Norwood, MA: Artech House.

CHAPTER 5

SOIL MOISTURE-INDUCED SAR INTENSITY AND INSAR PHASE CHANGES

Molan, Y.E., and Z. Lu. 2020. Modeling InSAR Phase and SAR intensity Changes Induced by Soil Moisture, *IEEE TGRS*, DOI: 10.1109/TGRS.2020.2970841.

5.1 Introduction

InSAR, which is an all-weather, day-or-night technique, has the ability to remotely sense mm to cm scale surface deformation with a high spatial resolution of tens of meters or better (Massonnet and Feigl, 1998; Bürgmann et al., 2000; Lu and Dzurisin, 2014). InSAR provides valuable input to studies of earthquakes, volcanos, landslides, permafrost processes, and so on (Lu and Dzurisin, 2014; Molan et al., 2018a; Ferretti et al., 2001). Two SAR images taken at different times are combined to make an interferogram to detect ground surface deformations as well as to generate DEMs (Massonnet and Feigl, 1998; Bürgmann et al., 2000; Lu and Dzurisin, 2014). Between the two images, the water content of the soil being imaged is subject to change. The temporal change in soil moisture has been known to contribute to InSAR phase and SAR intensity changes (Lu and Meyer, 2002; Nolan et al., 2003; Barrett et al., 2012; Zwieback et al., 2015a; De Zan et al., 2014). Consequently, InSAR detected ground displacement can be systematically biased by the changes in soil moisture. The uncompensated

biases in the spatial and temporal patterns of InSAR detected displacement limits the reliability and robustness of InSAR (Lu and Meyer, 2002; Nolan et al., 2003; Barrett et al., 2012; Zwieback et al., 2015a; De Zan et al., 2014).

Unlike ground deformations, which are spatially and temporally correlated, the spatial and temporal variabilities of soil moisture are complex (Hensley et al.., 2011) and, in practice, the influence on InSAR phases can be confused with atmosphere artifacts. Some atmospheric artifacts can be compensated by utilizing spatial-temporal filters (Hensley et al.., 2011; Hooper et al., 2012) since they often feature spatially-correlated variations (Hanssen, 2001). Unlikely, soil moisture is not always correlated spatially as its value varies abruptly, for example, across boundaries of two agricultural fields or different land cover types (Hensley et al.., 2011; Hooper et al., 2012; Hanssen, 2001; Gabriel et al., 1989). Soil moisture's temporal variability is also intricate (Hensley et al.., 2011; Hooper et al., 2012; Hanssen, 2001; Gabriel et al., 1989). Therefore, temporal filters may not be as practical as it is to mitigate turbulent tropospheric phase artifacts, which are temporally uncorrelated on time scale of days (Hanssen, 2001). Also, in some cases, terrestrial processes and subsequent movements are closely related to the changes in soil moisture. For example, sudden landslides can happen after rapid snow melt or heavy precipitation (Cardinali et al., 2000). Soil moisture also indicates groundwater conditions (Robinson and Campbell, 2008) and is in a close relationship with permafrost thawing and deformation (Molan et al., 2018a). Broadly speaking, soil moisture is a key variable in agricultural and environmental studies (Hirschi et al., 2006; Liang et al., 2014; Seneviratne et al., 2004), and plays a vital role in the terrestrial water cycle, exchange of energy and carbon fluxes between the atmosphere and the land surface (Liang et al., 2014; Seneviratne et al., 2004).

Potentially, modeling soil moisture influence on InSAR phase measurements and SAR intensity changes provides a means to compensate soil moisture induced InSAR phase artifacts and also to retrieve surface soil moisture. The first reported signal of soil moisture on InSAR images has been reported in 1989 (Gabriel et al., 1989). One of the interferograms over agricultural field in California, generated using SEASAT data, featured phase changes corresponded to field boundaries. The observed phase was inferred to be related to soil moisture. Swelling characteristic of the soil convinced the authors to ascribe the phase change to surface movement (expansion), *i.e.* shortening in the travel path of radar wave. Since then, soil moisture induced phase changes on interferograms from satellite SAR data (Nolan et al., 2003; Zhang et al., 2008; Barrett et al., 2012) and airborne and indoor experiments (Hajnsek and Prats, Nesti et al., 1995, 1998) have been continued to be reported.

New experimental studies later cast doubt on the expansion hypothesis. For instance, Rudant et al., 1996, in a laboratory experiment noted apparent subsidence over wetted soil and sprinkled planets. Hensley et al., 2011, and Morrison et al., 2011, also noticed that the phase change is larger than the deformation of the surface of the soil, indicating that the observed phase cannot be caused by a realistic deformation. Alternatively, the influence of soil moisture on InSAR phase has been attributed to soil volume scattering (Zwieback et al., 2015; De Zan et al., 2014). Zwieback et al., 2015, empirically analyzed the applicability of the aforementioned hypotheses. Using the data of two L-band airborne campaigns, the authors revealed that the soil moisture induced phase was not consistent with the penetration depth or the soil swelling hypotheses but only with dielectric volume scattering mechanism. Upon wetting, the dielectric constant of the soil and consequently the optical path between the antenna and the scatterers in the soil volume increase. As soil absorbs water, the replacement of air within free spaces of soil

by water increases the dielectric constant of the soil since the magnitude of the dielectric constant of water is much greater than that of air or sand grains. The increase in dielectric constant corresponds to an increase in the wavenumber in the soil, which gives rise to an increase in phase. This is manifested as a movement away from the antenna or an apparent subsidence of the surface, even with no mechanical deformation on the ground.

So far, a broad range of studies from controlled experiments to observational studies without soil moisture information have been conducted to quantify the effect of soil moisture on SAR intensity and InSAR phase and coherence (Molan et al., 2018a, 2018b; Lu and Meyer, 2002; De Zan et al., 2014; Gabriel et al., 1989; Nolan et al., 2003; Zhang et al., 2008; Barrett et al., 2012; Hajnsek and Prats, 2008; Nesti et al., 1995, 1998; Rudant et al., 1996; Hensley et al., 2011; Morrison et al., 2011). The models can be divided into interferometric and intensity models. On one hand, a number of interferometric models have provided mathematical volume scattering models ranging from simple analytical expression (e.g. Zwieback et al., 2015) to more complicated numerical solutions to Maxwell's equations to estimate soil moisture induced InSAR phase artifacts (e.g. De Zan et al., 2014). Basically, the models can potentially be used or modified for different soil types as well as layered and/or depth-resolved observations. Yet, what all the interferometric models share in common is that the temporal change in volume soil moisture has been purported to be the primary influential factor in the models. Hence, these interferometric models don't consider the influence of soil's structure, *i.e.* the size and distribution of scatterers, on InSAR phase changes. On the other hand, intensity models usually attribute soil moisture induced SAR intensity changes to surface scattering solely (Fung et al., 1992; Su et al., 2015; Baghdadi and Zribi, 2006; Altese et al., 1996; Barrett et al., 2009), and volume scattering is either neglected or employed along with surface scattering models to

provide an explanation for negative slope that appears on SAR intensity curves at small soil moisture values (Liu et al., 2016; Zwieback et al., 2017).

At the time of writing this manuscript, to the best of our knowledge, no volumetric soil moisture model has been introduced that takes into account soil volumetric structure and addresses both intensity and phase changes. In this paper, we present a new approach and a comprehensive model to estimate soil moisture induced SAR intensity and InSAR phase changes. To this end, we model the soil as a collection of discrete coarse scatterers, *i.e.* with a diameter of few centimeters or larger, embedded in an attenuating dielectric medium comprising of finer soil grains. Therefore, our volume scattering model can not only provide improved estimation of soil moisture induced intensity and phase changes but also potentially be used to infer soil structure. The rest of this paper is structured as follows: Section II describes the introduced volume scattering model; Section III includes simulated results; Section IV provides a discussion on the results and also mathematical analyses to support the outcomes; Section V provides validation of results; conclusions appear in Section VI.

5.2 Volume backscattering model

Here, we model the expected return signal from a pixel after SAR focus. Soil, the scattering object, is modeled as a half-space dielectric medium with N randomly distributed independent point scatterers in a resolution cell. When an electromagnetic wave strikes on the soil surface, a part of the incident wave reflects away, whereas a fraction of it transmits into the soil and decays exponentially at a rate governed by the imaginary part of the medium's complex wavenumber (Tsang et al., 2000; Ulaby et al., 1981; Mätzler, 1998). Also, as the wave propagates through the medium, its phase is manipulated by the real part of the medium's

complex wavenumber (Tsang et al., 2000; Ulaby et al., 1981; Mätzler, 1998). Once the wave is scattered by a point scatterer within the soil medium, a part of the scattered wave propagates backward. Through the backward propagation, the dielectric medium again modifies its amplitude and phase until it reaches the soil-air boundary. A part of the transmitted wave at the soil-air interface propagates back toward the antenna. Then, the signal is further modified by applying slant range and azimuth resolution functions, W_a and W_r, respectively. Finally, the scattered signal from a single scatterer located at (x_i, y_i, z_i) within the soil becomes

$$u_i = e^{-j2kR} t_{1,2}\, t_{2,1}\, s_i\, e^{\frac{-2\alpha z_i}{\cos(\theta_r)}} e^{-j2(k_0 y_i \sin(\theta_r) + \beta\, z_i \cos(\theta_r))}\, W_a(x_i) W_r(y_i \sin(\theta_r) - n\cos(\theta_r) z_i) \tag{5.1}$$

where n is the refraction index of the medium, θ_i and θ_r are the incident and refracted angles, respectively, $t_{i,j}$ is one-way transmission coefficient of amplitude from medium *i* to medium *j*, R is the propagation distance, *i.e.* the slant range of the pixel, α and β are real and imaginary part of $j\gamma$, which γ, α, and β are propagation, absorption, and phase constants of the medium, k_0 is free air wavenumber, and s_i is the scattering amplitude of the scatterer.

The complex-valued SAR backscattering $\boldsymbol{u}$, *i.e.* the total backscattering from the scattering points within a resolution element, is the coherent summation of the point scatterers' backscattering (Lei et al., 2016; Treuhaft et al., 1996)

$$\boldsymbol{u} = \sum_{i=1}^{N} u_i \tag{5.2}$$

where u_i is the backscattering signal of the point scatterer located at (x_i, y_i, z_i) within the soil. The point scatterers are randomly distributed in the soil volume, randomizing the total signal which is the summation of random signals. By assuming uniform random distribution, the soil volume can be considered as a symmetric target in the azimuth and ground range directions, meaning that the backscattered signal is a function of variations in the vertical direction.

The pixel's backscattering is the collection of contributions of all scatterers (grains) embedded in the soil (Treuhaft et al., 1996). The scattering and absorption coefficients of a scatterer are functions of its size, dielectric constant, and the wavelength. In the cases where the particle size is much smaller than the wavelength, *i.e.* clay, silt, and sand soil particles, Rayleigh approximation can be used to express the scattering, extinction, and absorption coefficients (Tsang et al., 2000; Ulaby et al., 1981; Mätzler, 1998). It is an approximation of Mie equations and can expressed by only the first two terms of the Mie series (Ulaby et al., 1981; Mätzler, 1998)

$$\xi_s = \frac{8}{3}\chi^4|K|^2 \tag{5.3}$$

$$\xi_e = \chi\, Im(-K) + \frac{8}{3}\chi^4|K|^2 \tag{5.4}$$

$$\xi_a = \xi_e - \xi_s \tag{5.5}$$

where ξ_s, ξ_e, and ξ_b, are the scattering, extinction, and backscattering efficiencies, respectively, and

$$K = \frac{n^2-1}{n^2+2} \tag{5.6}$$

$$\chi = \frac{2\pi r_p}{\lambda}\sqrt{\epsilon_b'} \tag{5.7}$$

$$n = \frac{n_p}{n_b} \tag{5.8}$$

In the equations above, λ is free space wavenumber, r_p is the radius of the point scatterer, $\epsilon_b^{'}$ is the real part of the dielectric constant of the background, n_p and n_b are complex indices of refraction of the scatterer and the background, and n is the ratio of the two refraction indices.

The expressions in equation (5.2) are valid only for $|n\chi| \ll 0.5$ (Tsang et al., 2000; Ulaby et al., 1981). Consequently, for L-band radar measurements, the Rayleigh approximation is always valid for medium and small grains, *i.e.* sand, silt, and clay, even with large dielectric constants of the soil. For larger grain sizes, *e.g.* gravel, depending on the dielectric constant, the assumption may not always be satisfied. Once the dielectric constant of the soil increases, the indicator$|n\chi|$ gradually increases to reach values larger than 0.5 (see equations (5.6) and (5.7)). For C-band measurements, depending on the dielectric constant of the medium, the Rayleigh approximation may not be applicable even for medium grain sizes. In such cases, Mie equations (Ulaby et al., 1981; Mätzler, 2002; Bohren and Huffman, 1983), which involve no approximations, should be used instead.

Using Mie solutions, the scattering, extinction, and backscattering efficiencies and scattered complex amplitudes are expressed in the form of converging series (Ulaby et al., 1981; Mätzler, 2002; Bohren and Huffman, 1983)

$$\xi_s = \frac{2}{\chi^2}\sum_{k=1}^{\infty}(2k+1)(|a_k|^2 + |b_k|^2) \tag{5.9}$$

$$\xi_e = \frac{2}{\chi^2}\sum_{k=1}^{\infty}(2k+1)Re(a_k + b_k) \tag{5.10}$$

$$\xi_b = \frac{1}{\chi^2}|\sum_{k=1}^{\infty}(2k+1)(-1)^k(a_k - b_k)|^2 \tag{5.11}$$

$$S_{1\,(\cos\theta)} = \sum_{k=1}^{\infty}\frac{2k+1}{k(k+1)}(a_k\pi_k + b_k\tau_k) \tag{5.12}$$

$$S_{2\,(\cos\theta)} = \sum_{k=1}^{\infty}\frac{2k+1}{k(k+1)}(a_k\tau_k + b_k\pi_k) \tag{5.13}$$

where S_1 and S_2 are the scattered complex amplitudes for perpendicular and parallel polarized waves, respectively. In the equation above, θ is the scattering angle, π_k and τ_k are functions of θ and n, and finally a_k and b_k are known as the Mie coefficients. The equations for the coefficients are not repeated here, instead interested readers are referred to (Ulaby et al., 1981; Mätzler, 2002; Bohren and Huffman, 1983) and the references therein for more details about the coefficients and strategies to calculate them.

Once the Mie efficiencies are calculated, the volume cross sections (m^2/m^3) are obtained by summing cross sections (m^2) over N_v (m^{-3}) particles per unit volume

$$\kappa_s = \sum_{k=1}^{N_v} Q_s(r_k) = \sum_{k=1}^{N_v}\xi_s(r_k) \times \pi {r_k}^2 \tag{5.14}$$

$$\kappa_e = \sum_{k=1}^{N_v} Q_e(r_k) = \sum_{k=1}^{N_v}\xi_e(r_k) \times \pi {r_k}^2 \tag{5.15}$$

where κ_s and κ_e are volume scattering cross section and volume extinction cross section, respectively, and N_v is the number of point scatterers embedded in the soil. The volume absorption coefficient is related to absorption constant of the medium α by $\kappa_a = 2\alpha$ (Ulaby et al., 1981). The extinction coefficient κ_e includes the scattering coefficient κ_s and absorption coefficient κ_a of dielectric medium (Fung, 1994; Ulaby et al., 1986; Liu et al., 2016)

$$k_e = k_s + k_a \tag{5.16}$$

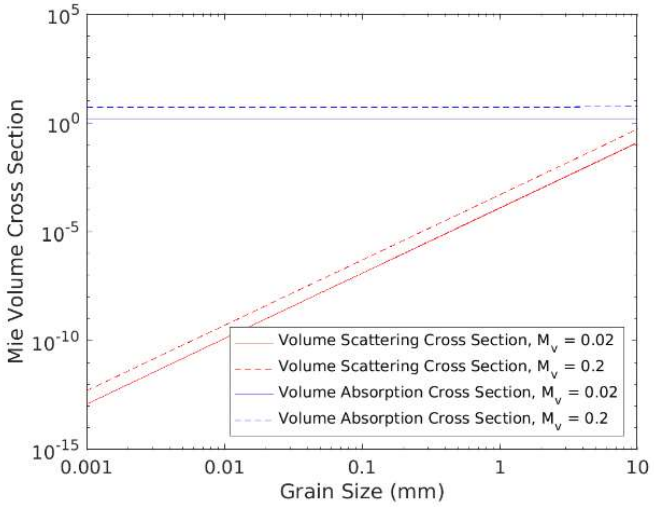

Figure 5.1. Mie volume scattering and absorption cross sections for different grain sizes.

Figure 5.1 shows the plot of Mie volume scattering and volume extinction cross sections (see equations (5.14) and (5.15)) for different grain sizes. It can be seen that Mie volume scattering cross section, plotted in logarithmic coordinates in figure 5.1, increases by enlarging the size of grains. For example, the Mie volume scattering cross section of a grain with the size

of 10 mm is about 1000 times larger than that of a grain with the size of 1 mm (figure 5.1). This means that the scattering of gravel grains with the radius of 1 cm occupying only 1% of a soil's solid volume is 10 times larger than the scattering of background grains with grain size of 1 mm occupying 99% of the total solid volume.

Unlike the volume scattering cross section, the volume extinction function is almost independent of grain size, at least for the range of sizes we study in this paper, *i.e.* up to a few centimeters. This means that the signal scattered by the soil volume is dominated by larger grains and that the contribution of smaller grains becomes negligible if large grains exist in the soil. However, all grains, regardless of their size, equally contribute to the absorption.

5.3 Simulating Results

5.31 Constant soil moisture profile

Here we provide simulation results for soils with different structures and soil moisture changes. In our model, the soil volume is assumed to a collection of randomly distributed point scatterers, *i.e.* larger grains, embedded in a lossy dielectric medium, *i.e.* finer grains. Without loss of generality, we assume a soil with $\overline{N}_v$ point scatterers of the same size r_p occupying f_s percent of the soil's total volume

$$\overline{N}_v = \frac{3f_s}{4\pi r_p^3} \tag{5.17}$$

where f_s is the fraction of the total volume occupied by the scattering soil particles. Then, we calculate soil moisture-induced interferometric phase and SAR intensity changes over the soil with different r_p and f_s values. The dielectric constant of wet soil was calculated using Hallikainen mixing model (Hallikainen et al., 1985). By increasing soil moisture, water fills the free spaces between the particles in the porous background. This increases the dielectric constant of the background. Unlike the porous background, large grains can only be wrapped by a layer of water. The thickness of the water layer increases by increasing soil moisture and its maximum thickness is related to the size of the free spaces, *i.e.* voids between background grains. To estimate the dielectric constant of a grain wrapped by a layer of water we used Maxwell-Garnett (Maxwell-Garnett, 1904) mixing equation (Sihvola, 1999)

$$\varepsilon_{eff} = \varepsilon_0 + 3f\varepsilon_0 \frac{\varepsilon_s - \varepsilon_0}{\varepsilon_s + 2\varepsilon_0 - f(\varepsilon_s - \varepsilon_0)} \tag{5.18}$$

where $f = \frac{v_s}{v_s + v_l}$ is the volume fraction of the solid grain, ε_{eff} is the effective dielectric constant, ε_0 is the dielectric constant of water, ε_s is the dielectric constant of the grain, v_s is the volume of the grain, and v_l is the value of the water layer. It should be noted that unlike the dielectric constant of the background, the dielectric constant of the larger grains, *i.e.* scatterers, slightly increase because the thickness of the water layer, which is related to the dimension of the free spaces, is much smaller than the size of scatterers.

Figure 5.2 shows modeled interferometric phase and intensity changes for different soils as a function of r_p and f_s (see equations (5.1) and (5.2)). It can be seen that the intensity is

proportional to the volume geometric cross section, *i.e.* $\sigma_g = \pi {r_p}^2 \overline{N}_v$, whereas phase change is proportional to $1/\sigma_g$.

5.3.2 Variable soil moisture profile

Constant soil moisture profile has been assumed to derive equation (5.1). This means that the attenuation and phase constants of the soil are independent of depth. However, with variable soil moisture profiles the attenuation and phase constants become functions of depth and we can rewrite equation (5.1) as

$$\boldsymbol{u} = \sum_{i=1}^{N} e^{-j2k} \; t_{1,2}\, t_{2,1}\, s_i \, e^{-2\int_0^z \frac{\alpha}{\cos(\theta_r)} dz'} e^{-j2(k_0 y_i \sin(\theta_r))}$$

$$e^{-2j\int_0^z \beta \cos(\theta_r) dz'} W_a(x_i) W_r(y_i \sin(\theta_r) - n\cos(\theta_r) z_i) \tag{5.19}$$

Figure 5.3 shows modeled SAR intensity and interferometric phase over a soil with different soil moisture profiles. The soil is loam containing 1.5% gravel grains of average radius of 2.5 cm. The soil moisture values at the surface are in the range of 0 and 0.50 and linearly changes with depth until it becomes 0.40 at depth 40 cm. In order to generate interferometric phases, we assume the master image to have variable soil moisture profile with the value of 0.10 at surface and 0.40 at the depth 40 cm. The results show that the depth-resolved and depth-averaged backscattered intensities are almost equal when shallow depths hold large soil moisture. Note that depth-resolved means a profile of variable soil moisture whereas depth-averaged indicates a constant soil moisture profile. However, by decreasing the soil moisture

values at shallow depths, the depth-averaged intensities take larger values compared to the depth-resolved intensity. Similar results can be seen in phase changes where larger difference between depth-resolved and depth-averaged phase changes can be observed at smaller soil moisture values.

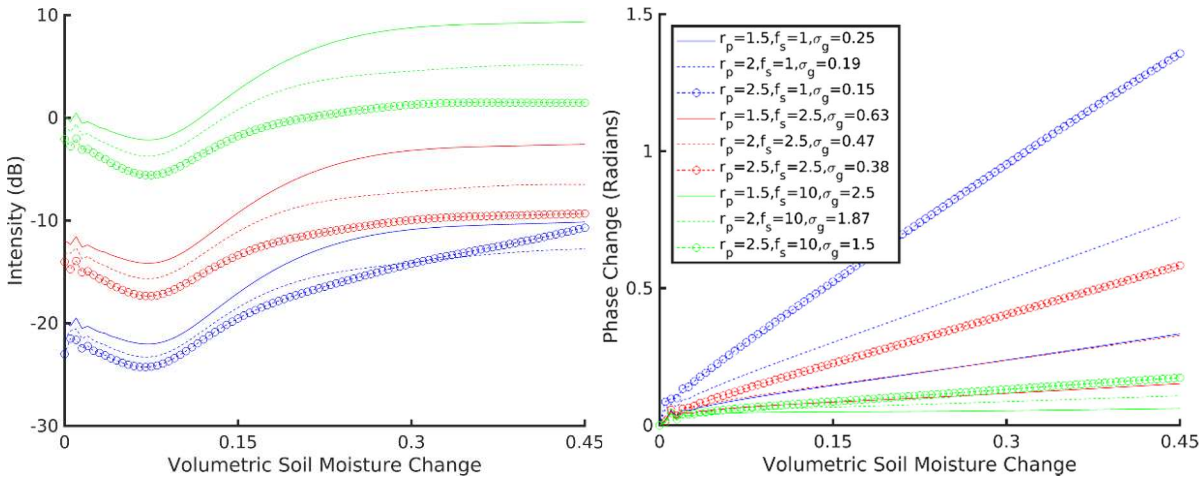

Figure 5.2. L-band soil moisture-induced SAR intensity changes and InSAR phase changes for different soil structures and different soil moisture changes.

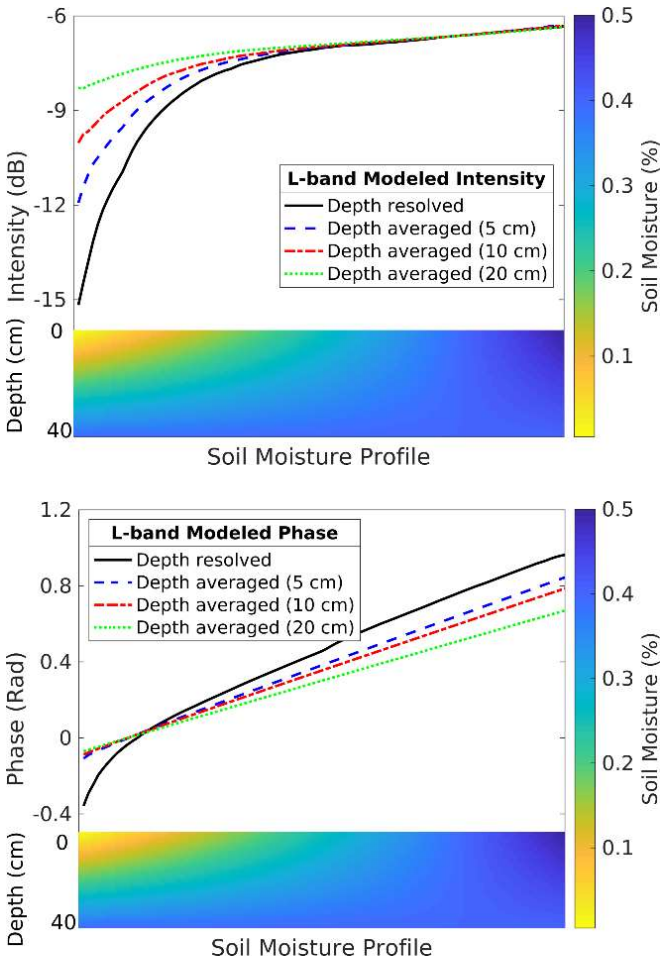

Figure 5.3. L-band soil moisture induced SAR intensity and phase changes for uniform and variable soil moisture profiles.

5.4 Discussion

There are two main steps in modeling soil moisture induced intensity and phase changes of a single-looked pixel on a SAR image. The first step is to model the dielectric medium (soil here) and the second step is to estimate intensity and phase changes due to changes in soil moisture. Most of the models introduced so far model soil as a continuous scattering medium (Zwieback et al., 2015; De Zan et al., 2014). The models then use a cross correlation between two soils with different soil moisture values to estimate the phase change. The model introduced

in this paper, however, differs in strategy from previous models in two ways. The first is that the model in this work considers the soil to be a discrete dielectric medium. The second lies in the approach we used to estimate the soil moisture-induced intensity and phase changes. The previous models aim to model the cross correlation between two single-looked pixels. In contrast, the model in this paper is a SAR based model that directly quantify SAR intensity of a single-looked pixel as a function of soil moisture. It also calculates phase change of a SAR pixel as a function of soil moisture.

5.4.1 Modeling dielectric medium (soil)

Generally, there are two main approaches that can be used to model a scattering object in order to estimate the phase and intensity changes. The first approach is to consider the scattering object as a collection of discrete scatterers embedded in a dielectric medium. In this model, the contribution of a single scatterer to the scattered signal is a function of its size, position and dielectric constant of the scatterer and the medium's dielectric constant. The second approach is to assume the scattering object as a continuous medium. The total signal in the case of continuous medium is expressed as a coherent sum of correlation among pairs of infinitesimal slabs along the vertical direction. This mathematically implies that every infinitesimal particle of the entire soil profile acts like a scattering object. The model neglects the influence of the structure of soil, *i.e.* the dimensions and distribution of scatterers, on the scattered signal. However, as explained in the previous section, the backscattering of a scatterer is a function of its size (Ulaby et al., 1981). Figure 5.4 shows such a relationship between grain size and Mie scattering cross section. The relationship between a scatterer's size and its backscattering, illustrated in figure 5.1 and figure 5.4, indicates that the scatterers' size should be considered in the models. It also indicates that a small grain's contribution to the total signal is negligible

compared to the contribution of a larger grain in the models. However, all grains, regardless of their sizes, equally contribute to the absorption. This means that scattering is a function of scatterer size and absorption is independent of it. Therefore, considering these, we have modeled the soil as a collection of discrete coarse scatterers embedded in an attenuating dielectric medium.

5.4.2 Estimating intensity and phase changes

Once the dielectric medium, *i.e.* soil, is modeled as a collection of scatterers, the soil moisture-induced intensity and phase changes can be estimated by exploiting a model. Imagine that *n* scatterers, *i.e.* $a_{1,1}e^{j\varphi_{1,1}}, a_{1,2}e^{j\varphi_{1,2}}, \dots, a_{1,\mathrm{n}}e^{j\varphi_{1,\mathrm{n}}}$, are within the single-looked pixel $\boldsymbol{u_1}$ on the first image where $a_{1,i}$ and $\varphi_{1,i}$ are the amplitude and phase of the scattered signal of the i^{th} scatterer. Now imagine that changes happened in soil moisture. This in turn leads to the changes in the amplitudes and phases of the scatterers. Therefore, for the same pixel on the second image, the backscattering values of the scatterers are $a_{2,1}e^{j\varphi_{2,1}}, a_{2,2}e^{j\varphi_{2,2}}, \dots, a_{2,\mathrm{n}}e^{j\varphi_{2,\mathrm{n}}}$. Now a model should be exploited to quantify phase change of the single-looked pixel between the two SAR images due to soil moisture change. The common approach in the literature has been applying a cross correlation between the two scattering objects, *i.e.* soil here. Therefore, the phase change can be calculated by

$$\emptyset_{1,2} = \arg\left(\sum_{i=1}^{n} a_{1,i}\, a_{2,i}\, \frac{e^{j\varphi_{2,i}}}{e^{j\varphi_{1,i}}}\right) \tag{5.20}$$

Note that SAR images are not generated in this approach and phase change is estimated from two modeled scattering objects by exploiting cross-correlation. Cross-correlation is a common approach to estimate interferometric phase in multi-looking process. However, the performance of cross correlation applied in modeling scattering objects is different from that of cross correlation conducted in multi-looking processing aiming to improve phase estimation. In multi-looking processing, the single-looked pixels in the multi-looking window on the first image are multiplied to the complex conjugate of the equivalent single-looked pixels on the second image. Here, however, cross-correlation is conducted between the stable point scatterers within the first single-looked pixel and the point scatterers within the second single-looked pixel. This means that the scatterers within the single-looked pixel on the first image are multiplied to the complex conjugate of the equivalent scatterers on the second image.

We argue here that applying cross-correlation to model soil moisture-induced phase changes cause phase artifacts. Since the amplitudes of the equivalent single-looked pixels are multiplied (see equation (5.20)), using cross-correlation in multi-looking process, weaker pixels, *i.e.* pixels with smaller amplitude and noises, have less influence on the estimated multi-looked phase. Thus, multi-looking improves phase estimation by decreasing the influence of weaker pixels. Unlike this, cross-correlation, however, can lead to biased phase estimations when it is exploited for dielectric mediums, *e.g.* soil. Soil is loosy dielectric medium, the phase of a scatterer increases by increasing its depth whereas its amplitude decreases at the same time. In this case, weaker scatterers, *i.e.* deeper scatterers with smaller amplitudes, are associated with larger phases. This means that by applying cross-correlation, scatterers with larger phases have less influence on the estimated phase. Since this effect increases by increasing soil moisture changes, phase curves tends to saturate at higher soil moisture changes. Saturated phase curves

have been documented in previous models (Zwieback et al., 2015; De Zan et al., 2014) in which cross-correlation has been used to model soil moisture induced interferometric phase.

Another consequence is non-zero closure phase for single-looked pixels, which has been documented in previous models (Zwieback et al., 2015; De Zan et al., 2014). Note that closure phase of single-looked pixels is zero in observations. This effect is similar to phase artifact in multi-looking process and interested readers are referenced to Molan et al., 2020, for more details about the multi-looking artifacts. We also notice that, in practice, unlike the cross-correlation approach, we use SAR images to generate interferograms since the signals of the single point scatterers within the soil volume are not available separately.

In this paper, instead of applying cross-correlation, we first model SAR pixel and then calculate the phase and intensity changes between SAR images with different soil moisture values. A single pixel on a SAR image is a vector summation of the signals of single scatterers within the resolution cell

$$\boldsymbol{u}_j = \sum_{i=1}^{n} a_{j,i} e^{j\varphi_{j,i}} \tag{5.21}$$

Then, the interferometric phase of two single-looked pixels on SAR images is simply calculated by subtracting the phase of first SAR image from the phase of the second image

$$\emptyset_{1,2} = \varphi_2 - \varphi_1 = \arg\left(\frac{\sum_{i=1}^{n} a_{2,i} e^{j\varphi_{2,i}}}{\sum_{i=1}^{n} a_{1,i} e^{j\varphi_{1,i}}}\right) \tag{5.22}$$

Here, one may argue that a shallower scatterer with larger amplitude contributes to a SAR pixel's signal more than a deeper scatterer with smaller amplitude, alike the aforementioned case in cross-correlation. However, it should be noted that the influence of amplitude on interferometric phase between two acquisitions decreases because amplitude appears in the denominator as well as the numerator of the equation (5.22). On the other hand, as it can be seen in equation (5.20), the counterbalancing of amplitude influence doesn't happen in cross-correlation. Instead, cross-correlation increases the influence of the amplitude by multiplying the amplitudes.

5.4.3 Negative slope on SAR intensity curves

One of the features, which is occasionally observed on SAR intensity curves is inverse relation between soil moisture and backscatter for small soil moisture values, e.g. mv<0.10. This phenomena is thought to be due to a decrease in the subsurface scattering and an increase in surface scattering upon wetting (Barrett et al., 2009; Liu et al., 2016). However, not all intensity curves feature such a negative slope for small soil moisture values, indicating that this may not the case. We argue that the negative slope appears when the dielectric constant of the dry background, e.g. silt, sand, and clay, is smaller than the dielectric constant of point scatterers, e.g. gravel sized grains. The porous background has smaller dielectric constant compared to the individual larger soil particle due to the smaller dry bulk density. As the background soil absorbs water, its dielectric constant increases and gets closer to the dielectric constant of the point scatterers, resulting in decreased backscatter at their interface. The backscattering then increases upon more wetting. Figure 5.4 shows the Mie backscattering (see equation (5.11)) of point scatters with dielectric constant of 3.3 embedded in a background with dielectric constant of 2.5

at dry condition. As it can be observed on the plot, backscattering decreases at first and then increase upon more wetting.

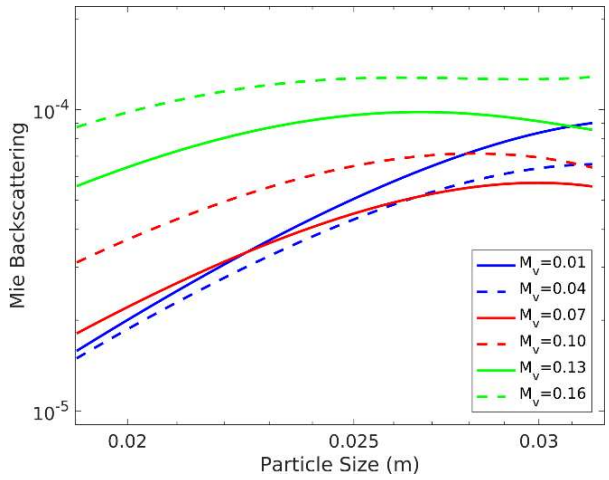

Figure 5.4. Mie backscattering for different soil moisture values and different particle sizes. M_v is volumetric soil moisture (ratio of soil volume occupied by water).

5.5 Evaluation

To evaluate our model, we choose ALOS PALSAR data over Idaho where in-situ soil moisture measurements are available at the Orchard Range SCAN station (https://www.wcc.nrcs.usda.gov/). Co-registered SLC images are used to generate multi-looked interferograms with 6 and 3 looks in azimuth and range, respectively. Table 5.1 provides the dates of the SAR images. The path and frame numbers are 208 and 860, respectively. The topographic phase is simulated using the Digital Elevation Model (DEM) of Shuttle Radar Topography Mission (SRTM) with 1 arc-second spatial resolution and is then removed from the interferograms. After removing those interferograms with low coherence over the soil moisture station, a total of 87 remaining interferograms are selected. The perpendicular baseline of the

selected interferograms ranges between 12 m and 1970 m and the maximum temporal baseline is 1196 days.

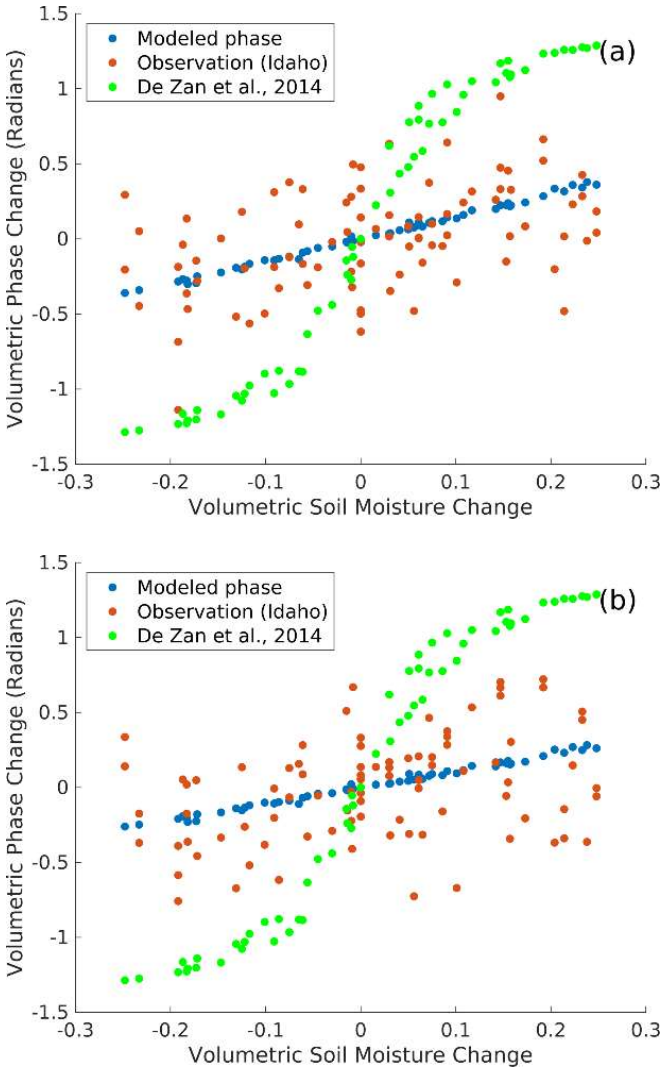

Figure 5.5. The modeled and observed interferometric phases at point (a) with grain size of 2.8 cm and volume fraction of 3.6 percent, and point (b) with grain size of 2.75 cm and volume fraction of 5.2 percent.

No.	date	No.	date	No.	date
1	2007-07-05	7	2008-07-07	13	2010-05-28
2	2007-08-20	8	2009-01-07	14	2010-07-13
3	2007-11-20	9	2009-07-10	15	2010-08-28
4	2008-01-05	10	2009-10-10	16	2010-10-13
5	2008-04-06	11	2010-01-10	17	2011-02-28
6	2008-05-22	12	2010-04-12		

Table 5.1. The date (yyyy-mm-dd) of the SLC images.

Figure 5.5 illustrates the comparison between our model and the model introduced by De Zan et al., 2014, with observed interferometric phases at two pixels around the station where soil moisture measurements are available. The model introduced in De Zan et al., 2014, has been used for soil moisture estimations and later revised by Zwieback et al., 2017, to accommodate depth variable soil moisture cases. This model assumes the temporal changes in soil moisture to be the primary influential factor. Hence, it doesn't consider the influence of soil's structure on InSAR phase changes. Therefore, unlike our model, its estimated phase for (a) and (b) cases (see figure 5.5) are the same regardless of their different phase behaviors due to different soil structures. In figure 5.6, the modeled intensity is compared with the observed intensity. Also, in figure 5.7, intensity changes are compared with the observed intensity changes. The plots show that our model is very successful in estimation of InSAR phase and SAR intensity. By fitting the modeled phase and intensity values to the observed intensity and phase values (see figure 5.6 and figure 5.7), the grain sizes of 2.8 and 2.75 cm with volume fractions of 3.6 and 5.2 percent, respectively for (a) and (b) are estimated. The dielectric constant of the scatterers is also

estimated to be 2.7 and the maximum layer of water that wraps larger grains is estimated to be 1.1 mm.

Upon wetting, the replacement of air within free spaces of soil by water increases the dielectric constant of the soil. The increase in dielectric constant corresponds to an increase in the wavenumber in the soil. This means that the wave fronts propagating in the soil become closer as soil becomes wetter. However, soil moisture contribution to the final signal received by antenna appertain more to soil structure. Generally, as the density of scatters increases, the magnitude of scattered waves at shallower depths increase and relatively smaller portion of the wave has the chance to reach deeper depths and gain larger phase changes. This is because a wave backscattered by a scatterer at depth 10 cm, for instance, experiences twice larger phase changes compared to a wave backscattered by a scatterer located at depth 5 cm in a homogeneous medium. On this account, soil moisture-induced InSAR phase change decreases by increasing the volume fraction and/or size of the scatterers. At the same time, however, the backscattered intensity increases as the volume fraction and/or size of the scatterers increases. This fact can be observed in our model's results shown in figure 5.2 and also in figures 5.5 and 5.6, which feature the comparison between real and modeled phase and intensity changes. It can be seen that the intensity is proportional to the volume geometric cross section whereas phase change is inversely proportional to it. In other words, pixels with smaller volume geometric cross section are associated with larger soil moisture-induced phase changes and smaller intensities. Theoretically, a pixel can take large phases (say 2 rad. and even larger) however, in practice, such pixels are difficult to study since the intensity gets closer to the noise equivalent signal zero (NESZ). Therefore, the largest detectable soil moisture-induced phase changes is relevant to NESZ of the data.

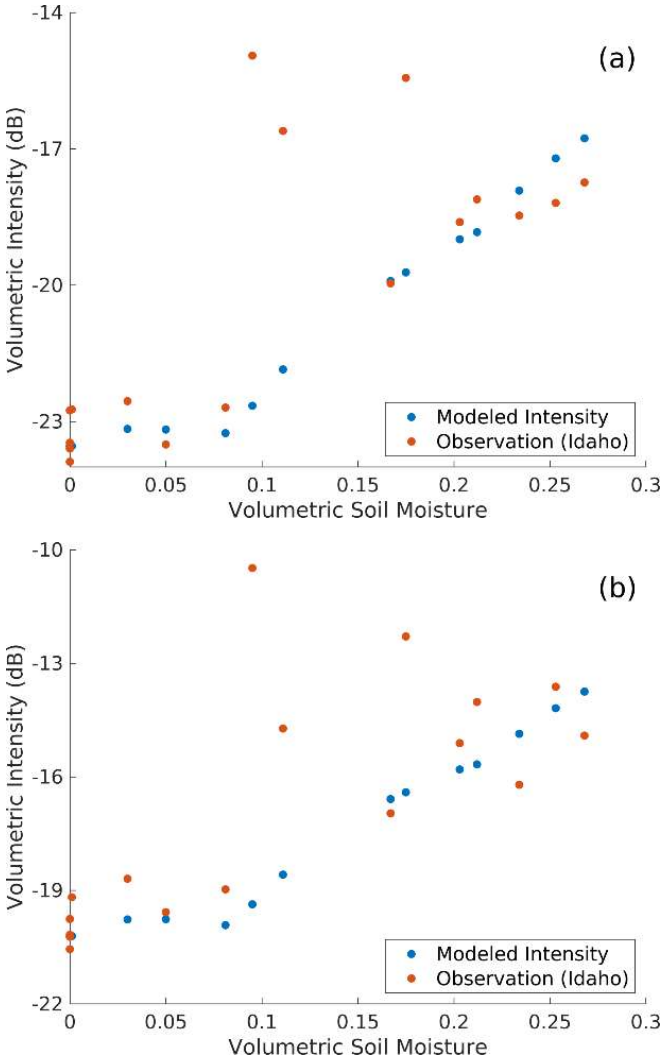

Figure 5.6. The modeled and observed SAR intensity.

Three measurements exhibit very high values on intensity plots (figure 5.6), indicating a strong change in the backscattering property of the soil. The observed out-of-range values (figure 5.6) are so high that even fully saturated soil could not generate such a strong backscattering. Therefore, the mechanism that leads to the high values of intensity could not be elucidated considering soil moisture changes solely. Instead, we attribute this to the change in the structure of soil due to freezing. The weather record over the study area indicates that the soil

temperatures of the three measurements are below 0°C. The dielectric constant of ice, which is about 3.2, is very close to the dielectric constant of soil particles. When soil freezes, the pore ice bonds soil particle together, resulting in a larger almost homogenous scatterer. The change in the structure of the soil due to freezing decorrelates the backscattered signals (Molan et al., 2018b), leading to low coherence between frozen and non-frozen soils. In this case where the coherence is low, intensity changes can be potentially used for analyzing the radar responses of frozen soil. However, we don't cover this issue in this research as it is beyond the scope of this research.

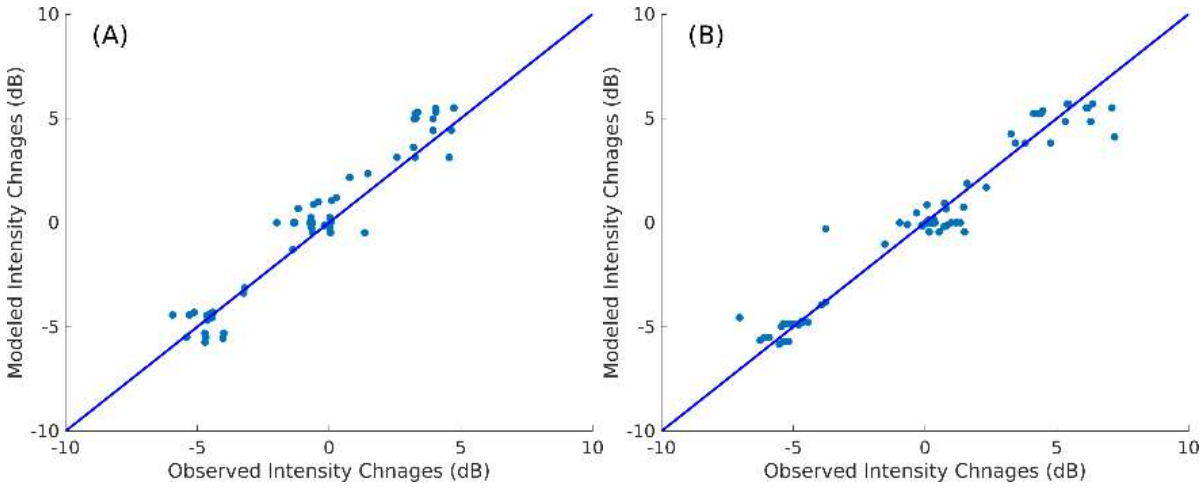

Figure 5.7. The modeled and observed SAR intensity changes.

5.6 Conclusion

Unlike previous models, which are only applicable for either intensity or phase estimations, our volume scattering model successfully estimates SAR intensity changes as well as InSAR phase changes. Also, while previous interferometric models provide phase changes due to soil moisture changes, they don't take into the account the structure of the soil, *i.e.* soil particle size and distribution. The model introduced in this paper models the soil as a discrete

dielectric constant medium with larger scatterers embedded within a finer grain background of soil. It takes into account the scatterers' sizes and their volumetric fraction. This may open new window in the study of soil structure using SAR and InSAR methods.

The volume scattering models so far have been used along with surface models to estimate soil moisture-induced SAR intensity changes. Based on this hypothesis, the negative slope on intensity curves is attributed to volume scattering, which decreases by increasing soil moisture. The volume scattering model provided in this study, however, is successful in estimation of SAR intensity changes.

The model in this work predicts reverse relationship between soil moisture changes and SAR intensity changes for small soil moisture values. We attribute this to the difference between the dielectric constants of dense point scatterers and porous dry background.

The previous models lead to non-zero phase triplets for single focused pixels, which is zero in real world and also in our model. This is because the models don't generate SAR images and instead, they apply a cross-correlation to estimate phase changes from modelled pixels.

Acknowledgment: The work was funded by the NASA Earth Surface & Interior Program (80NSSC19K1491, NNX16AK56G) and the Shuler-Foscue Endowment at Southern Methodist University.

References

Massonnet, D., and K. Feigl. 1998. Radar interferometry and its application to changes in the Earth's surface, *Rev. Geophys.,* 36, 441-500.

Bürgmann, R., P.A. Rosen, and E.J. Fielding. 2000. Synthetic aperture radar interferometry to measure Earth's surface topography and its deformation. Annu. Rev. *Earth Planet. Sci.,* 28, 169–209.

Lu, Z., and D. Dzurisin. 2014. InSAR Imaging of Aleutian Volcanoes: Monitoring a Volcanic arc from Space, Geophysical Sciences, Springer Praxis Books, Springer: Chichester, UK, 2014, p. 390.

Molan, Y.E., J.-W. Kim, Z. Lu, B. Wylie, and Z. Zhu. 2018a. Modeling Wildfire-Induced Permafrost Deformation in an Alaskan Boreal Forest Using InSAR Observations. Remote Sens., 10, 405.

Ferretti, A., C. Prati, and F. Rocca. 2001. Permanent scatterers in SAR interferometry. IEEE Transactions on Geoscience and Remote Sensing, 39, 8–20.

Lu, Z., and D. Meyer. 2002. Study of high SAR backscattering due to an increase of soil moisture over less vegetated area: its implication for characteristic of backscattering. *International Journal of Remote Sensing*, 23 (6), 1065-1076.

Nolan, M., D. R. Fatland, and L. Hinzman. 2003. DInsar measurement of soil moisture. IEEE Trans. Geosci. Remote Sens., vol. 41, no. 12, pp. 2802–2013.

Barrett, B., E. Dwyer, and P. Whelan. 2012. The use of C- and L-band repeatpass interferometric SAR coherence for soil moisture change detectionin vegetated areas. Open Remote Sens. J., vol. 5, no. 1, pp. 37–53.

Zwieback, S., S. Hensley, and I. Hajnsek. 2015. Assessment of soil moisture effects on L-band radar interferometry. *Remote Sens. Environ*. 2015, 164, 77–89, doi:10.1016/j.rse.04.012.

De Zan, F., A. Parizzi, P. Prats-Iraola, and P. Lopez-Dekker. 2014. A SAR interferometric model for soil moisture. *IEEE Transactions on Geoscience and Remote Sensing*, 52, 418–425.

Hensley, S., T. Michel, J. Van Zyl, R. Muellerschoen, B. Chapman, S. Oveisgharan, Z. S. Haddad, T. Jackson, and I. Mladenova. 2011. Effect of soil moisture on polarimetric-

interferometric repeat pass observations by UAVSAR during 2010 Canadian Soil Moisture campaign. In Proc. *IEEE IGARSS*, pp. 1063–1066.

Hooper, A., D. Bekaert, K. Spaans, and M. Arikan. 2012. Recent advances in SAR interferometry time series analysis for measuring crustal deformation. *Tectonophysics,* vols. 514–517, pp. 1–13.

Hanssen, R. 2001. Radar Interferometry: Data Interpretation and Error Analysis, vol. 2. Dordrecht, The Netherlands: Kluwer.

Gabriel, R. Goldstein, and H. Zebker. 1989. Mapping small elevation changes over large areas: Differential radar interferometry. J. Geophys. Res., vol. 94, no. B7, pp. 9183–9191.

Cardinali, M., F. Ardizzone, M. Galli, F. Guzzetti, and P. Reichenbach. 2000. Landslides triggered by rapid snow melting, the December 1996-January 1997 event in Central Italy," *in proceedings of the EGS Plinius Conference,* Cosenza, Italy, 439-448.

Robinson, D.A., and C. S. Campbell. 2008. Soil Moisture Measurement for Ecological and Hydrological Watershed-Scale Observatories: A Review. *Vadose Zone J.*, 7, 358–389.

Hirschi, M., P. Viterbo, and S. Seneviratne. 2006. Basin-scale water balance estimates of terrestrial water storage variations from ECMWF operational forecast analysis. *Geophys. Res. Lett.*, 33, L21401.

Liang, W.L., F. X. Hung, M. C. Chan, and T. H. Lu. 2014. Spatial structure of surface soil water content in a natural forested headwater catchment with a subtropical monsoon climate. *J. Hydrol*., 516, 210–221.

Seneviratne, S.I., P. Viterbo, D. Luthi, and C. Schar. 2004. Inferring changes in terrestrial water storage using ERA-40 reanalysis data: The Mississippi River basin. *J. Clim*., 17, 2039–2057.

Gabriel, R. Goldstein, and H. Zebker. 1989. Mapping small elevation changes over large areas: Differential radar interferometry. J. Geophys. Res., vol. 94, no. B7, pp. 9183–9191.

Nolan, M., D. R. Fatland, and L. Hinzman. 2003. DInsar measurement of soil moisture. IEEE Trans. Geosci. Remote Sens., vol. 41, no. 12, pp. 2802–2013.

Zhang, T., Q. Zeng, Y. Li, and Y. Xiang. 2008. Study on relation between InSAR coherence and soil moisture. In Proc. ISPRS Congr., vol. 37, pp. 131–134.

Barrett, B., E. Dwyer, and P. Whelan. 2012. The use of C- and L-band repeatpass interferometric SAR coherence for soil moisture change detectionin vegetated areas. Open Remote Sens. J., vol. 5, no. 1, pp. 37–53.

Hajnsek, I., and P. Prats. 2008. Soil moisture estimation in time with DInSAR. In Proc. *IEEE IGARSS*, vol. III, pp. 546–549.

Nesti, G., D. Tarchi, and J.-P. Rudant. 1995. Decorrelation of backscattered signal due to soil moisture changes. In Proc. Int. Geosci. Remote Sens. Symp., vol. 3, pp. 2026–2028.

Nesti, G., D. Tarchi, D. Despan, J.-P. Rudant, A. Bedidi, P. Borderies, and E. Bachelier. 1998. Phase shift and decorrelation of radar signal related to soil moisture changes. In Proc. 2nd ESA Int. Workshop Retrieval Bio- Geo-Phys. Parameter SAR Data Land Appl., pp. 423–430.

Rudant, J.-P., A. Bedidi, R. Calonne, D. Massonnet, G. Nesti, and D. Tarchi. 1996. Laboratory experiment for the interpretation of phase shift in SAR interferograms. In Proceedings of *FRINGE*.

Hensley, S., T. Michel, J. Van Zyl, R. Muellerschoen, B. Chapman, S. Oveisgharan, Z. S. Haddad, T. Jackson, and I. Mladenova. 2011. Effect of soil moisture on polarimetric-interferometric repeat pass observations by UAVSAR during 2010 Canadian Soil Moisture campaign. In Proc. *IEEE IGARSS*, pp. 1063–1066.

Morrison, K., J. C. Bennett, M. Nolan, and R. Menon. 2011. Laboratory measurement of the DInSAR response to spatiotemporal variations in soil moisture. *IEEE Trans. Geosci. Remote Sens*., vol. 49, no. 10, pp. 3815–3823.

Molan, Y.E., J.-W. Kim, Z. Lu, P. Agram. 2018b. L-Band Temporal Coherence Assessment and Modeling Using Amplitude and Snow Depth over Interior Alaska. *Remote Sens*. 10, 150.

Fung, A.K., Z. Li, and K.S. Chen. 1992. Backscattering from a randomly rough dielectric surface. *IEEE Trans. Geosci. Remote Sens.*, 30, 356-369.

Su, Z.,P. A. Troch, and F.P. De Troch. 1997. Remote sensing of bare surface soil moisture using EMAC/ESAR data. *Int. J. Remote Sens.*, 18, 2105-2124.

Baghdadi, N. and M. Zribi. 2006. Evaluation of radar backscatter models IEM, OH and Dubois using experimental observations. *Int. J. Remote Sens.* 27, 3831-3852.

Altese, E., O. Bolognani, M. Mancini, and P.A. Troch. 1996. Retrieving soil moisture over bare soil from ERS 1 synthetic aperture radar data: Sensitivity analysis based on a theoretical surface scattering model and field data. *Water Resour. Res.*, 32, 653-661.

Barrett, B., E. Dwyer, and P. Whelan. 2009. Soil moisture retrieval from active spaceborne microwave observations: An evaluation of current techniques," *Remote Sensing,* 1, 210–242.

Liu, P.-W., J. Judge, R.D. DeRoo, A.W. England, T. Bongiovanni, and A. Luke. 2016. Dominant backscattering mechanisms at L-band during dynamic soil moisture conditions for sandy soils. *Remote Sensing of Environment*, vol. 178, pp. 104 – 112.

Zwieback, S., I. Hajnsek, A. Edwards-Smith, and K. Morrison. 2017. Depth-resolved backscatter and differential interferometric radar imaging of soil moisture profiles: observations and models of subsurface volume scattering. *IEEE Journal of Selected Topics in Applied Earth Observations and Remote Sensing*.

Tsang, L., J. A. Kong, and K. H. Ding. 2000. Scattering of electromagnetic waves: Theories and applications. *John Wiley*, New York, 2000, pp 9-10.

Ulaby, F., R. Moore, and A. Fung. 1981. Microwave remote sensing: Active and passive. Vol. I, Boston, MA: Artech House, pp. 334-335.

Mätzler, C. 1998. Improved born approximation for scattering of radiation in a granular medium. *J. Appl. Phys.,* vol. 83, no. 11, pp. 6111–6117.

Lei, Y., P. Siqueira, and R. Treuhaft. 2016. A dense medium electromagnetic scattering model for the InSAR correlation of snow. *Radio Sci.*, 51, 461–480, doi:10.1002/2015RS005926.

Treuhaft, R.N., S.N. Madsen, M. Moghaddam, and J.J. Zyl. 1996. Vegetation characteristics and underlying topography from interferometric radar. *Radio Sci.,* 31(6), 1449–1485.

Mätzler, C. 2002. MATLAB functions for Mie scattering and absorption. Online document, https://omlc.org/software/mie/maetzlermie/Maetzler2002.pdf

Bohren, C. F., and D. R. Huffman. 1983. Absorption and Scattering of Light by Small Particles. John Wiley, New York, NY.

Fung, A. 1994. Microwave scattering and emission models and their applications. Norwood, MA: Artech House.

Hallikainen, M.T., F.T. Ulaby, M.C. Dobson, M.A. El-Rayes, and L.-K. Wu. 1985. Microwave dielectric behavior of wet soil—Part 1: Empirical models and experimental observations," *IEEE Trans. Geosci. Remote Sens.,* vol. GE-23, no. 1, pp. 25–34.

Maxwell-Garnett, J.C. 1904. Colours in metal glasses and in metallic films. *Philosophical Trans.*, Royal Soc London A 203:385–420.

Sihvola. A. 1999. Electromagnetic mixing formulas and applications. *IEEE Electromagnetic Waves Series,* No. 47. Institution of Electrical Engineers, Stevenage, Herts. UK.

Molan, Y.E., Z. Lu, and J-W. Kim. 2020. Influence of the statistical properties of phase and intensity on closure phase, *IEEE TGRS*, (submitted on Sep. 19, 2019)

CHAPTER 6

SOIL MOISTURE INDUCED PHASE, COHERENCE, AND CLOSURE PHASE CHANGES.

Molan, Y.E., and Lu, Z. 2020. Can InSAR Coherence and Closure phase be used to estimate soil moisture changes? *Remote Sensing.*

6.1 Introduction

InSAR can remotely sense mm to cm scale surface deformation with a high spatial resolution of tens of meters or better (Massonnet and Feigl, 1998; Bürgmann et al., 2000; Simons et al., 2007). InSAR has been used successfully to map surface deformations associated with different mechanisms, such as landslides, sinkholes, volcanism, subsidence, and permafrost (Lu and Dzurisin, 2014; Ferretti et al., 2001; Molan et al., 2018; Rykhus and Lu, 2008; Liu et al., 2010). Two SAR images of the same area with the same looking angle taken at different times can be used to generate an interferogram. After removing topographic phase, orbital, and atmospheric phase artifacts, the phase of an interferogram represents the deformation between two images in the line of sight direction. Between the two image acquisitions of an interferogram, however, soil moisture may have also changed. The change in water content contributes to InSAR phase and SAR intensity changes (Molan and Lu, 2020a). This, in turn, can influence inferred deformation and potentially affect InSAR coherence.

Soil moisture is a key variable in many agricultural and environmental studies, and plays a vital role in the terrestrial water cycle, exchange of energy, and carbon fluxes between the atmosphere and the land surface (Hirschi et al., 2006; Liang et al., 2014; Seneviratne et al., 2004). Also, some terrestrial processes and subsequent movements are in a close relationship with the changes in soil moisture. For example, rapid snowmelt or heavy precipitation can trigger sudden landslides (Cardinali et al., 2000). Groundwater conditions can be indicated by soil moisture condition (Robinson and Campbell, 2008). Also, soil moisture is closely related to permafrost thawing and deformation (Molan et al., 2018; Rykhus and Lu, 2008; Liu et al., 2010).

Many studies have been introduced to estimate soil moisture changes using InSAR phase and SAR intensity (De Zan et al., 2014, 2015; Zwieback et al., 2015, 2016; Molan et al., 2018b; Hoekstra and Delaney, 1974; Hallikainen et al., 1985). However, soil moisture estimation using InSAR phase has encountered difficulties and uncertainties. The spatial and temporal variabilities of soil moisture, unlike deformation, are complex (Hensley et al., 2011). In many cases, soil moisture varies abruptly, for example, across boundaries of different land cover types or two agricultural fields. Therefore, it is not always correlated spatially (Zwieback et al., 2015; Hensley et al., 2011). Temporal variability of soil moisture is also complex due to, for example, precipitation and seasonal effects (Hensley et al., 2011). In addition, intensity and phase contribution of non-soil moisture changes cannot be easily distinguished from the soil moisture signal. Despite these difficulties, complex SAR images have been used to estimate soil moisture [*e.g.* De Zan et al., 2015; Zwieback et al., 2015; Hensley et al., 2011).

In order to avoid the difficulties in estimating soil moisture using InSAR phase, recently, some studies have introduced approaches to estimate soil moisture using closure phase. By assuming that closure phase has contributions from the magnitude of soil moisture changes,

Zwieback et al. (2017) tried to establish approaches to estimate soil moisture using closure phase and InSAR coherence. Closure phase (*a.k.a.* phase triplet) is the combination of three interferograms generated from three SAR images. The phase of the single-looked interferogram pairing the first and the third SAR images equals the summation of the phases of the two intermediate single-looked interferograms. This means non-zero phase triplet does not exist in single-looked pixels (Molan et al., 2020). For multi-looked pixels, however, closure phase has non-zero values (Zwieback et al., 2017; Molan et al., 2020; De Zan and Gomba, 2018). Some studies have discussed the possible causes of non-zero phase triplet. De Zan et al. (2015) argued that non-zero phase triplet could happen due to interference of different scatterer populations with independent phase behaviors. The authors associated closure phase to the changes in the water content of soil and vegetation. Also, Zwieback et al. (2015) argued that deformations do not cause non-zero phase triplet. The authors suggested that non-random effects of decorrelation noise, non-zero spatial baselines, and the change in dielectric constant can potentially cause phase inconsistency (De Zan et al., 2015; Zwieback et al., 2015).

In contrast to the hypothesis that the magnitude of changes contributes to closure phase (Zwieback et al., 2017; De Zan and Gomba, 2018), a new study showed that closure phase is independent from the magnitude of changes (Molan et al., 2020). Using analytical and statistical approaches, Molan et al. (2020) studied the influence of the statistical properties of intensity and phase of single-looked pixels on multi-looked phase and coherence. The authors showed that closure phase is related to the heterogeneity of intensity and phase changes and is independent of the magnitude of changes. In this letter, we study the influence of soil moisture changes on closure phase and coherence of multi-looked pixels. We aim to answer the question whether closure phase or InSAR coherence can be used to estimate soil moisture changes.

To study the relationship between soil moisture changes and InSAR coherence and closure phase, we generated semi-synthetic interferograms with variable soil moisture changes between the images. Using an analytical soil moisture model (Molan and Lu, 2020), the soil moisture values were converted to their corresponding intensity and phase changes. The intensity and phase changes were applied to the real pixels to generate synthetic pixels. Finally, semi-synthetic interferograms were generated using the real and synthetic pixels. The results from synthetic data showed that multi-looked phase artifact, decorrelation, and closure phase increase by increasing the standard deviation of soil moisture changes within the multi-look window. We show that, compared to soil moisture changes, non-soil moisture changes can lead to larger decorrelation and closure phase values. To confirm the results of synthetic data, we used phase and coherence images generated from real SAR images of L-band ALOS PALSAR over two study areas in Idaho and Oregon. It is also shown that heterogeneity of phase changes, decorrelation, and closure phase are correlated with each other and with land cover type. We conclude that, in general, closure phase and InSAR coherence are independent of the magnitude of soil moisture changes and are inappropriate tools to estimate soil moisture changes.

The rest of this letter is structured as follows: Section 6.2 describes the method to generate semi-synthetic interferograms; Section 6.3 provides the results generated from synthetic and real SAR images; Section 6.4 provides a discussion on the results; conclusions appear in Section 6.5.

6.2 Materials and Methods

To investigate the effect of statistical characteristics of soil moisture changes on InSAR coherence, and closure phase, we exploit semi-synthetic interferograms. The first image of a

semi-synthetic interferogram $\boldsymbol{u}_1$ is a real single-looked SAR image containing *p.q=n* pixels. The second image $\boldsymbol{u}_2$ is synthetic data generated from the real data by applying a change vector $\Delta\boldsymbol{u}_{1,2}$

$$\boldsymbol{u}_{\mathbf{j}} = \left[u_j^{(1)}, u_j^{(2)}, \dots, u_j^{(n)}\right]', \mathrm{j} = 1,2 \tag{6.1}$$

The intensity and phase changes of the change vector, respectively, are

$$\Delta\boldsymbol{dB} = f_{dB}(M_v) + \Delta\boldsymbol{dB_i},\ \Delta\boldsymbol{\theta} = f_{\theta}(M_v) + \Delta\boldsymbol{\theta_i} \tag{6.2}$$

where $\boldsymbol{M}_v$ is the vector of soil moisture changes between the real and synthetic images

$$M_v = \left[m^{(1)}, m^{(2)}, \dots, m^{(n)}\right]'. \tag{6.3}$$

In the equations above $f_{dB}(\boldsymbol{M}_v)$, and $f_{\theta}(\boldsymbol{M}_v)$ are soil moisture dependent intensity and phase changes, respectively. $\Delta\boldsymbol{dB}_{ns}$ and $\Delta\boldsymbol{\theta}_{ns}$ indicate the intensity and phase changes associated with non-soil moisture changes between the two images, which in general include mechanical deformations, other artifacts, and noise.

In the literature, studies suggest a linear relationship between soil moisture changes and SAR intensity changes (*e.g.* Barrett et al., 2009). Also, a linear relationship between soil moisture changes and phase changes has been reported in the studies where statistical approaches have been conducted (*e.g.* Zwieback et al., 2015). Thus far, few analytical and statistical approaches have been introduced to quantify the relationship between soil moisture and SAR intensity or phase (Zwieback et al., 2016, 2017; Nolan et al., 2013; Zhang et al., 2008; Barrett et al., 2012; Hajnesk and Prats, 2008; Nesti et al., 1998, 2015; Rudant et al., 1996; Morrison et al., 2011). The studies generally model either phase or intensity. In this letter, we use the analytical model developed by Molan and Lu (2020). The model uses Mie equations and successfully quantifies soil moisture induced SAR intensity and phase changes. It models soil as a collection of discrete coarse scatterers embedded in a background that is an attenuating dielectric medium comprised of finer soil grains. The signal of a focused single-looked pixel, in the model, is (Molan and Lu, 2020)

$$u = \sum_{i=1}^{N} e^{-j2kR} t_{1,2}\, t_{2,1}\, s_i\, e^{-2\int_0^z \frac{\alpha}{\cos(\theta_r)} dz'} e^{-j2(k_0 y_i \sin(\theta_r))}\, e^{-2j\int_0^z \beta \cos(\theta_r) dz'} W_a(x_i) W_r(y_i \sin(\theta_r) - n\cos(\theta_r) z_i) \quad (6.4)$$

where u is the phasor of the single looked pixel, *i.e.* the total backscattering from all scattering points within the pixel, n is the refraction index of the soil medium, θ_r is the refracted angle, $t_{i,j}$ is the one-way transmission coefficient of amplitude from medium i to medium j (Barrett et al., 2009), R is the range of the pixel, α and β are absorption and phase constants of the medium, k_0

is free air wavenumber, and s_i is the amplitude of the scattered wave by the scatterer. Also, W_a and W_r are slant range and azimuth resolution functions for the single scatterer located at (x_i, y_i, z_i). Figure 6.1 shows modeled intensity and phase changes calculated using equation 6.4. Without loss of generality, we assume that the soil background is loam that contains silt, clay, and sand. It also contains gravels with the grain size (r_p) of 2.65 cm and volume fraction (f_s) of 1.0 percent.

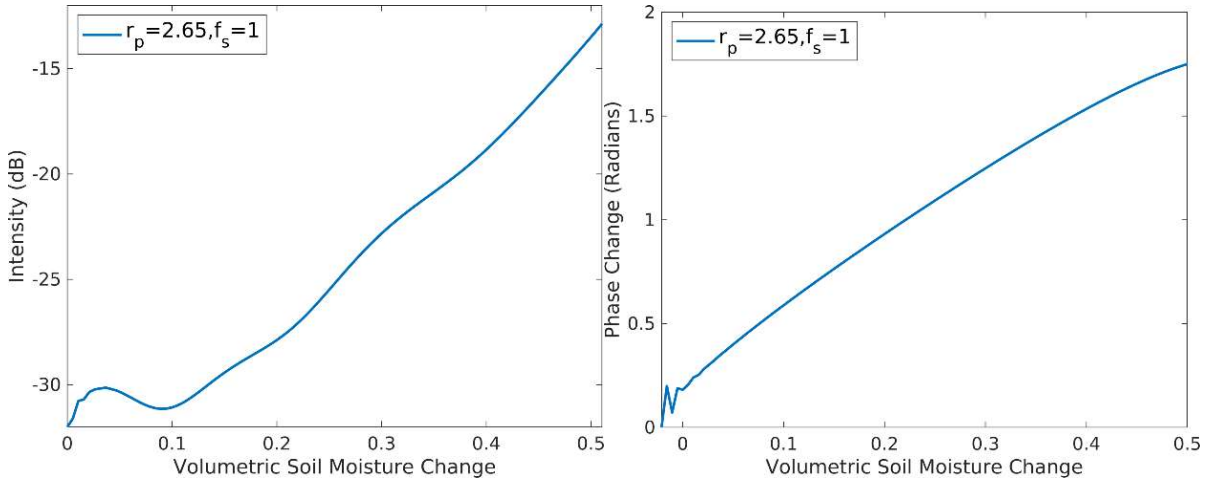

Figure 6.1. Intensity and phase changes of the soil. r_p is the radius of the larger grains (main scatterers) and f_s is the fractional volume of larger grains.

Using equations 6.2 and 6.4, we can generate a synthetic image from a real image and a synthetic image with pre-defined soil moisture changes. The real image has *n* single looked pixels. The soil moisture differences between the real and the synthetic image $\boldsymbol{M_v}$ is a random vector with pre-defined average Δm_v and standard deviation σ_{mv} values. Therefore, one soil moisture change Mv_i is associated to each of the single-looked pixels in the first image $u_1^{(i)}$. The soil moisture changes are converted to the equivalent intensity and phase changes using equation

6.4. Then, the intensity and phase changes are applied to $u_1^{(i)}$ to generate $u_2^{(i)}$. After creating the synthetic image, an interferogram can be generated using the real and synthetic images. Therefore, by applying different values to the average and standard deviation of soil moisture changes and calculating the resulting phase and coherence changes, we can assess the influence of the statistical properties of soil moisture changes on InSAR phase and coherence. To compare the influence of soil moisture change with the effect of non-soil moisture changes, we first assume that the non-soil moisture changes are negligible. Then, we generate the second type of interferograms that have both soil moisture and non-soil moisture changes.

6.3 Results

6.3.1 Synthetic data

The interferometric phase and coeherence are the angle and magnitude of

$$\gamma = \frac{E[\boldsymbol{u_1 u_2^*}]}{\sqrt{E[|\boldsymbol{u_1}|^2]E[|\boldsymbol{u_2}|^2]}} \tag{6.5}$$

To assess the influence of the statistical properties of soil moisture changes on InSAR phase and coherence, two types of interferograms are generated. For the first type of the interferograms, non-soil moisture changes are assumed to be zero. This means that $\Delta\boldsymbol{dB}_{ns}$ and $\Delta\boldsymbol{\theta}_{ns}$ in equation 6.2 are zero and we have

$$\Delta \boldsymbol{dB} = f_{dB}(M_v), \Delta \boldsymbol{\theta} = f_{\theta}(M_v) \tag{6.6}$$

The intensity and phase changes associated with soil moisture changes, *i.e.* $f_{dB}(\boldsymbol{M}_v)$ and $f_{\theta}(\boldsymbol{M}_v)$, are calculated using equation 6.4. Then, $\boldsymbol{u}_2$ is calculated by applying the intensity and phase change to $\boldsymbol{u}_1$ and finally, an interferogram is generated using $\boldsymbol{u}_1$ and $\boldsymbol{u}_2$. The average soil moisture changes of 0.05, 0.15, and 0.25 with the standard deviation in the range of 0.01-0.13 were applied between the two images to generate interferograms. For each case with the same average and standard deviation, one thousand interferograms were generated. Figure 6.2 illustrates the phase and coherence of the generated interferograms. In figure 6.2, each point on the solid phase lines is the average phase of one thousand interferograms with a specific Δm_v and σ_{mv}. The same-color dashed lines show the average ± standard deviation of multi-looked phases of the interferograms. The average interferometric coherence values for those interferograms are also shown in figure 6.2.

As stated previously, we considered zero non-soil moisture changes between the images to assess the influence of soil moisture changes of InSAR coherence and closure phase. Now, we generate the second type of semi-synthetic interferograms by applying non-soil moisture changes ($\Delta \boldsymbol{dB}_{ns}$ and $\Delta \boldsymbol{\theta}_{ns}$) in addition to the soil moisture changes. Soil moisture changes lead to intensity and phase changes of SAR images. In general, the intensity and phase values increase by increasing soil moisture (see figure 6.1). In other words, dielectric constant changes due to soil moisture changes cause correlated intensity and phase changes. Unlike soil moisture changes, the intensity and phase changes of non-soil moisture changes are assumed to be uncorrelated.

In the second type of the interferograms, which include both soil moisture and non-soil moisture changes, the average intensity and phase of non-soil moisture changes are considered to be zero. The standard deviations of the intensity and phase changes are 4 dB and 0.75 radians, respectively. The soil moisture changes of the second type of interferograms are identical to the soil moisture changes of the first type. The multi-looked phase and coherence values are shown in figure 6.3. Similar to the first type of interferograms, we generated one thousand interferograms with the same average and standard deviation of changes for each case. Note that the influence of non-soil moisture changes is demonstrated by larger distance between the average plot (solid phase line) and the average ± standard deviation plot (dashed phase lines). The coherence plot of non-soil moisture cases is shown in figure 6.3, which dropped from 1.0 to 0.68 at $\sigma_{mv} = 0$.

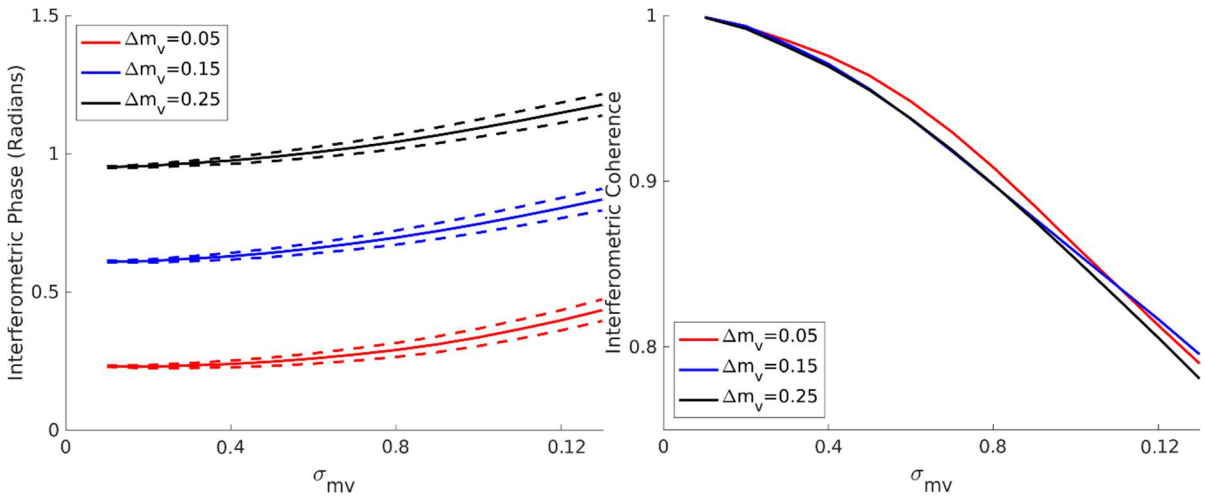

Figure 6.2. The phase and coherence changes due to the change in the standard deviation of soil-moisture changes.

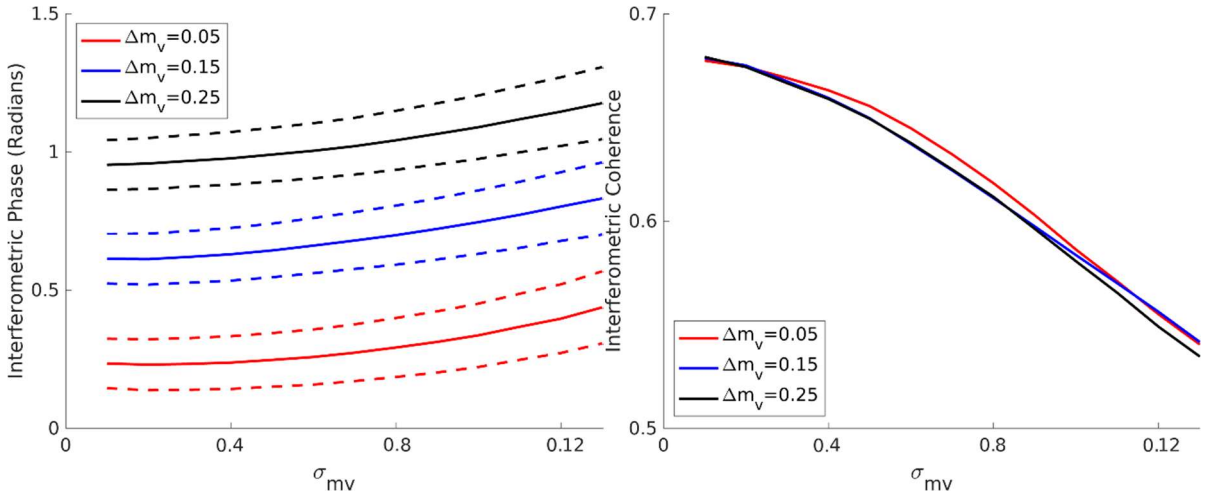

Figure 6.3. The phase and coherence changes due to the change in the average and standard deviation of soil-moisture changes and zero-mean random non-soil moisture change.

Three images can generate three mutual interferograms and one phase triplet, which is calculated by subtracting the phase of the interferogram pairing the first and the last images from the summation of the phases of the two intermediate interferograms (De Zan et al., 2015; Molan et al., 2020)

$$\ddot{\emptyset}_{i,j,k} = \emptyset_{i,j} + \emptyset_{j,k} - \emptyset_{i,k} \tag{6.7}$$

We have used a pair of one real image and one synthetic image to generate the interferograms. Now, we can use one real image and two synthetic images to generate a closure phase image. We used the same strategy applied in the previous section to generate the semi-synthetic interferograms. Figure 6.4 shows the closure phases generated using six different

combinations of soil moisture changes. In figure 6.4, each point on the image is the average value of one thousand closure phases with specific $\Delta m_{v,1}$, $\Delta m_{v,2}$, $\sigma_{mv,1}$, and $\sigma_{mv,1}$ values.

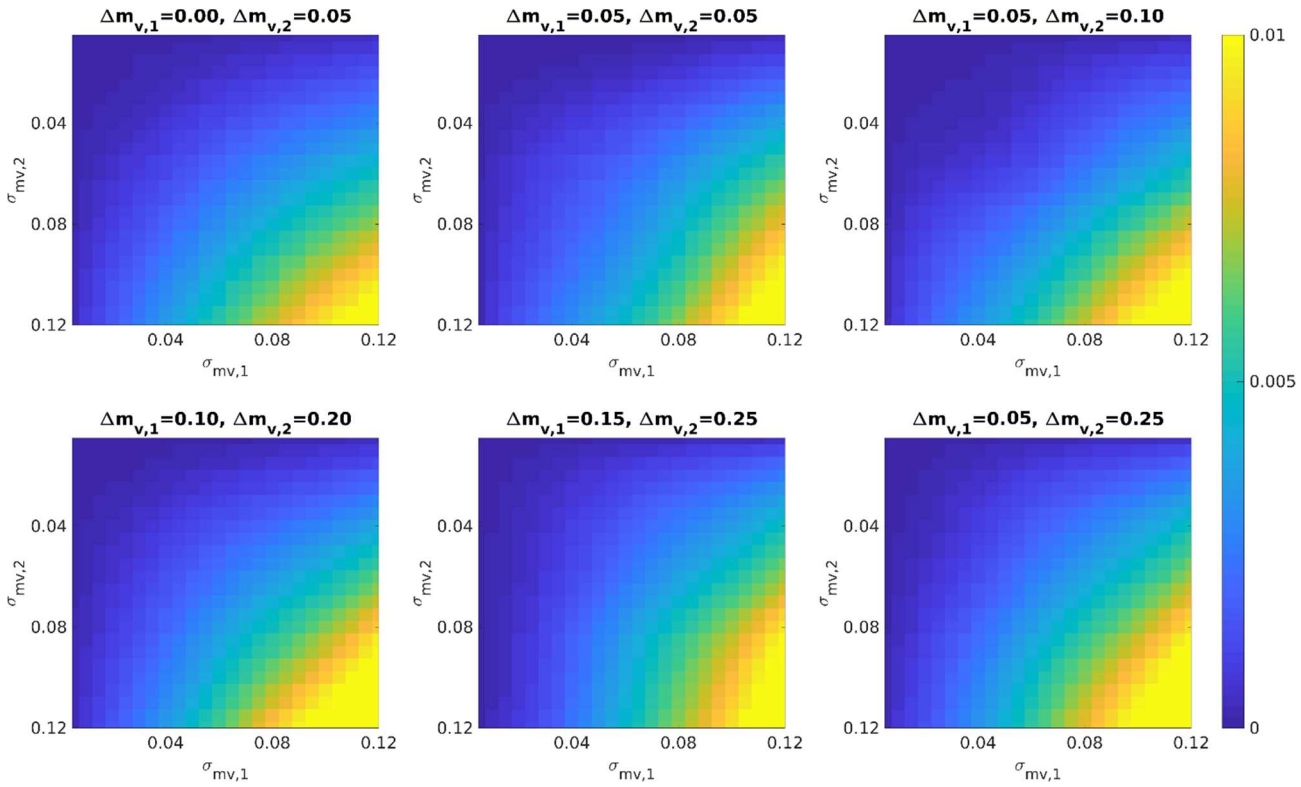

Figure 6.4. Closure phase due to different combination of soil moisture changes.

The results in figure 6.4 were generated by assuming negligible non-soil moisture changes. The second type of closure phases were generated by applying both soil moisture and non-soil moisture changes between the images. We assumed that the non-soil moisture changes induce zero-mean intensity and phase changes with the standard deviations of 4 dB and 1.0 radian, respectively. The results of the second type of closure phases are shown in figure 6.5.

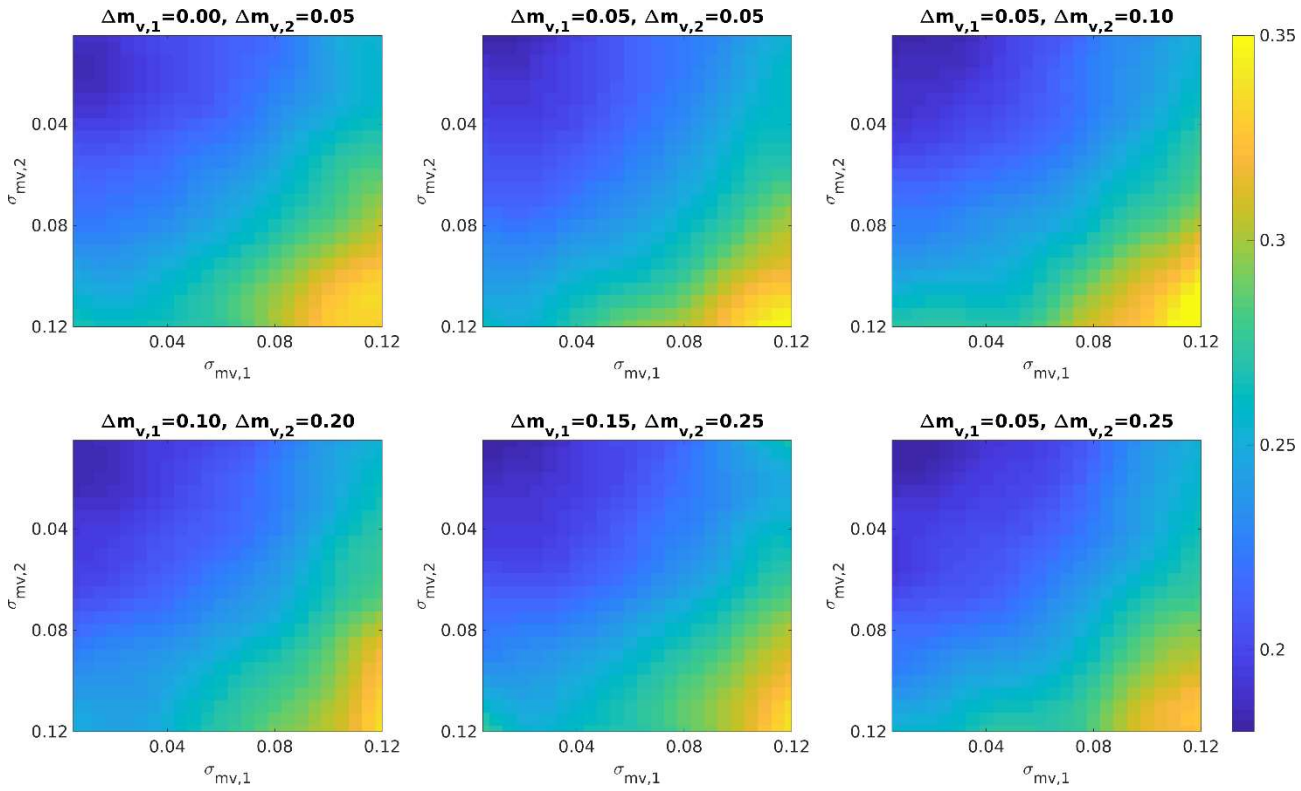

Figure 6.5. Closure phase (in radians) due to different combination of soil moisture changes and zero-mean random non-soil moisture change.

6.3.2 Real data

Our results from synthetic data showed that InSAR coherence and closure phase are functions of the standard deviation of soil moisture changes between images. Now, we use real SAR data over two areas in Oregon and Idaho to evaluate the results generated from the synthetic data. To this end, over each area, three co-registered SLC images (the three first images in table 6.1 and table 6.2) of L-band ALOS PALSAR have been used to generate multi-looked interferograms with 9 and 4 looks in azimuth and range, respectively. To simulate and remove the topographic phase from the interferograms, the Shuttle Radar Topography Mission (SRTM) Digital Elevation Model (DEM) with 1 arc-second spatial resolution was used. The images over

the area in Idaho are from ascending orbital path 208 and frame 860 and the images over the area in Oregon are from ascending orbital path 215 and frame 830. The data are in the fine beam and horizontal-horizontal (HH) polarization mode. Over each study area, from the three co-registered SLC images, three multi-looked interferograms, and three coherence images were generated. In addition, for each study area, three circular standard deviation images S_c (Zar 2010), one for each interferogram, have been generated. The circular standard deviation of a multi-looked pixel is calculated by

$$S_c = \sqrt{-2\ln\left|\sum_{i=1}^{n}\exp(j\theta_i)\right|} \tag{6.8}$$

where *i* is the number of the single-looked pixel, *n* is the total number of single-looked pixels in the multi-looked window, and θ_i is phase change of the pixel **i**. For each area, the three multi-looked interferograms were used to produce a closure phase image. Figures 6.6(a) and 6.7(a) show closure phase images. Similarly, the three circular standard deviation images were used to generate a standard deviation root mean square (RMS) image, *i.e.*

$$RMS_s = \sqrt{\frac{1}{3}\left({S_{c,1}}^2 + {S_{c,2}}^2 + {S_{c,3}}^2\right)} \tag{6.9}$$

Figures 6.6(b) and 6.7(b) show standard deviation RMS images. The three coherence images were also used to generate the average coherence image *R*. Figures 6.6(c) and 6.7(c) show the average decorrelation images, *i.e.* 1-*R*.

No.	**date**	**No.**	**date**	**No.**	**date**	**No.**	**date**
1	2007-07-05	4	2009-07-10	7	2010-05-28	10	2010-10-13
2	2007-08-20	5	2009-10-10	8	2010-07-13	11	2011-02-28
3	2007-11-20	6	2010-04-12	9	2010-08-28		

Table 6.1. The date (yyyy-mm-dd) of the SLC images over the study area in Idaho.

No.	**date**	**No.**	**date**	**No.**	**date**
1	2007-08-01	2	2007-12-17	3	2008-03-18

Table 6.2. The date (yyyy-mm-dd) of the SLC images over the study area in Oregon.

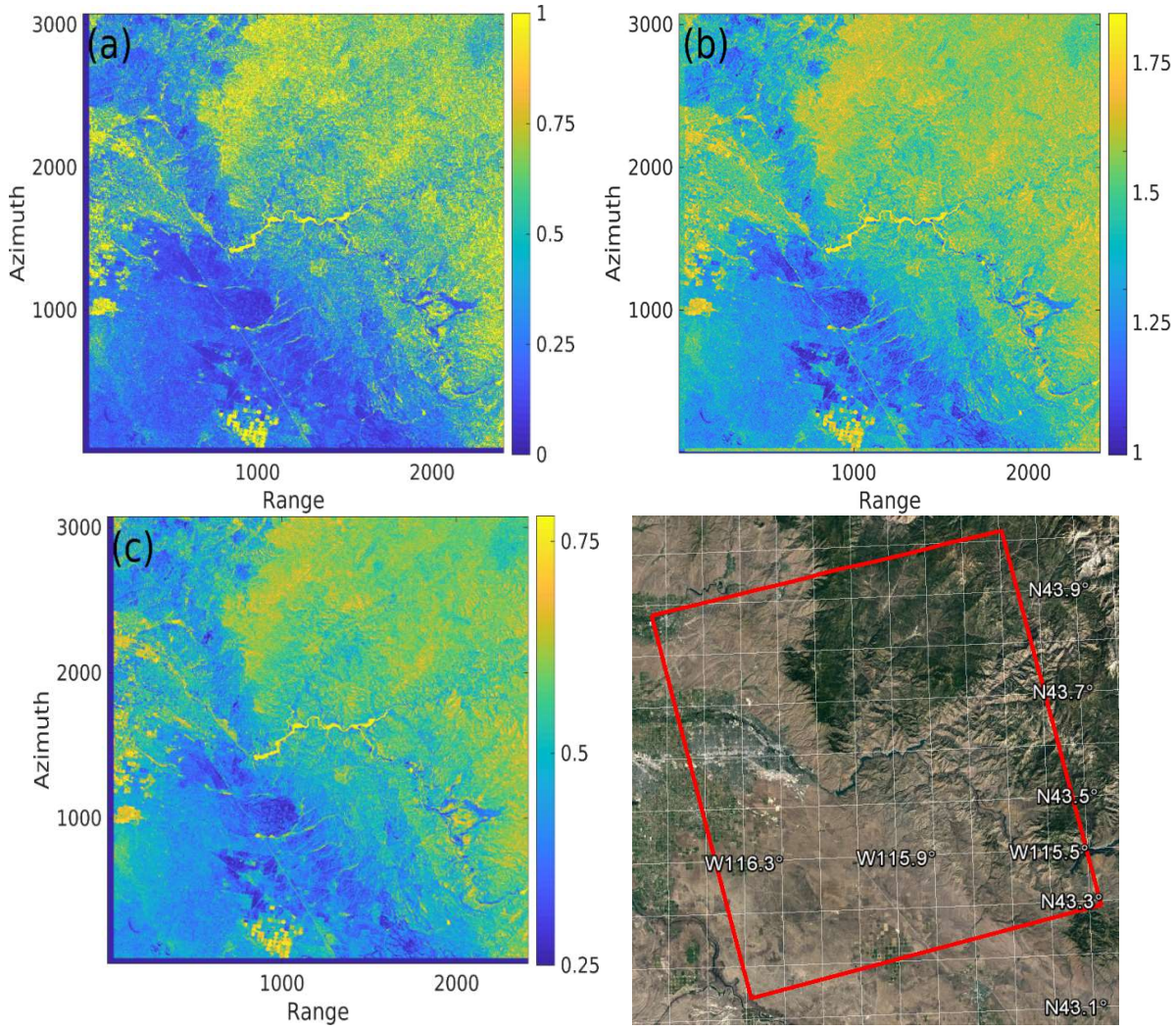

Figure 6.6. Closure phase (a), RMS_s of phase changes (b), and average decorrelation (c) over the study area in Idaho. The study area is in red box on the optical image.

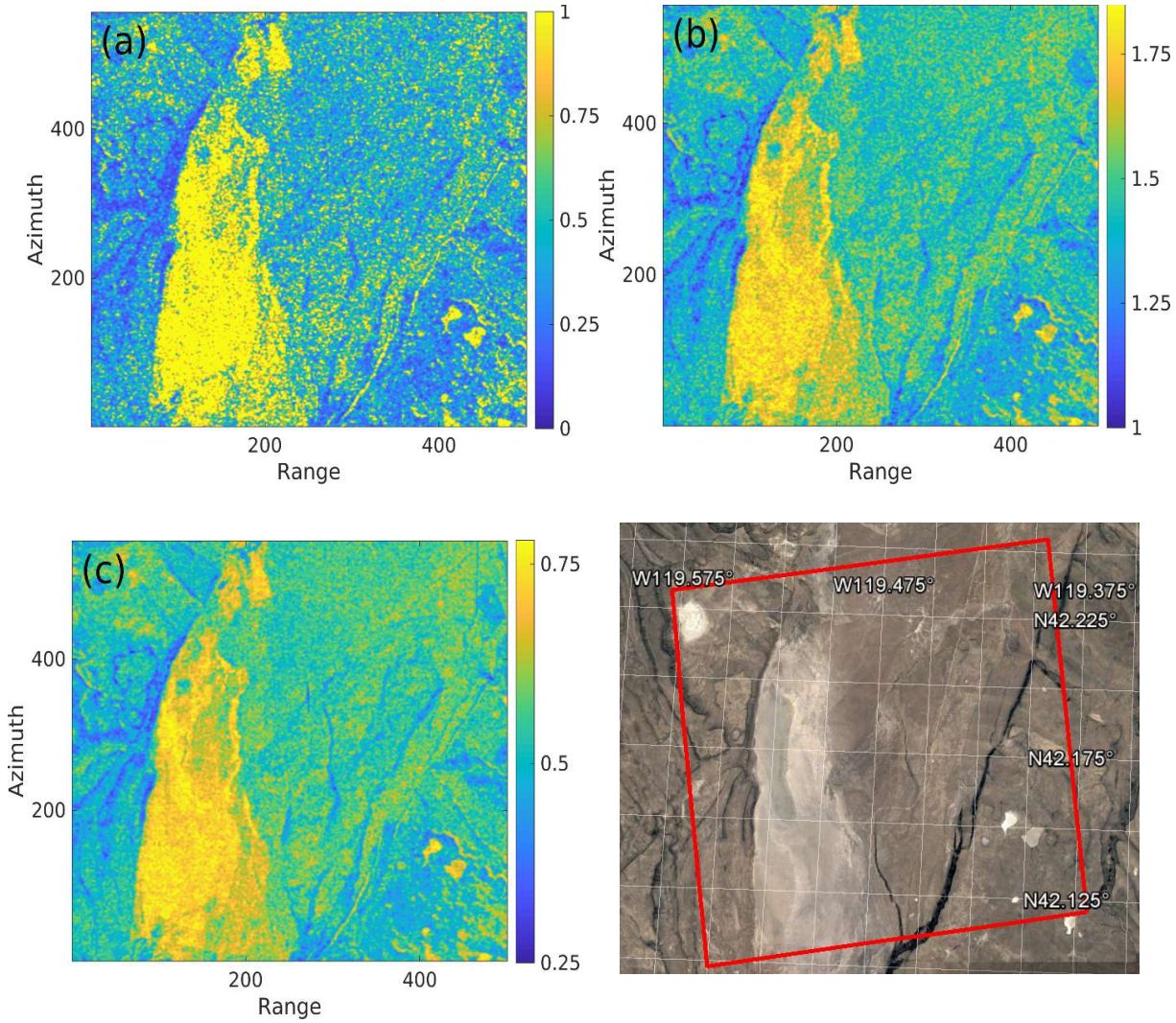

Figure 6.7. Closure phase (a), RMS_s of phase changes (b), and average decorrelation (c) over the study area in Oregon. The study area is in red box on the optical image.

6.4 Discussion

Due to strong effects of decorrelations and noises, single-looked interferograms are noisy. Multi-looking, which averages adjacent pixels in complex interferograms, improves phase reliability by reducing noise. (Ferretti et al., 2011; Goldstein et al., 1998)). It was shown, however, that the statistical properties of intensity and phase changes within a multi-look window influence interferometric phase and coherence (Molan et al., 2020). Molan et al. (2020)

showed that InSAR coherence and closure phase are associated with the heterogeneity of intensity and phase changes. In this letter, we assessed changes in InSAR phase, coherence, and closure phase due to change in the statistical properties of soil moisture changes using semi-synthetic interferograms. Our results indicate that non-zero standard deviation of soil moisture changes within a multi-look window leads to decorrelation and non-zero closure phase. Regarding this, we discuss here whether InSAR phase, coherence, and closure phase can be used for soil moisture estimation.

6.4.1 Soil moisture-induced multi-looked phase artifact and non-zero phase triplet

Multi-looked InSAR phase has been used for soil moisture estimation. Multi-looked interferometric phase has contributions from physical changes as well as the statistical properties of the intensity and phase of single-looked pixels (Molan et al., 2020). In the case of soil moisture changes between two multi-looked pixels, the average and standard deviation of soil moisture changes contribute to physical and statistical phases, respectively.

The results in figure 6.2 illustrate the average interferometric phase $\emptyset$, physical phase $\emptyset_p$, statistical phase ($\emptyset_s = \emptyset - \emptyset_p$), and phase diversity. The solid and dashed lines, respectively, show the average and standard deviation of the interferometric phases. The physical phase $\emptyset_p$ in figure 6.2 is the interferometric phase at $\sigma_{mv} = 0$ (the first point on the solid line), at which the statistical phase ($\emptyset_s$) is zero. The average statistical phase $\emptyset_s$ is the phase difference between interferometric phase $\emptyset$ (the solid line) and the physical phase $\emptyset_p$ (the first point on the solid line).

In figure 6.2, we show that the average statistical phase increases by increasing the standard deviation of soil moisture changes. However, soil moisture-induced phase diversity, *i.e.*

standard deviation, is negligible. Similar behavior of the average interferometric phase and statistical phase can be seen in figure 6.3, which illustrates the results of non-soil moisture cases. Also, the diversity of interferometric phases increases by increasing the standard deviation of soil moisture and non-soil moisture changes. However, non-soil moisture changes lead to larger diversity of phase changes compared to soil moisture changes (compare the dashed lines in figures 6.2 and 6.3).

Considering the contribution of statistical phase, InSAR phase can be potentially used for soil moisture estimation if the magnitude of physical phase is meaningfully larger than the statistical phase. A thorough discussion of physical and statistical phase contributions on multi-looked phase has been provided in Molan et al. (2020). However, as a general practical strategy, pixels with low coherence values should be avoided because low coherence pixels are associated with larger statistical phases. In other word, both decorrelation and multi-looked phase artifact (statistical phase) are functions of the standard deviation of changes (Molan et al., 2020).

The results in figure 6.4 show that closure phase is zero only when σ_{mv} between images is zero. It is shown in figure 6.4 that regardless of the magnitude of soil moisture changes, closure phase increases by increasing σ_{mv}. This indicates that closure phase is independent of the magnitude of changes and is an inappropriate means to estimate soil moisture changes. Also, a comparison between soil moisture and non-soil moisture results, illustrated, in figures 6.4 and 6.5 respectively, shows that the closure phase values increase drastically by applying non-soil moisture changes. This is because non-soil moisture changes induce much larger phase diversity (see figures 6.2 and 6.3). The practical implication of this is that closure phase due to non-soil moisture changes can mask soil moisture-induced closure phase. The general conclusion that one can make is that closure phase, decorrelation, and phase diversity are smaller when the intensity

and phase changes are correlated, *i.e.* soil moisture-induced changes. The quantities increase drastically by increasing non-soil moisture changes, *i.e.* non-correlated intensity and phase changes.

6.4.2 Soil moisture-induced decorrelation

The results illustrated in figure 6.2 show that coherence decreases by increasing the standard deviation of soil moisture changes. It should be noted that the small changes in coherence and closure phase values of different soil moisture changes are due to non-linear relationships between soil moisture and the intensity and phase of single-looked pixels (see figure 6.1). Regarding the relationship between soil moisture changes and InSAR coherence, the main question is whether we can exploit InSAR coherence to estimate soil moisture changes. The results indicate that coherence, like closure phase, is a function of the standard deviation of changes and is independent of the magnitude of changes. Therefore, it cannot be directly used to estimate soil moisture. This conclusion is true except for those cases where the magnitude and diversity of soil moisture changes (dielectric constant changes in general) are correlated. It should be noted that the uncertainty of soil moisture estimation for the cases where the magnitude and diversity are correlated is related to the degree of association between the magnitude and diversity.

In our study area in Idaho, we show an example to assess the correlation between the magnitude and diversity of changes. To do this, for each multi-looked pixel, we calculated the correlation coefficient between the magnitude and diversity of the phase of single-looked pixels within the multi-looked window. Over the study area in Idaho, eleven co-registered SLC images of L-band ALOS PALSAR (table 6.1) were used to generate 41 unwrapped multi-looked interferograms with 14 and 7 looks in azimuth and range. The processing approach to generate

unwrapped interferograms was explained earlier in section 3. For each interferogram, one standard deviation of phase changes within multi-looked pixels were calculated. Therefore, each multi-looked pixel has forty-one interferometric phase values and forty-one standard deviation values. Finally, for each multi-looked pixel, the correlation coefficient between the interferometric phase values and the standard deviation values was calculated. Figure 6.8 illustrates the calculated correlation coefficient image. It shows that the correlation between the diversity and magnitude of phase changes is not strong, *i.e.* $|r| < 0.5$.

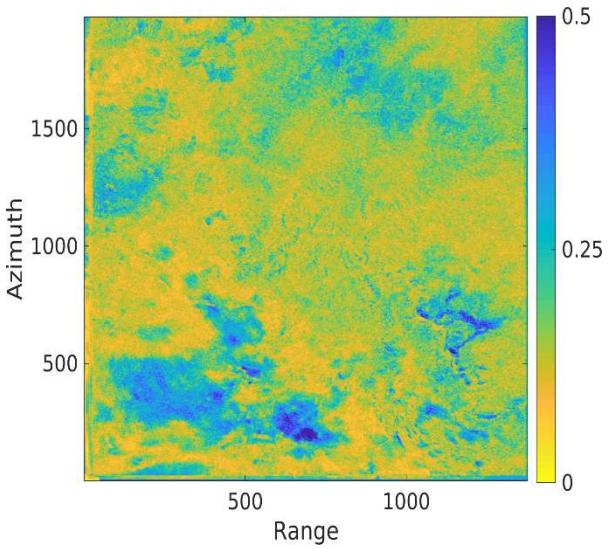

Figure 6.8. The correlation coefficient images over the study areas in Idaho.

It should be noted that even with correlated magnitude and diversity of changes, soil moisture estimation using closure phase, if not impractical, will suffer from high uncertainty in the results. This is because, unlike coherence that is associated with the statistical properties of changes between one pair of images, closure phase has contribution from three interferograms, each with different statistical properties.

One other problem in using coherence to estimate soil moisture is related to the ambiguity in the orientation of soil moisture changes. An inferred soil moisture change can be assigned to both drying and wetting soils. This is even more complicated for closure phase because it combines three interferograms. Furthermore, it should be noted that soil moisture estimation using InSAR coherence and closure phase is even more challenging in practice. Coherence reduction and non-zero phase triplet due to non-soil moisture changes can bury the decorrelation and non-zero phase triplet of soil moisture changes. Figures 6.6 and 6.7 show optical images of our study areas. When comparing closure phase values over different land cover types, we see very small values over bare soil with drastic increases over vegetated areas and agricultural fields (figure 6.6). The standard deviation RMS and average decorrelation also show similar behaviors over different land cover types. The practical implication of this is that possible soil moisture signal in coherence and closure phase will be buried by the larger influence of vegetation.

Yet, the effect of vegetation is not the only obscuring influence on soil moisture-induced decorrelation and closure phase. In figure 6.7, which shows the results over the study area in Oregon, decorrelation and closure phase are larger over unconsolidated sediments, *i.e.* the brighter area on the left side of the optical image. The area is covered by unconsolidated Quaternary surficial deposits (Walker et al., 1965). Although not vegetated, higher decorrelation, closure phase, and diversity values can be seen over the area. This is because surficial deposits can be easily moved by surface water that leads to increased phase diversity.

6.5 Conclusion

Our analysis showed that InSAR coherence and closure phase are functions of the diversity of soil moisture and non-soil moisture changes. The results of the synthetic data

illustrated that non-soil moisture changes have a larger influence on decorrelation and closure phase. The results of the real data confirm that compared to soil moisture changes, vegetation and surficial processes lead to much larger closure phase and decorrelations. It is also shown that closure phase and decorrelation are correlated with each other and with land cover type.

By considering the results of the synthetic and real data, we conclude that coherence and closure phase are not appropriate tools for soil moisture estimation. However, over sparsely vegetated areas and bare soils with stable surface deposits, coherence can be associated with soil moisture changes if a strong correlation exists between the magnitude and diversity of soil moisture changes and if coherence reduction caused by other environmental factors are negligible.

Acknowledgment: The work is funded by the NASA Earth Surface & Interior Program: NASA Science Team (80NSSC19K1491, NNX16AK56G) and the Shuler-Foscue Endowment at Southern Methodist University.

References

Massonnet, D., and K. Feigl. 1998. Radar interferometry and its application to changes in the Earth's surface, *Rev. Geophys.,* 36, 441-500.

Bürgmann, R., P.A. Rosen, and E.J. Fielding. 2000. Synthetic aperture radar interferometry to measure Earth's surface topography and its deformation. Annu. Rev. *Earth Planet. Sci.,* 28, 169–209.

Simons, M., and P. Rosen. 2007. Interferometric Synthetic Aperture Radar Geodesy. *Treatise Geophys. Geodesy*, 3, 391–446.

Lu, Z., and D. Dzurisin. 2014. InSAR Imaging of Aleutian Volcanoes: Monitoring a Volcanic arc from Space, Geophysical Sciences, Springer Praxis Books, Springer: Chichester, UK, 2014, p. 390.

Ferretti, A., C. Prati, and F. Rocca. 2001. Permanent scatterers in SAR interferometry. *IEEE Transactions on Geoscience and Remote Sensing*, 39, 8–20.

Molan, Y.E., J.-W. Kim, Z. Lu, B. Wylie, and Z. Zhu. 2018a. Modeling Wildfire-Induced Permafrost Deformation in an Alaskan Boreal Forest Using InSAR Observations. *Remote Sens*., 10, 405.

Rykhus, R., and Z. Lu. 2008. InSAR detects possible thaw settlement in the Alaskan Arctic Coastal Plain. *Can. J. Remote Sens*., 34, 100–112.

Liu, L., T. Zhang, and J. Wahr. 2010. InSAR measurements of surface deformation over permafrost on the North Slope of Alaska. *J. Geophys. Res*., 115, F03023, doi:10.1029/2009JF001547.

Molan, Y.E., and Z. Lu. 2020a. Modeling InSAR Phase and SAR intensity Changes Induced by Soil Moisture, *IEEE TGRS*, DOI: 10.1109/TGRS.2020.2970841.

Hirschi, M., P. Viterbo, and S. Seneviratne. 2006. Basin-scale water balance estimates of terrestrial water storage variations from ECMWF operational forecast analysis. *Geophys. Res. Lett.*, 33, L21401.

Liang, W.L., F. X. Hung, M. C. Chan, and T. H. Lu. 2014. Spatial structure of surface soil water content in a natural forested headwater catchment with a subtropical monsoon climate. *J. Hydrol*., 516, 210–221.

Seneviratne, S.I., P. Viterbo, D. Luthi, and C. Schar. 2004. Inferring changes in terrestrial water storage using ERA-40 reanalysis data: The Mississippi River basin. *J. Clim*., 17, 2039–2057.

Cardinali, M., F. Ardizzone, M. Galli, F. Guzzetti, and P. Reichenbach. 2000. Landslides triggered by rapid snow melting, the December 1996-January 1997 event in Central Italy," *in proceedings of the EGS Plinius Conference,* Cosenza, Italy, 439-448.

Robinson, D.A., and C. S. Campbell. 2008. Soil Moisture Measurement for Ecological and Hydrological Watershed-Scale Observatories: A Review. *Vadose Zone J.*, 7, 358–389.

De Zan, F., A. Parizzi, P. Prats-Iraola, and P. Lopez-Dekker. 2014. A SAR interferometric model for soil moisture. *IEEE Transactions on Geoscience and Remote Sensing*, 52, 418–425.

De Zan, F., M. Zonno, and P. López-Dekker. 2015. Phase inconsistencies and multiple scattering in SAR interferometry. *IEEE Trans. Geosci. Remote Sens.*, 53, 6608–6616.

Zwieback, S., S. Hensley, and I. Hajnsek. 2015. Assessment of soil moisture effects on L-band radar interferometry. *Remote Sens. Environ*. 2015, 164, 77–89, doi:10.1016/j.rse.04.012.

Zwieback, S., X. Liu, S. Antonova, B. Heim, A. Bartsch, J. Boike, and I. Hajnsek. 2016. A statistical test of phase closure to detect influences on DInSAR deformation estimates besides displacements and decorrelation noise: Two case studies in high-latitude regions. *IEEE Trans. Geosci. Remote Sens.*, vol. 54, no. 9, pp. 5588-5601.

Molan, Y.E., J.-W. Kim, Z. Lu, P. Agram. 2018b. L-Band Temporal Coherence Assessment and Modeling Using Amplitude and Snow Depth over Interior Alaska. *Remote Sens.* 10, 150.

Hoekstra, P. and A. Delaney. 1974. Dielectric properties of soils at UHF and microwave frequencies. *J. Geophys. Res.*, 79:1699-1708.

Hallikainen, M.T., F.T. Ulaby, M.C. Dobson, M.A. El-Rayes, and L.-K. Wu. 1985. Microwave dielectric behavior of wet soil—Part 1: Empirical models and experimental observations," *IEEE Trans. Geosci. Remote Sens.,* vol. GE-23, no. 1, pp. 25–34.

Hensley, S., T. Michel, J. Van Zyl, R. Muellerschoen, B. Chapman, S. Oveisgharan, Z. S. Haddad, T. Jackson, and I. Mladenova. 2011. Effect of soil moisture on polarimetric-interferometric repeat pass observations by UAVSAR during 2010 Canadian Soil Moisture campaign. In Proc. *IEEE IGARSS*, pp. 1063–1066.

Zwieback, S., Hensley, S., Hajnsek, I., 2017. Soil moisture estimation using differential radar interferometry: toward separating soil moisture and displacements. IEEE Trans.Geosci. Remote Sens. 55 (9), 5069–5083.https://doi.org/10.1109/TGRS.2017.2702099

Molan, Y.E., Z. Lu, and J-W. Kim. 2020. Influence of the statistical properties of phase and intensity on closure phase, *IEEE TGRS*.

De Zan, F., and G. Gomba. 2018. Vegetation and soil moisture inversion from SAR closure phases: First experiments and results. *Remote Sensing of Environment,* Volume 217, Pages 562-572

Barrett, B., E. Dwyer, and P. Whelan. 2009. Soil moisture retrieval from active spaceborne microwave observations: An evaluation of current techniques," *Remote Sensing,* 1, 210–242.

Lu, Z., and D. Meyer. 2002. Study of high SAR backscattering due to an increase of soil moisture over less vegetated area: its implication for characteristic of backscattering. *International Journal of Remote Sensing*, 23 (6), 1065-1076.

Nolan, M., D. R. Fatland, and L. Hinzman. 2003. DInsar measurement of soil moisture. *IEEE Trans. Geosci. Remote Sens*., vol. 41, no. 12, pp. 2802–2013.

Zhang, T., Q. Zeng, Y. Li, and Y. Xiang. 2008. Study on relation between InSAR coherence and soil moisture. In Proc. *ISPRS Congr.,* vol. 37, pp. 131–134.

Barrett, B., E. Dwyer, and P. Whelan. 2012. The use of C- and L-band repeatpass interferometric SAR coherence for soil moisture change detectionin vegetated areas. *Open Remote Sens. J.,* vol. 5, no. 1, pp. 37–53.

Hajnsek, I., and P. Prats. 2008. Soil moisture estimation in time with DInSAR. In Proc. *IEEE IGARSS*, vol. III, pp. 546–549.

Nesti, G., D. Tarchi, and J.-P. Rudant. 1995. Decorrelation of backscattered signal due to soil moisture changes. In Proc. *Int. Geosci. Remote Sens.* Symp., vol. 3, pp. 2026–2028.

Nesti, G., D. Tarchi, D. Despan, J.-P. Rudant, A. Bedidi, P. Borderies, and E. Bachelier. 1998. Phase shift and decorrelation of radar signal related to soil moisture changes. In Proc. 2nd ESA Int. Workshop Retrieval Bio- Geo-Phys. Parameter SAR Data Land Appl., pp. 423–430.

Rudant, J.-P., A. Bedidi, R. Calonne, D. Massonnet, G. Nesti, and D. Tarchi. 1996. Laboratory experiment for the interpretation of phase shift in SAR interferograms. In Proceedings of *FRINGE*.

Morrison, K., J. C. Bennett, M. Nolan, and R. Menon. 2011. Laboratory measurement of the DInSAR response to spatiotemporal variations in soil moisture. *IEEE Trans. Geosci. Remote Sens*., vol. 49, no. 10, pp. 3815–3823.

Zar, J.H. 2010. Biostatistical Analysis. 5th ed. Upper Saddle River, N.J.: Prentice-Hall/Pearson.

Ferretti, A., A. Fumagalli, F. Novali, C. Prati, F. Rocca, and A. Rucci. 2011. A new algorithm for processing interferometric data-stacks: SqueeSAR. *IEEE Transactions on Geoscience and Remote Sensing*, 49, 3460–3470. http://dx.doi.org/10.1109/TGRS.2011.2124465.

Goldstein, R.M., H.A. Zebker, and C.L. Werner. 1988. Satellite Radar Interferometric: Two-dimensional phase unwrapping. *Radio Sci.*, Vol.23, No.4, pp.713-720.

Walker, G.W., and C. Repenning. 1965. Reconnaissance geologic map of the Adel quadrangle, Lake, Harney, and Malheur Counties, Oregon: Reston, Va., U.S. Geological Survey Interpretive Map I-446, scale 1:250,000.

CHAPTER 7

FINDINGS AND FUTURE WORK

InSAR detected displacement can be systematically biased by the changes in soil moisture. Ordinary InSAR analyses rarely take into account soil moisture influences on InSAR phase, and coherence. However, soil moisture-induced uncompensated biases in the spatial and temporal patterns of InSAR detected displacement can limit its applicability and impacts its reliability and robustness. This dissertation illustrates analytical and statistical approaches to model the influence of soil moisture of InSAR phase and coherence. The highlights of the major chapters of this dissertation are summarized below.

7.1 Highlights

Chapter 3: Temporal coherence is usually modeled as a univariate exponential function of temporal baseline. The coherence models introduced so far have largely neglected the effect of the temporal change in backscattering on InSAR coherence. We introduced a new temporal decorrelation model that considers changes in surface backscattering by utilizing the relative change in SAR intensity between two images as a proxy for the change in surface scattering parameters. The model also takes into account the decorrelation due to the change in snow depth between two images. The improvements made by the model has been statistically proved to be significant with 99% confidence level.

Chapter 4: An analytical model for soil moisture-induced SAR intensity and InSAR phase changes is provided in this chapter. We quantified the influence of soil moisture on InSAR phase and SAR intensity by employing a volume scattering model. Our volume scattering model successfully estimates SAR intensity and InSAR phase changes due to soil moisture changes. In addition to soil moisture changes, the model also takes into account the scatterers' size and their volumetric fraction. This may open new window in the studying of soil structure using SAR images and InSAR methods.

Chapter 5: We study the influence of statistical properties of intensity and phase changes of single-looked pixels on multi-looked phase and coherence. By quantifying the extent of their influences on phase triplet, we showed that the statistical properties of intensity of pixels within a multi-looking window can induce changes in interferometric phase and coherence and contribute to non-zero closure phase. We demonstrate that the intensity induced changes increase by increasing the standard deviation of phase changes, dispersion index of intensity, and the correlation between intensity and phase changes. Our results show that closure phase is only a function of the statistical properties of the phase and intensity of pixels and does not possess the information about the magnitude of physical changes.

Chapter 6: This work provides a statistical assessment of the influence of soil moisture on InSAR coherence and closure phase and answers the question whether or not InSAR coherence and closure phase can be used for soil moisture estimation. Our results show that the diversity of soil moisture values within the multi-look window gives rise to decorrelations, multi-looked phase artifact, and consequently non-zero phase triplet. It is shown that decorrelation, and closure phase increase by increasing the diversity of soil moisture changes within the multi-look window. We showed that compared to soil moisture changes, non-soil moisture changes can lead

to larger decorrelations and closure phases. We concluded that closure phase and InSAR coherence are independent of the magnitude of soil moisture changes and are inappropriate tools to estimate soil moisture changes.

7.2 Future Work

Extending the L-band soil moisture model to C-, P-, and S-bands: The volumetric soil moisture model developed in Molan and Lu, 2020, is a function of wavelength. Therefore, it can be extended to C-, S, and P-bands. The model for C-band is, however, expected to have higher uncertainty. This is because surface backscattering and surface temporal change have greater influence on smaller wavelengths. This leads to greater contribution of the surface backscattering to the received signal.

Developing analytical models to estimate and remove InSAR phase change due to the changes in vegetation water content: The analytical soil moisture model developed in this dissertation can estimate soil moisture-induced phase changes. It, however, does not estimate the phase changes due to the change in vegetation water content. The structure of the scattering medium can be re-modeled and modified for a vegetation layer. Modeling the structure of scatterers embedded in a vegetation layer is the most challenging task to deal.

Developing statistical models to estimate and remove surface moisture-induced phase changes: The analytical model that can quantify soil moisture-induced phase changes should also be modified to estimate phase changes due to the change in the water content of vegetation layer. In practice, however, both soil and vegetation have contributions to InSAR phase and un-mixing the two phase changes is demanding if no ancillary data are

available. With adequate measurement of the soil moisture and vegetation water content during image acquisitions, a statistical model can be developed to estimate surface moisture-induced phase and also to un-mix soil and vegetation phases.

Estimating surface moisture-induced phase using SAR intensity change: The change in surface moisture, *i.e.* soil moisture and water content of vegetation, changes SAR intensity as well as InSAR phase. Therefore, using intensity change as a proxy for phase change can provide an estimation of the phase change. A time-series can be developed to use SAR backscattering intensity to separate intensity-independent phase changes from intensity-dependent phase change.